

**POLITECNICO DI TORINO
AALTO UNIVERSITY**

Master's Degree in Electrical Engineering



**Politecnico
di Torino**



Master's Degree Thesis

**Design and optimization of a V-type
interior permanent magnets motor for EV
application**

Supervisors:

Prof. Gianmario Pellegrino
Prof. Anouar Belahcen
Ph.D. Floran Martin

Candidate:

Giampiero Nitti

March 2022

Summary

Electric vehicles (EV) gained an increasing popularity over the years, especially in the last decade, with significant growth of the sales by 46% to 69%. There are multiple reasons for that: the regulations on CO₂ emissions pushed the automotive industry to focus more on them than the traditional ICE vehicles since they are the only ones capable of respecting the latest restrictions. Furthermore, they are suitable to reach higher performance, but also to adapt to new technologies. Consequently, all the components of the electric traction line are required to have high efficiency. Among them, a lot of research have been focusing on the electric motor and on how taking full advantage from its features. In particular, looking at the already existing solutions on the market, it seems that the V-type interior permanent magnet motor (IPM) is the most promising and used one thanks to the high efficiency, specific power and constant power speed range, but also to the remarkable torque density it can achieve. For this reason, the aim of this thesis is to design and optimize a V-type IPM motor that enhances the characteristic required by the EV application.

As primary task, the working points of the motor have been obtained through the Worldwide Harmonised Light Vehicle Test Procedure (WLTP). It is a driving cycle, introduced in 2017 and adopted to retrieve the energy consumption of EVs. It is more reliable than the others because it is based on real-driving data. The design part has been carried out through the development of a proper reluctance network of the motor of interest. It represents an equivalent magnet circuit of the electric machine. In other words, the aim is to model the magnetic flux path inside the motor, adopting a simple circuit. The main benefit of this approach is to save computational time, although the accuracy could decrease, depending on how complicate the geometry is.

The next step has been to properly define the parameters that affect the rotor geometry, as various properties depend on it. At first stage, we implemented two reluctance networks, for d and q axes, on Simulink. Afterwards, the networks have been analytically solved, including the non-linearity effect of the iron core and the

cross coupling between the axes. This last step involved adding an extra path on the q axis, representing the bridges reluctances, present on d-axis. Different geometries have been drawn to test the model and validate it through the finite element software FEMM 4.2. The results have been compared and the error on the torque has been calculated.

The model made it possible to retrieve the current-flux maps of the motor, which were used to develop a simple open loop control following the MTPA and MTPV laws. The control gives the possibility to follow properly the working points suggested by the driving cycle. The advantage of the model is to permit a straightforward control, acting directly on the d and q components of the current. Finally, the Particle Swarm Optimization (PSO) has been used to optimise the design in those points.

Acknowledgements

I wish to warmly thank all the people I met at Aalto University, Department of Electrical engineering and Automation where this thesis work has been carried out. In particular, I want to express my gratitude to the Professor Anouar Belahcen for having given me the opportunity to work with his brilliant research group, for the availability shown and for the advises. I would like to thank my supervisor D.Sc. Martin Floran, for the unwavering support throughout the months. He helped me a lot, guiding me in the right direction towards the goal. I have learnt a lot from him. I want also to say thank you to the colleagues, or better the friends, with whom I have worked every day. They have been very supportive and made me feel like a part of the group.

I want to say thank you to my Italian supervisor, Professor Gian Mario Pellegrino, for making the whole experience possible. Without him, I would never discover how beautiful is broaden the horizon.

Finally, thank you to my family, my girlfriend Serena, for having unconditionally supported me in every second, especially in the moments of discouragement. Without their emotional support I would not be able to achieve this goal.

Table of Contents

List of Tables	VIII
List of Figures	IX
Acronyms	XIII
1 Introduction	1
2 Background	3
2.1 The electric traction line	3
2.2 Electric motors in electric vehicles	5
2.2.1 Induction motors	7
2.2.2 Reluctance motors	7
2.2.3 Permanent magnets synchronous motors (PMSM)	9
2.3 Interior permanent magnets motor	12
2.3.1 Structure of an IPM	12
2.3.2 Dynamic model	15
2.3.3 From energy balance to torque expression	20
2.3.4 Control theory of IPM	23
2.3.5 Chosen typology: V-type shape	29
3 Traction design	32
3.1 Trends in the EV market	32
3.2 Driving cycle	33
3.3 Vehicle dynamics	35
3.3.1 Newton's second law	36
3.3.2 WLTP working points	39
4 Geometry description	44
4.1 Overall view	44
4.2 Stator geometry	46

4.3	Rotor geometry	50
4.3.1	Magnets design	52
5	Design method	61
5.1	Choice of the design method	61
5.1.1	Reluctance network principles	63
5.2	Reluctance network proposed for the machine	65
5.2.1	Magnetic materials in the machine	67
5.2.2	Description of the reluctance network	71
5.2.3	Solution of the Reluctance network	76
5.3	Validation of the tool	80
5.3.1	Test 1	80
5.3.2	Test 2	87
5.3.3	Computational time	91
6	Control and optimization	92
6.1	MTPA and MTPV loci	92
6.1.1	MTPA implementation	94
6.1.2	MPPV implementation	95
6.1.3	Flux maps interpolation	96
6.1.4	Base and maximum speed calculation	97
6.2	Optimization function	98
6.2.1	Particle swarm optimization	99
6.2.2	Optimization results	101
7	Conclusions	109
	Bibliography	113

List of Tables

3.1	Main performance data of EVs in the market[22][39].	33
3.2	Acceleration time (0-100km/h) [39].	33
3.3	Vehicle features	39
3.4	Efficiency of the traction line	40
5.1	Dimensions of the motor.	81
5.2	Lengths of the magnets barriers.	81
5.3	Materials chosen for the motor.	82
5.4	Current components in the cases.	84
5.5	Torque computation and relative error.	85
5.6	Dimensions of the motor.	88
5.7	Lengths of the magnets barriers.	88
5.8	Torque computation and relative error.	89
6.1	Design parameters.	101
6.2	Dimensions of the motor.	103
6.3	V_{DC} and losses coefficients	104

List of Figures

1.1	EV's and HEV's market growth [1]	1
2.1	Electric traction line.	4
2.2	Electric motor suitable for EVs and HEVs (adapted from [6]).	6
2.3	Tesla induction motor [10].	8
2.4	SynRM rotor designs [12].	9
2.5	Cross section of a SPM motor [13].	10
2.6	Basic structure of an IPM [19].	12
2.7	Rotor shape trends for IPM [18].	14
2.8	Examples of PM assisted Synchronous reluctance motors [24]	15
2.9	Three winding of the stator	15
2.10	Equivalent circuits of an IPM motor [26].	19
2.11	$P-\omega$ and $T-\omega$ of IPM machine.	23
2.12	Current and voltage limits for the IPM machine [34].	25
2.13	MPTA locus for IPM machine [35].	26
2.14	Infinite drive and finite drive [36].	28
2.15	Example of v-type rotor geometry [37]	30
2.16	d and q axes orientation in V-type geometry. Adapted from [38]	31
3.1	WLTP driving cycle.	35
3.2	WLTP working points for the vehicle considered.	41
3.3	$T_{tractive}$ and $T_{resistive}$ at wheels side.	42
3.4	WLTP working points and $T - \omega$ graph at motor side.	42
3.5	$P - \omega$ graph of the motor.	43
4.1	Main dimensions of the electric machine.	45
4.2	Structure of the stator.	47
4.3	Detail of the stator slot.	48
4.4	Syr-e GUI.	49
4.5	Rotor main dimensions.	50
4.6	Magnet barriers in the rotor.	53

4.7	Particular of the central magnet barrier.	54
4.8	Detail of the upper barrier.	56
4.9	Detail of the lower barrier.	58
4.10	Dimensions of the bridges.	59
4.11	Dimensions along the q-axis.	60
5.1	MEC model a V-type IPM motor from [54].	64
5.2	Mesh of the motor [55].	65
5.3	$B-H$ curve of ferromagnetic material [58].	67
5.4	Demagnetizing curve of the most common PM materials.	70
5.5	d -axis reluctance network of the machine.	71
5.6	Permanent magnet dimensions.	72
5.7	Integration of the reluctance.	73
5.8	q -axis reluctance network of the machine.	75
5.9	Graphical representation of Newton-Raphson method.	77
5.10	Solution path of the MEC.	79
5.11	Design of the <i>Test 1</i> IPM motor.	80
5.12	Design of the <i>Test 1</i> IPM motor.	83
5.13	FEM simulation in no load condition:flux density and magnetic flux path.	83
5.14	Error on the iterative method.	84
5.15	Error on the torque.	85
5.16	Φ_d flux map for <i>test 2</i>	86
5.17	Φ_q flux map for <i>test 1</i>	86
5.18	Torque map for <i>test 1</i>	87
5.19	Design of the <i>Test 2</i> IPM motor.	87
5.20	FEM simulation in no load condition:flux density and magnetic flux path.	89
5.21	Error on the torque	90
5.22	Φ_d flux map for <i>test 2</i>	90
5.23	Φ_q flux map for <i>test 2</i>	91
5.24	Torque map for <i>test 2</i>	91
6.1	Control scheme.	92
6.2	Updating solution process in PSO[64].	100
6.3	Iteration trend in the PSO.	102
6.4	Selected WLTP points	102
6.5	Torque-speed graph of the optimized motor.	105
6.6	Optimized design of the motor.	105
6.7	Φ_d flux map of the optimized motor.	106
6.8	Φ_q flux map of the optimized motor.	106

6.9	Torque map of the optimized motor.	106
6.10	FEMM Flux map in <i>Test 1</i>	107
6.11	FEMM Flux map in <i>Test 2</i>	107
6.12	FEMM Flux map in <i>Test 3</i>	108

Acronyms

IPM

Interior permanent magnets motor

PM

Permanent magnets

EV

Electrical vehicles

CPSR

Constant power speed range

EMF

Electromotive force

SRM

Switched reluctance machine

SynRM

Synchronous reluctance machine

PMSM

Permanent magnet synchronous machine

SPM

Surface permanent magnets machine

MMF

Magneto-motive force

FOC

Field-oriented control

DTC

Direct torque control

DFVC

Direct flux vector control

MTPA

Maximum torque per Ampere

MTPV

Maximum torque per Volt

MPPV

Maximum power per Volt

WLTP

Worldwide Harmonised Light-Duty Vehicles Test Procedure

NEDC

New European driving cycle

FEM

Finite elements method

RN

Reluctance network

MEC

Magnetic circuit model

PSO

Particle swarm optimization

Chapter 1

Introduction

In the last decade, the automotive market has been shifting its attention from the traditional internal combustion engine (ICE) vehicles to the electric (EV) or hybrid (HEV) ones. The worldwide sales of these kind of vehicles have significantly grown year after year: taking into consideration the period that goes from 2012 to 2018, it is possible to notice a substantial growth that hovers around 46 % and 69 %. In particular, the year 2021 is considered by the most of the insiders a turning point of this market because it has been forecast a sale of 6.4 millions units, representing an increment year over year equal to the 98 %.

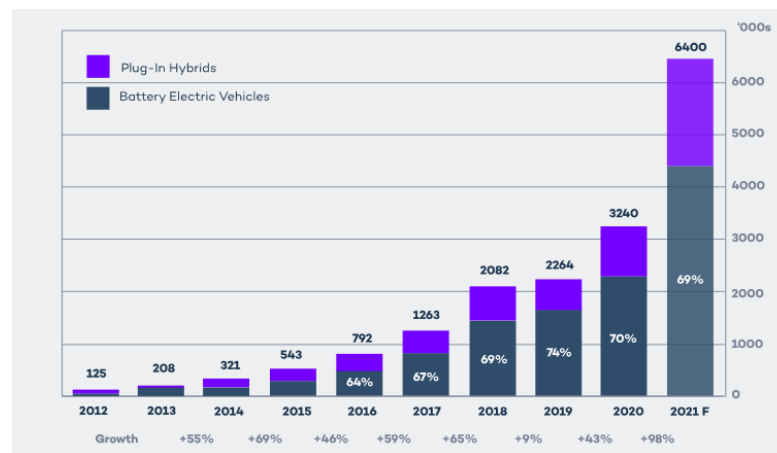


Figure 1.1: EV's and HEV's market growth [1]

Furthermore, the environmental policy of some countries, especially the European ones, has pushed the automotive companies in the direction of hybrid and electric vehicles, being the only capable of satisfy the new strict rules about the pollutants emissions.

Based on these considerations, it is necessary to focus more on how to improve

the design process and the efficiency of the every part of the electric traction line. Among the components, the one that hugely influences the performance of the vehicle is the electric motor. So, it is of interest deepen how the design process can be carried out in order to have a motor that suits the EV application. For these reasons, the aim of this thesis is to design and then optimize a motor for electric vehicles application. In particular, the motor investigated is a V-type interior permanent magnet motor. Nowadays, the permanent magnets motor are the most adopted in the automotive field, because of the high efficiency achievable, the high specific power and power density [2]. Among them, the ones that have the PMs embedded in the rotor are the most promising one, because of possibility to produce torque not only by means of the permanent magnets, but also exploiting the saliency of the machine. In addition they can reach higher values of CPSR and power density [3].

The first part of the thesis has been focused on finding an ideal $T-\omega$ characteristic to be taken as reference. In particular, the WLTP driving cycle has been considered in order to have an idea of the real torque and speed requests during an working condition.

Once obtained the working points, the next step has been to define a proper structure, describing the type of inputs needed for the stator and the rotor and what kind of geometrical relationships link them. In particular, it has been chosen a multi V-type geometry, with three magnet barriers.

As design method, a reluctance network of the machine has been built, for d and q axes. The aim has been to obtain a tool through which computing the electromagnetic torque and analyze the magnetic behaviour along the machine could be fast and easy tasks. Once created, the tool has been validated with the finite element method software FEMM 4.2 and its accuracy has been calculated. In the last part of the work, an open loop control has been implemented in order to have a optimized exploitation of the current and the voltage, following the MTPA and MTPV laws. As last task, once obtained the objective function to be maximized, namely, the power density of the machine, the particle swarm optimization algorithm has been employed, in order to have an optimal final design, taking into account the $T-\omega$ graph reference and respecting the thermal limit, through the calculation of the mean temperature in 15 selected WLTP points, inside the characteristic.

Chapter 2

Background

In the following chapter, a brief introduction of the components of the electric traction line has been made. After that, the attention has been shifted to the most common electric drives for EVs with a particular focus on the topology chosen for this thesis work, the IPM. It has been described its structure and working principle. Furthermore, analytical considerations has been made in order to find the dynamic model and torque equations. The control techniques have been shown and ,finally, the benefits of the chosen V-type IPM geometry have been explained.

2.1 The electric traction line

Since Toyota has put on the market the successful Prius, in 1997, full electric and hybrid vehicles have faced an increasing popularity during the years. Especially in the last decade, the entire car market dealt with huge changes, focusing more on them. There are multiple reasons for that: as primary motivation, the regulations for reducing the CO₂ emissions in air, forced the automotive industry to pursue research towards this field; another reason could be find in the performance that electric vehicle can assure, for example, in terms of acceleration, but also of adaptability to new technologies. In order to have a complete idea of their functioning, it is better to explain what are the main components of an electrical vehicle.

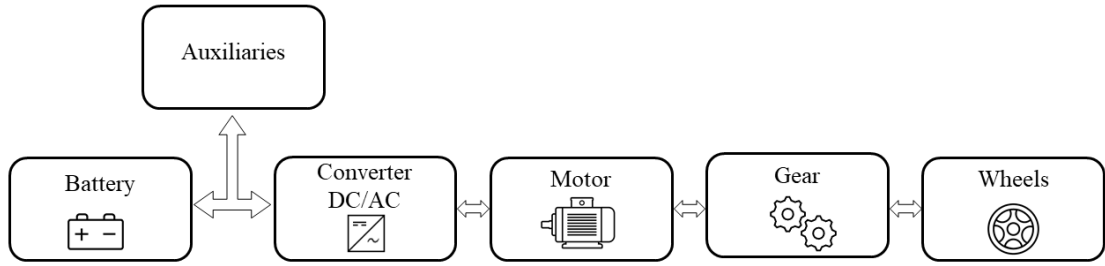


Figure 2.1: Electric traction line.

The electric traction line is composed by:

- Battery:** It is where the energy of the entire system is stored. According to the working point of the vehicle, it can be used either as a source of energy or to store it during a regenerating braking. A way to characterize the batteries is considering its specific power. Nowadays the biggest problem in those kind of vehicles is finding space for each component. In particular, the batteries define the autonomy of the vehicle, so a good trade off between it and space available on board is required. Consequently, they are required to be as small as possible; thus, a fundamental parameter to be taken into account is the energy density and the specific energy. The former indicates how much power can fit in a defined volume, whereas the latter gives an estimation of the weight needed for a certain amount of energy. The aim would be having small and light batteries. Nowadays, the goal can be reach. As far as the constructive technology is concerned, the most used type is lithium based one, in particular the Lithium ions or polymers. In the past, the Sealed lead acid were used as well. The Lithium based can reach very good levels of energy density, aS $600 \frac{Wh}{L}$, but also higher ones if the lithium phosphate and zinc based batteries are considered. Fortunately, these technologies also have a limited specific energy, making them compact too. In the future trends, it will be possible to consider silicon based anodes and nickel based cathodes, making the batteries even more suitable for EVs [4].
- Auxiliaries:** with the term auxiliaries, it has been considered all the items, inside the vehicle, that are not fundamental for the correct functioning of the car. They can be split in two categories, depending on the voltage level at which they should be supplied. The low voltage one includes the lights,the electric parking brake, the audio, the windows heating;in the high voltage one, the air conditioning. They usually need a stage of conversion because the voltage required could be lower (or higher) than the battery one.
- Converter:** A stage of conversion (or more) is necessary in the electric

traction line for several reasons. First of all, the source of energy is the battery, namely a DC voltage source, whereas the motor is usually a AC drive. In this sense, using a converter, or better an inverter, is fundamental in order to have an AC supply. There could exist also a DC-DC boost converter to excite the motor with higher voltages and make it work with higher efficiency. Furthermore, employing an inverter has made possible using those drives that rotate synchronously at the frequency of supply. Even in the case of a DC motor, a converter will be used, in this case a DC-DC booster, in order to have a proper level of voltage for the machine. Another converter that could be utilized is the one for auxiliaries, usually supplied at 12 V, so in low voltage. They are based on semiconductors, which means that, unfortunately, they are a source of heat as well. As a consequence, the heat dissipation of those is something to be carefully taken into account with a proper cooling system [5].

- **Motor:** This is the heart of the electric traction line and of this thesis work. It could be an AC or DC motor. It is required to have specific features both from torque and power point of view, but also as far as the efficiency, the maximum speed, the torque density are concerned. For these reasons, it should be well designed. As main topic of this work, a detailed description of what are the most used drives for EV and their features will be given in paragraph 2.2.
- **Gearbox:** The gearbox is the component of the electric traction line that has the duty of modifying the magnitude of the torque and speed that reach the wheels. In fact, the motor usually rotates at high speed; if it was directly coupled with wheels they would inexorably slip. What is usually done is adopting a fixed gear ratio, equal in every condition, between the motor and the wheels. So, this is a peculiarity for the electric vehicles. In fact, the motor delivers its maximum torque already starting from the zero speed, which means that they reach higher performance than the ICE ones.

2.2 Electric motors in electric vehicles

Because of increasing importance of the EVs, it is possible to say that for every component of the power-train there have been significant improvements. A special mention goes to electric machines. In order to be complaint to certain peculiarity needed for this type of vehicle, mainly as far as cost and space are concerned, they have been the centre of an intense research throughout the years.

To be more specific, the electric machines used for this application are firstly required to be highly efficient and reliable so they must handle big overloads. From the power, torque and speed points of view, determined features are strictly necessary: in order to have a proper acceleration, high rated torque and high

starting torque are common features in this sector. High power at cruising speed and constant power speed range (CPSR) are certainly required to achieve higher maximum speeds, machines must be easily flux weakened [2]. Obviously, high specific power and power density are pursued in order to make the vehicles more compact and lighter. It has to be said that the researches spread out towards the most common machines, ranging from DC and AC machines. In figure 2.2, it is reported a scheme which gives a full and detailed picture of what are most used ones for EVs.

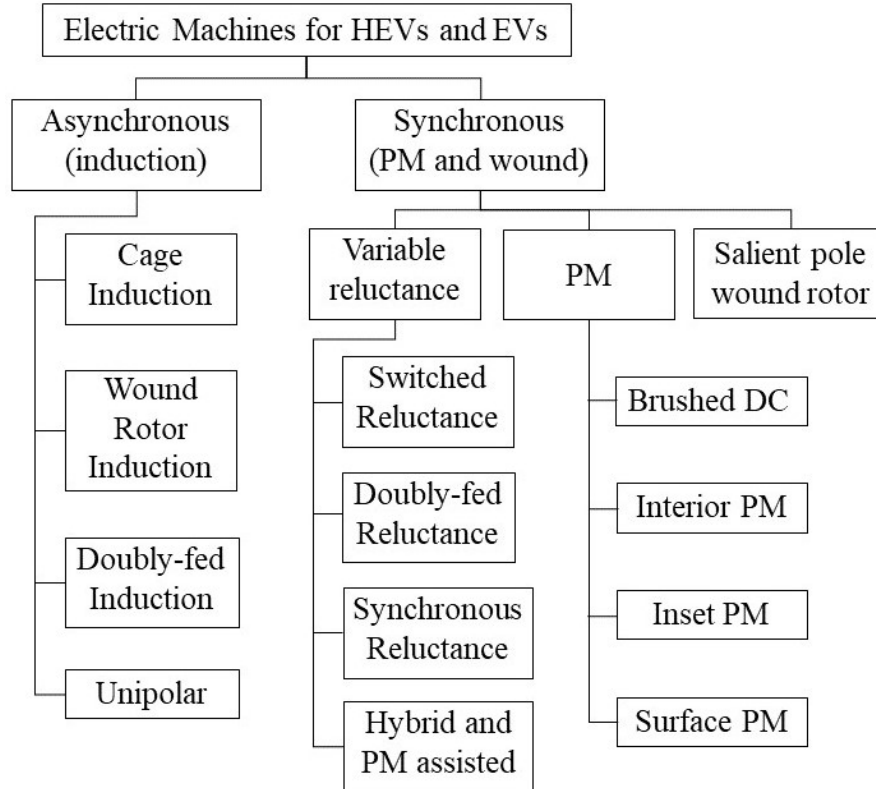


Figure 2.2: Electric motor suitable for EVs and HEVs (adapted from [6]).

As it can be seen, there are two main categories: induction and synchronous machines. In particular, the latter shows a further division depending on presence, or less, of the permanent magnets (PM). This kind of motors have been widely explored in the last decade. In fact, it has been noticed a shift from induction machines, especially used in the first generation of EVs, to PM machines with heavy rare earth magnets, like Samarium Cobalt and Neodymium Iron Boron, for traction use. This is due to all the benefits PM motors permit; they will be fully discussed later.

After having taken into account this distinction, it is reasonable to make a summary

saying that, in modern vehicles, there are basically three type of motors:

1. Induction machines;
2. Reluctance machines;
3. Permanent magnets machines.

Finally, new designs are still under examination and so the scheme is intended to become wider.

2.2.1 Induction motors

The induction motors are most widespread machines in the industry and ones of the oldest motors, with a huge history behind them. For these reasons they could also be applied for traction application. One of its first automotive application was the GM EV-1, the first full electric car produced in the US; the earlier models of Tesla Motors adopted them too [2].

It is a three phase AC machine, without separate excitation, and the its rotor could be of two types: squirrel cage or wound rotor. The former is the only one that find a place in the power-train. The easiness of the construction is one the biggest advantages of using them; unfortunately, the efficiency and the power density seem to be the most worrying drawbacks [7]. To solve this, the material chosen for the rotor is principally copper, because it allows to have lower motor losses, of about 20% [8]; this is due to the high conductivity of it. Consequently, if the rotor has been finely designed, high efficiency can be reached. This is a searched feature for electric vehicles, especially in machines like this, where the losses come both from stator and rotor. However, there are other benefits, like the possibility to easily skew the stator, in order to let the torque ripple decrease. The induction motors are very silent too and they do not present an electromotive force (EMF) when not excited, due to the absence of source of magnetic flux like permanents magnets [9].

2.2.2 Reluctance motors

Another typology of machine used for the traction of these vehicles is the one based on the reluctance principle. According to that, in an electromagnetic system, in presence of a movable armature, the latter moves towards the position where the inductance of the windings, in which the current flows, is maximum. The particular configuration represents also the position of minimum reluctance. A lot of motors based on this idea already exist, but, from an industrial point of view, especially from the automotive one, there are two main drives:

1. Switched reluctance machine (SRM);



Figure 2.3: Tesla induction motor [10].

2. Synchronous reluctance machine (SynRM) ;

As it can be possible to realize, one of the advantages of these machines is the absence of the permanent magnets inside the rotor that, consequently, have a very simple structure, being formed only by steel laminated sheets. In fact, there are windings only on the stator side. However, the constructive form of both stator and rotor differs depending on the motor type. The main difference between them is that SRM is a salient pole machine, contrary to SynRM that is a no-salient one.

SRM

Focusing on SRM machines, they present a double anisotropy, both on stator and on the rotor. The stator windings are of the concentrated type, wound on each pole. The stator and the rotor consist of packs of laminated iron sheets which have a number of different salient poles on their periphery, facing the air gap. The advantages of them are that they are easily built, robust, reliable, low cost and high efficient. From the automotive point of view, these motors have high CPSR, but the noise and torque ripple are still relevant problems and, consequently, the latest studies have been focusing on that in order to make these machines usable for the modern electric cars[11] [9].

SynRM

Moving to the SynRM, it presents anisotropy only on the rotor and it is obtained through holes of different shape that create air barriers, in order to make the magnetic flux flows in the direction on the direct axis (d-axis). So, it is reasonable to think that all the construction is aimed to maximize the ratio between the inductance on d-axis and one on the q-axis.

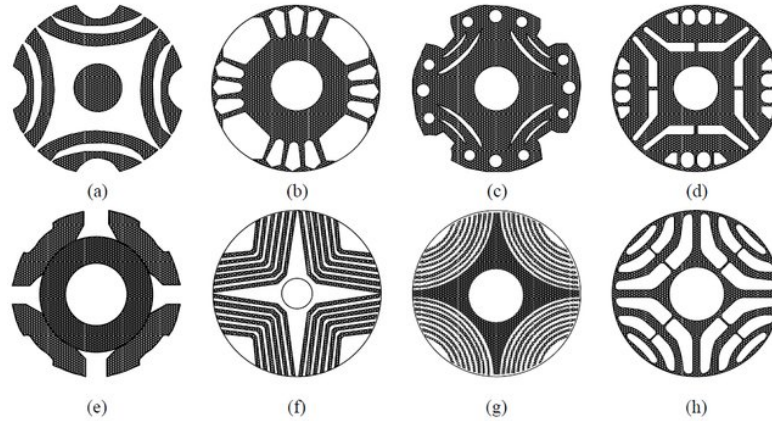


Figure 2.4: SynRM rotor designs [12].

They find a place in the automotive field, thanks to their robustness, high efficiency, but also for the fact that the torque ripple is well contained. The control does not affect so much the cost as well. Unfortunately, the power factor is low and this leads to problems in the performance. Furthermore, their CPSR is not well extended and, as known, it represents a relevant issue in the traction field [2].

2.2.3 Permanent magnets synchronous motors (PMSM)

Looking at the current electric cars present on the market, it is reasonable to say that most of them are fitted with an electric motor that based its functioning of the permanent magnets. In the power-train sector, all the studies have been concentrating on this type of motors because of multiple benefits they provide in terms of performances and efficiency [3]. In order to give an example, it sufficient to say that many car manufactures, like Toyota and Tesla have adopted them in most of their vehicles; especially the former can be considered a pioneer in this area, since the first mass-produced hybrid car, Prius in 1997, mounted this type of motor as part of the drive-train.

In order to understand the basic principle of PMSM, it is better to explain what is a permanent magnet. A magnet is a body that generates magnetic field. A permanent magnet is defined as a body that has been magnetized and therefore creates its own autonomous magnetic field. In this sense, there are two sources of magnetic field in a PMSM: the first one is the stator, which produces a rotating magnetic field. It works in the same way as it does in every other electric machine. The second one is the rotor, through the permanent magnets. From the interaction between the two magnetic fields, a mechanic torque is generated and transmitted to the shaft.

Despite all the classifications that it is possible to make about permanent magnets motors and despite all the new combinations of motors that have been developed lately, it exists only two broad categories that must be mentioned:

1. Surface permanent magnet motors (SPM) ;
2. Interior permanent magnet motors (IPM) ;

As it can be realized from their names, the main difference between them refers to the position of the magnets in the rotor. It leads to several benefits and drawbacks that will be explained in the following paragraphs.

SPM

The SPM motors presents a straightforward rotor structure, being the permanent magnets located on the surface of the rotor, as it can be seen in Figure 2.5.

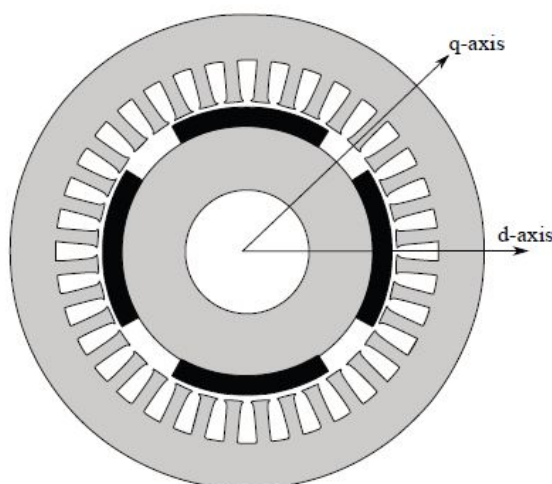


Figure 2.5: Cross section of a SPM motor [13].

Due to this particular structure, its rotor is isotropic, which basically means that the reluctance is constant and not depending of the position. As a consequence, there will not be any torque component related to the reluctance principle. Furthermore, because of rotor composition, the magnets will be more subject to the centrifugal forces, creating a considerable mechanical problem, especially at high speeds. In order to get rid of the inconvenience, retaining sleeves are used and the magnets maintain the original position [14]. Another issue related to them, is the presence of an electromotive force at no load and at no current. Focusing more on the construction details, the typology of permanent magnets used for them is usually

neodymium iron boron or samarium cobalt. Unfortunately, at high speed the rotor presents high losses; magnetomotive force (MMF) space harmonics and current time harmonics are the reasons of the inconvenient. Thus, the maximum speed of the SPM is highly limited[13]. Related to that, because of the peculiar position of the magnets, the air gap seems to be larger, having a bad effect on the motor performance, and so on its CPSR [2] . In order to solve the particular issue, from the stator point of view, fractional-slot concentrated windings (FSCW) are preferred [15]. Thanks to that, it is possible to achieve higher constant power speed ranges. Another effect of the peculiar choice is having short end windings; as a consequence, low Joule losses will be reached and an high fill factor can be obtained as well. A proper choice of the number of slots per pole is something to be taken accurately into account too [15].

Considering the level of efficiency achievable, SPMs can reach high ones, especially with sophisticated materials. Furthermore the torque density is noteworthy and the ripple that affects the torque can be reduced by means of stepping and even with harmonic compensations [16]. The noise is reduced as well; it is an important aspect to be considered for application of this kind.

This could make us think they are very good candidates for the traction of electric vehicles. On the contrary, through the years, there has been few models that still mount this typology for the power train. The main reason is surely the cost that affect the rotor construction. It is not related to the realization of the structure itself, but to the materials used. Because of the fact that the magnets are mounted on the surface of the rotor, the quantity needed for the whole motor is surely bigger than other topology workable, like the interior permanent magnets motors. From a geopolitical point of view, the cost of the PMs is increasing, and ,so, the entire research has shifted in the direction of solutions capable of exploiting the enormous benefits of permanent magnets, but reducing their use, taking advantage from the reluctance principle as well. So, other alternatives, like the interior permanent magnets, have been investigated.

IPM

As it has said in the paragraph 2.2.3, the position of the permanent magnets defines the different typology of PMSM. In the case in which, the PMs are moved from the surface of the rotor and embedded inside of it, another category called interior permanent magnet motors is obtained. Considering their extreme importance in the automotive field, a detailed focus about their structure, geometry and working principle find space in paragraph 2.3.

2.3 Interior permanent magnets motor

During the last years, the electric machine that more than the others rose to prominence is the interior permanent magnet motor. It has already been said, most of the modern electric vehicles use permanent magnet motors; but, in particular, the above-mentioned one seems to be the proper candidate for traction purposes. In order to give some examples, it is sufficient to say car companies like Tesla and Toyota adopt it for the latest models [17]. Before showing all the benefits but also the drawbacks of the their use in the automotive field, it has been preferred to present some key concepts, as the working principle, the dynamic model, the torque composition and, of course, the structure itself, in order to have a better understanding of the increasing popularity.

2.3.1 Structure of an IPM

As it has been said in the paragraph 2.2.3, in the IPM, the magnets are located inside the rotor. It follows that modifying the position of those within it, will surely affect the performance of the electric machine. In fact, the rotor shape is the key factor to be taken into account for the design process [18]. It follows that its structure has been the centre of studies and different arrangements have been proposed in order to find new solutions. The figure 2.6 shows two basic examples

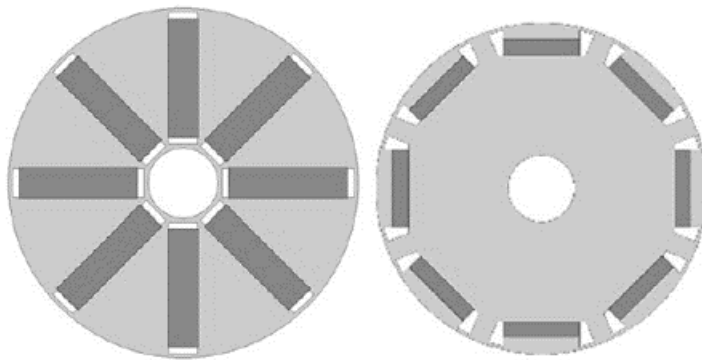


Figure 2.6: Basic structure of an IPM [19].

of what kind of structure can be obtained moving the magnets inside the rotor. What stands out observing it is its anisotropy. This is precisely the result you wish to achieve with the PM-embedded motors. The reason is straightforward: it will be, now, possible to take advantage from the reluctance principle. In order to give a better explanation of that, the concept of the saliency will be now introduced.

Saliency

Saliency is a peculiar feature of electric motors, in particular, in the case of PMSM, it can be considered a key factor for several reasons, especially as far as the control theory is concerned [20]. Taking into account the d-q axes frame, the saliency is defined as the spatial distribution of the inductance from the stator terminals point of view. The ratio between the inductance of d-axis and the one on q-axis is called saliency ratio.

$$\xi = \frac{L_q}{L_d} \quad (2.1)$$

It naturally follows that, for PMSM, the element that defines ξ is the rotor shape itself. In machine like the SPM, where the rotor is perfectly isotropic, the saliency ratio can not be that 1, because L_d is equal to L_q . While, interior permanent magnet motor presents a saliency ratio which is between $2 \div 3$. It means that only with IPM is possible to obtain an additional contribute to the torque, that is the reason why most of vehicles adopt that machine. As a consequence, the choice of the saliency ratio will affect some aspect. Sometimes, an high one is preferred to a low one. To give some examples, an IPM machines with an high ξ can lead to high efficiency and power factor in the constant torque application, but unfortunately also to an increased cost, due to the materials. Whereas, in the case in which a constant power is sought, having an high ξ can be the cause of low CPSR [21].

Rotor shapes in literature

As previously mentioned, a lot of studies have been conducted on the particular rotor geometry obtainable varying different parameters, like the number of the magnets inserted, the inclination of those and also the distance between them. As a consequence of that, it is not straightforward coming up with a proper and comprehensive classification of all the possible solutions for the design of the rotor. It is surely true that the entire process of design have greatly evolved: it has gone from easy flat-type geometries to complex ones. Anyway, a broad classification can be done, in particularly, looking at the solution for automotive field. The figure 2.7, shows the most common trends in the IPM rotor shape, especially for traction application.

Thus, the most common used geometries for traction purposes are:

1. V-shape;
2. Delta-shape ;
3. Double magnet shape.

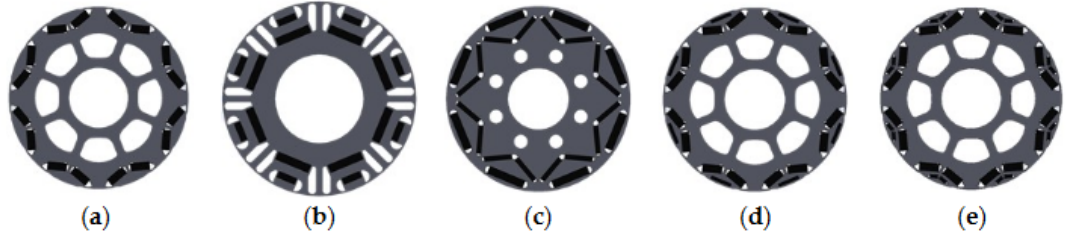


Figure 2.7: Rotor shape trends for IPM [18].

The case **(a)** represents a V-shape type and can be found in some models like the Tesla model 3, the Toyota Prius III and in Audi A3 e-tron. Case **(b)** stands for a double magnet shape; the **(c)** one for a delta shape, chosen for the Nissan Leaf model. The **(d)** type is called hybrid v-shape with magnet bar whereas the case **(e)** represents a double V-shape shape, applied in BMW i3 [22][18].

Air barriers

It is possible to observe all these structures are not composed only by permanent magnets. As first thing, during the construction, every iron sheet that compose the rotor, is punched, so, holes come of the shape wanted and in those are, then, applied the PMs. The latter, deliberately, occupy less space than the one effective. In this way, air barriers will be created. First of all they represent a way, thanks to which is possible to cool down the machine. As their name suggest they constitute a barrier to the magnetic flux flow. It follows they can be helpful to direct the magnetic flux itself towards a specific direction. In fact, during the design process of an IPM, a lot of attention is given to the saturation of the iron in rotor core, especially in the gap between the magnets, called center-post, and the bridges. This is done in order to increase the reluctance torque. Their saturation depend on the width of the air barriers. Taking into consideration the center-post, to have a proper saturation it is necessary having a large air barriers. It means having a narrow center-post. This is helpful in terms of torque because, thanks to this structure, it will be possible to push the magnetic flux, produced by PMs, in the direction of the airgap, enhancing the torque production. However, having parts of rotor of small width could subject them to high centrifugal forces, creating non negligible mechanical problems, in particular at high speed [23].

PMASR machines as alternative to IPM

As already said above, despite the fact the IPM motor is the most used motor for electric vehicles purpose, nowadays the researches are pushing in the direction of new solutions. Because of the increasing price of the rare earth materials, needed

for the construction of PMSM, it is desirable relying less on torque due to PMs and increase the one coming from the reluctance principle, even more than IPM already does. In this context, another machine, alternative to IPM, is the Permanent Magnet Assisted Synchronous Reluctance motor (PMASR).

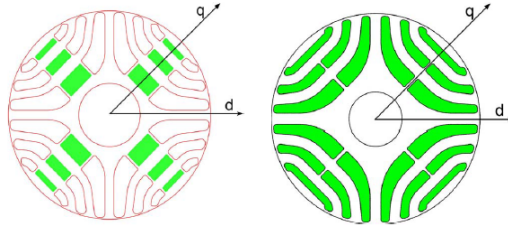


Figure 2.8: Examples of PM assisted Synchronous reluctance motors [24]

In this machine, the relevant torque component comes from the reluctance principle: the saliency ratio is much bigger than the IPM one. However, the presence of small amount of magnets seems to be necessary, in order to get rid of some issue, typical of a pure SynRM, like the oversize of the supply inverter [24]. Furthermore, it could be possible to increase the power factor and have a larger CPSR than the traditional SynRM [25].

2.3.2 Dynamic model

The electric and magnetic equations for the IPM machines will be now obtained. It has to be said the process is basically the same for every brushless machine; the only different consist in the possible anisotropy of some machines, like the IPM ones. At the beginning, in order to make the explanation clearer, an isotropy machine with sinusoidal distributed windings is taken into account. The hypothesis of magnetic linearity is considered. For a three-phase windings, it is possible to write the following voltage law:

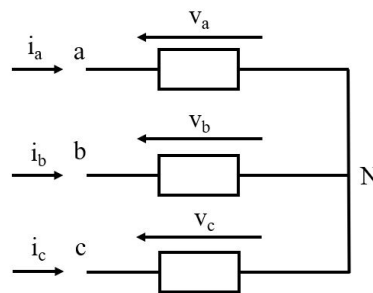


Figure 2.9: Three winding of the stator

$$\begin{aligned}
 v_a(t) &= Ri_a + \frac{d\lambda_a(t)}{dt} \\
 v_b(t) &= Ri_b + \frac{d\lambda_b(t)}{dt} \\
 v_c(t) &= Ri_c + \frac{d\lambda_c(t)}{dt}
 \end{aligned} \tag{2.2}$$

where R is the stator resistance and it is equal for all the winding, i_a, i_b, i_c are the phase currents and λ_i is the linkage flux, for each phase. It follows the total voltage of each phase is due to a resistive drop and a eletromotive force, given by the time variation of the linkage flux.

Let us now analyse the relationship between the linkage flux, the magnets and the current. The former is composed by the contribute coming from the stator resistance and the one from the permanent magnets. In the case of no load condition (so no currents are applied), the flux linkage will be all produced by the PMs and it will be sinusoidal. Indeed, as the anisotropy has been not introduced yet and the distributed winding are sinusoidal, it is possible also state that the self-inductances will be equal to each other; the same thing can be said for the mutual inductances.

$$\begin{aligned}
 \lambda_a &= L_a i_a + M_{ab} i_b + M_{ac} i_c + \Lambda_{PM} \cos(\theta_m) \\
 \lambda_b &= L_b i_b + M_{ab} i_a + M_{bc} i_c + \Lambda_{PM} \cos(\theta_m - \frac{2\pi}{3}) \\
 \lambda_c &= L_c i_c + M_{bc} i_b + M_{ac} i_a + \Lambda_{PM} \cos(\theta_m - \frac{4\pi}{3})
 \end{aligned} \tag{2.3}$$

where, Λ_{PM} is the amplitude of the flux due to the PMs.

It has been said that:

$$L_a = L_b = L_c = L_s \tag{2.4}$$

$$M_{ab} = M_{ac} = M_{bc} = M_s \tag{2.5}$$

Substituting the 2.4 and 2.5 in 2.3, it follows:

$$\begin{aligned}
 \lambda_a &= Li_a + M(i_b + i_c) + \Lambda_{PM} \cos(\theta_m) \\
 \lambda_b &= Li_b + M(i_a + i_c) + \Lambda_{PM} \cos(\theta_m - \frac{2\pi}{3}) \\
 \lambda_c &= Li_c + M(i_b + i_a) + \Lambda_{PM} \cos(\theta_m - \frac{4\pi}{3})
 \end{aligned} \tag{2.6}$$

Because of the absence of the neutral, the sum of the phase currents is zero:

$$i_a + i_b + i_c = 0 \quad (2.7)$$

and, so:

$$\begin{aligned} \lambda_a &= Li_a + M(-i_a) + \Lambda_{PM}\cos(\theta_m) \\ \lambda_b &= Li_b + M(-i_b) + \Lambda_{PM}\cos(\theta_m - \frac{2\pi}{3}) \\ \lambda_c &= Li_c + M(-i_c) + \Lambda_{PM}\cos(\theta_m - \frac{4\pi}{3}) \end{aligned} \quad (2.8)$$

Considering the first harmonic and knowing the third ones are not contributing, it follows:

$$M_1 = -\frac{L_1}{2} \quad (2.9)$$

and, as a consequence, the L_{eq} can be defined as follow:

$$L_{eq} = L_1 - M_1 = \frac{3L_1}{2} \quad (2.10)$$

Thus, the magnetic equations are obtained:

$$\begin{aligned} \lambda_a &= L_{eq}i_a + \lambda_{PM,a} = L_{eq}i_a + \Lambda_{PM}\cos(\theta_m) \\ \lambda_b &= L_{eq}i_b + \lambda_{PM,b} = L_{eq}i_b + \Lambda_{PM}\cos(\theta_m - \frac{2\pi}{3}) \\ \lambda_c &= L_{eq}i_c + \lambda_{PM,c} = L_{eq}i_c + \Lambda_{PM}\cos(\theta_m - \frac{4\pi}{3}) \end{aligned} \quad (2.11)$$

Finally, substituting the 2.11 in 2.2, the electrical equations can be written:

$$\begin{aligned} v_a(t) &= Ri_a + L_{eq}\frac{di_a(t)}{dt} + e_a \\ v_b(t) &= Ri_b + L_{eq}\frac{di_b(t)}{dt} + e_b \\ v_c(t) &= Ri_c + L_{eq}\frac{di_c(t)}{dt} + e_c \end{aligned} \quad (2.12)$$

where e_i :

$$e_i = \frac{d\lambda_{PM,i}(t)}{dt} \quad i = a, b, c \quad (2.13)$$

e_i is called back-EMF and it is the time-derivative of the flux produced by the magnets. It has an effect on the stator side. It can be clearly seen, there will be a decrease of the voltage at the stator terminals, creating problem especially at high speed.

Now, a more compact formulation is needed:

$$[v] = R[i(t)] + L_{eq} \frac{d[i]}{dt} + [e] \quad (2.14)$$

where:

$$[v] = [v_a, v_b, v_c] \quad [i] = [i_a, i_b, i_c] \quad [\lambda] = [\lambda_a, \lambda_b, \lambda_c] \quad [e] = [e_a, e_b, e_c] \quad (2.15)$$

In particular, shifting from the matrix expression to a space vectors one, the equations present as follow:

$$\bar{\lambda} = L_{eq} \bar{i} + \lambda_{PM}^- \quad (2.16)$$

$$\bar{v} = R \bar{i} + L_{eq} \frac{d\bar{i}}{dt} + \bar{e} \quad (2.17)$$

At this point the reference frame can be changed, passing from a three dimensional one, to a bi-dimensional one (α - β). The passage will be done, so that the plane components will be the same of the space ones.

$$\lambda_{\alpha\beta}^- = L_{eq} i_{\alpha\beta}^- + \lambda_{PM\alpha\beta}^- \quad (2.18)$$

$$v_{\alpha\beta}^- = R i_{\alpha\beta}^- + \frac{d\lambda_{\alpha\beta}^-}{dt} \quad (2.19)$$

It is a common practise to make use of a d - q reference frame which rotates synchronously with the grid voltage vector. For the IPM motors, the d -axis matches with the rotor magnetic axis. As a consequence, the magnetic flux due to rotor will not have an imaginary component.

$$\begin{cases} \lambda_{dq}^- = L_{eq} i_{dq}^- + \lambda_{PMdq}^- \\ v_{dq}^- = R i_{dq}^- + j\omega \lambda_{dq}^- + \frac{d\lambda_{dq}^-}{dt} \end{cases} \quad (2.20)$$

The 6.28 shows the dynamic model of a brushless motor in d - q frame. It is possible to notice that $j\omega \lambda_{dq}^-$ has appeared. The new component is called motional term, and it takes into account the fact that the $d - q$ frame is rotating. The electrical equation in 6.28 is valid for every brushless motor; whereas the magnetic equation is valid in case of rotor isotropy and magnetic linearity.

In order to obtain the equations for the interior permanent magnet motor, the

anisotropy has to be applied. The inductance of d -axis will be different from the one on q -axis. In particular, the condition $L_d \leq L_q$ is always verified for these machines. So the equation 6.28 turns into:

$$\begin{cases} \bar{v}_{dq} = R\bar{i}_{dq} + j\omega\bar{\lambda}_{dq} + \frac{d\bar{\lambda}_{dq}}{d\tau} \\ \begin{bmatrix} \lambda_d \\ \lambda_q \end{bmatrix} = \begin{bmatrix} L_d & 0 \\ 0 & L_q \end{bmatrix} \begin{bmatrix} i_d \\ i_q \end{bmatrix} + \begin{bmatrix} \lambda_m \\ 0 \end{bmatrix} \end{cases}$$

Decomposing the electrical equation along the d and q axes:

$$\begin{cases} v_d = Ri_d + L_d \frac{di_d}{dt} - \omega L_q i_q \\ v_q = Ri_q + L_q \frac{di_q}{dt} + (\omega L_d i_d + \omega \lambda_{PM}) \end{cases} \quad (2.21)$$

The electrical equations 2.21, give the possibility to draw the equivalent circuit of the IPM machine. In particular, before doing that, it appears appropriate introducing a new quantity, called characteristic current (or short-circuit current) that has the following expression:

$$i_{ch} = \frac{\lambda_{PM}}{L_d} \quad (2.22)$$

The equivalent circuits are, then, shown:

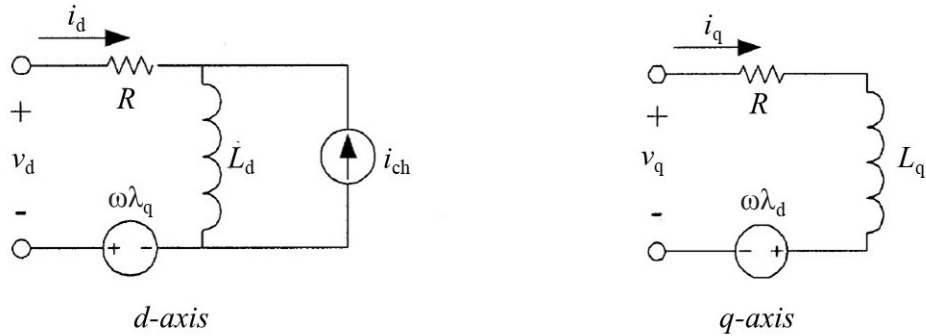


Figure 2.10: Equivalent circuits of an IPM motor [26].

As it can be possible to see from figure 2.10, the I_{ch} has been modeled with an ideal current source along the d -axis circuit. This parameter has a huge importance for IPM machines; in particular it affects the performance of the motor at high

speed. The back-EMF is present in both circuits and modeled with an ideal voltage source. In fact, as already said above, it basically decreases the v_d and v_q , influencing drastically some operating region, especially at high speed. In these circuits, the eddy currents and the iron losses are not represented; the only losses taken into account are the one due to the Joule effect, accountable for the increment of the temperature within the machine.

As far as the saliency ratio is concerned, it is possible to give an explanation of the reason why it is always bigger than one. Along the d-axis the magnets are located; they are seen like an additional airgap, that means the reluctance will be augmented and the synchronous inductance decreased. On the other hand, on the q-axis the magnetic flux does not meet an extra airgap, but only iron. In this scenario, the reluctance will be lower and consequently, the inductance higher.

2.3.3 From energy balance to torque expression

Once that the electrical and magnetic equations are written down, a proper expression for the torque can be found. As the title suggested, to do that, an energy balance has been employed.

The way of proceeding will be the same of the dynamic model: firstly an isotropic machine will be considered. Let us start from the equation 2.14, written referring to a three phase frame:

$$[v] = R[i(t)] + L_{eq} \frac{d[i]}{dt} + [e] \quad (2.23)$$

From a dimensional point of view, in order to obtain power, it is required to multiply both sides of the equation for a factor that represents the current, to be exact $[i]^t$.

$$[i]^t[v] = [i]^t R[i(t)] + [i]^t L_{eq} \frac{d[i]}{dt} + [i]^t [e] \quad (2.24)$$

Let us analyse the terms of the equation 2.24:

- $[i]^t R[i(t)]$ are the Joule losses,
- $[i]^t L_{eq} \frac{d[i]}{dt}$ is the time-derivative of magnetic energy, so the energy stored in the magnetic field,
- $[i]^t [e]$ is the electrical power transformed into mechanical one.

Focusing on the last quantity, it is also true that:

$$[i]^t [e] = [i]^t \frac{d[\lambda_{PM}]}{dt} \quad (2.25)$$

with λ_{PM} as function of the electrical angle θ .

So, multiplying and dividing for $d\theta$, it is possible to obtain the following expression:

$$\text{Mechanical power} = [i]^t \left[\frac{d[\lambda_{PM}]}{d\theta} \right] p \omega_m \quad (2.26)$$

where ω_m is the mechanical speed of the machine.

Dividing for ω_m , a first expression of the torque is obtained.

$$T = p [i]^t \left[\frac{d[\lambda_{PM}]}{d\theta} \right] \quad (2.27)$$

where p is the number of pole pairs. As already mentioned, it is desirable deriving an expression of torque, in a bi-dimensional frame. First of all, the $\alpha - \beta$ frame will be introduced and then the $d - q$ frame will be employed. Remembering what already said about the corrective factor in passing from a three-dimensional to a bi-dimensional environment, the expression of torque will be the following:

$$T = \frac{3}{2} p \bar{i} \times \frac{d\lambda_{PM}^-}{d\theta} \quad \text{or} \quad T = \frac{3}{2} p (\lambda_{PM}^- \wedge \bar{i}) \quad (2.28)$$

Considering the $d - q$ frame, it is preferred to align the d-axis with λ_{PM} . The expression of the torque changes as follow:

$$T = \frac{3}{2} p \lambda_{PM} i_q \quad (2.29)$$

If we consider anisotropy and write the energetic balance according the $d - q$ frame, the expression of the torque for the IPM machines will be obtained.

$$\begin{aligned} P &= \bar{v} \times \bar{i} = (v_d i_d + v_q i_q) dt = \\ &= R i_d^2 + L_d \frac{di_d}{dt} i_d - \omega L_q i_q i_d + R i_q^2 + L_q \frac{di_q}{dt} i_q + L_q i_q i_d + \omega \lambda_{PM} i_q \end{aligned} \quad (2.30)$$

So, the torque:

$$T = \frac{3}{2} p [\lambda_{PM} i_q - (L_q - L_d) i_d i_q] \quad (2.31)$$

Now that the torque expression has been retrieved, the reason why the IPM motor are so spread find a proper analytical explanation.

The two torque contributions can be clearly seen in 2.31: the former is due to the interaction between the flux produced by the permanent magnets and the one produced by the stator current. It would be the only contribution to the torque

in isotropic machines like the SPM ones. The other contribution comes from the diversity among L_d and L_q . In particular, this contribution is strictly connected to the saliency. If the latter augments, the torque due to the reluctance principle, will be higher, as it can be observed in the following equation, where the role of the i_{ch} is also pointed out.

$$T = \frac{3}{2}pL_d[i_{ch}i_q - (\xi - 1)i_d i_q] \quad (2.32)$$

However, it has to be said, the two components of the torque have different signs, which implies an opposite effect on the overall torque. In order to magnify the quantity of available torque, a lot of attention has to be spent on the proper control of the $d - q$ currents.

Torque ripple

The term torque ripple refers to a periodic interference in the magnitude of the torque, that does not have a static value. This disturbance causes problems to the motor itself: not having a constant torque implies noise and also attrition of bearings. In order to understand the phenomenon, it is possible to think about the torque as composed by two terms:

- a DC component, namely, the amplitude component
- a frequency component

As the equation 2.27 shows, the responsible for torque ripple could be either the stator currents or the back-EMF. It is desirable having them as most sinusoidal as possible, in order to avoid the presence of harmonics in the torque that causes the issues [27]. Unfortunately, imperfection of windings or of back-EMF are always possible, so a lot of method to decrease the torque ripple have been proposed. Most of them base on the control theory or on the rotor design. In order to give some examples, the [28] proposes eight major rotor design by means of Latin hypercube sampling method, studying how the design variables are sensitive to the torque ripple. The [29] proposes an improved direct torque control (DTC) for the reduction of the torque ripple.

Cogging torque

Another disturbance that affects the torque, is the cogging torque. This is caused by the interaction between the permanent magnets on the rotor and the stator slots. To be more precise, it is the tendency of the rotor to stop in determined

position and it exists also when the machine is not excited. This is due to the different magnetic local situation, that changes with the rotation of the rotor [30]. In fact, the phenomenon appears when permeability of the air-gap is not constant. Also for this issue, the effects are vibration and acoustic noise. As a consequence, it can lead to resonance too. It follows that it has to be minimize as much as possible. One of the most used technique to eliminate the problem consists in skewing the stator (or rotor). The aim would be to average the local situation along all the axial machine length. Other solutions can be found in literature: [31] proposes an interesting way of design the stator, based on mathematical system called R-D (reaction and diffusion). In [32], an asymmetrical v-type rotor geometry has been proposed in order to decrease the cogging torque.

2.3.4 Control theory of IPM

A fundamental aspect to be taken into account in order to obtain the performance wanted is the control of the machine itself. The way of doing that, varies according the purposes and the situations. Before focusing on them, it has been preferred to introduce some basic principles. In figure 2.11 are shown the traditional torque-speed graph and power-speed graph.

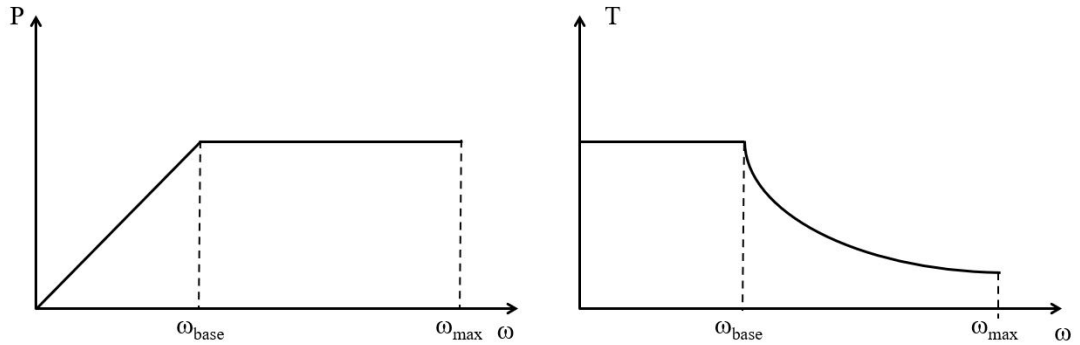


Figure 2.11: P - ω and T - ω of IPM machine.

From the picture 2.11 is possible to observe some particular features of the IPM machine. The ω_{base} can be defied as the speed at which the rated torque and the rated speed have reached. Furthermore, at ω_{base} the rated voltage given by the converter has been reached. So, the quantity defines two operating areas:

- One at constant torque;
- One at constant power.

It will be used a proper control law for each of the operating areas. Before explaining which principles are employed, it is appropriate focusing on the limits of the machine, because they give an idea of how behaving during the two operating area.

Current limit

It is known there are limits for the proper functioning of an electric machine in voltage and current that must not be exceeded. It follows that they also draw the limits for the working points, defining the operating range. Often, those values are represented by the rating ones. In order to determine these limits, the hypothesis made is to consider all the quantifies steady, namely, a condition in which the voltages and currents do not vary in amplitude or frequency. In these conditions we have a constant speed.

Starting from the current limit, the expression for the maximum current available is the following one:

$$\sqrt{i_d^2 + i_q^2} \leq I_{max} \quad (2.33)$$

$$I_{max} = \sqrt{2}I_{rated} \quad (2.34)$$

The equation 2.33 is represented by a circumference in i_d - i_q plane, with a radius that is exactly the maximum phase current.

Voltage limit

As far as the voltage is concerned, the limit is the following:

$$\sqrt{v_d^2 + v_q^2} \leq U_{max} \quad (2.35)$$

Thinking about the electric traction line, there is a strict relationship between the battery voltage, namely, the voltage of the DC-bus and the maximum available for the machine:

$$U_{max} \leq \frac{U_{DC}}{\sqrt{3}} \quad (2.36)$$

The limit is imposed in order to make the voltage vector to be in the limit [33]. Considering the electrical equations written on d - q frame(2.21), neglecting the losses substituting them in 2.36, the equation of an ellipse is obtained. In fact, the voltage limit for this machine is an ellipse. In case in which the machine had been

isotropy, it would have been obtained a circumference.

$$\sqrt{\left(I_d + \frac{\lambda_{PM}}{L_d}\right)^2 + \left(\frac{L_q}{L_d} I_q\right)^2} \leq \frac{V_{lim}}{\omega L_d} \quad (2.37)$$

The above mentioned ellipses have the center in $-\frac{\lambda_{PM}}{L_d}$ in the d - q axes frame. It comes from that, in reluctance motors, without PMs, the center would have been in the origin. The figure 2.12 shows what already said.

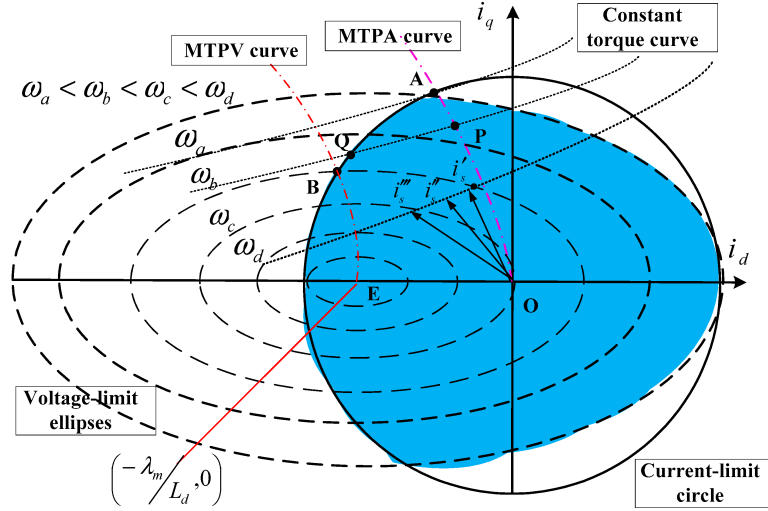


Figure 2.12: Current and voltage limits for the IPM machine [34].

As it can be seen, the constant torque curve are represented by hyperbole with one asymptote that is the horizontal axis and the other one that passes through the point $\frac{\lambda_{PM}}{L_q - L_d}$.

Now, that currents and voltage limits are defined, the control principles will be explained: to do that it has followed the above mentioned distinction between the two operating areas.

Constant torque zone

As seen in figure 2.11, the area in which the torque is kept constant is the one below the ω_{base} . At low speeds, the ellipses delimiting the voltage limits shown in 2.37, does not effect so much the functioning of the machine. It follows that in this area a proper control has to be done on the current and not on the voltage.

In particular, a strategy for controlling the current itself is the one based on the **MTPA** (Maximum torque per Ampere). As the name suggest, this is a locus of all the points that allows to have the best exploits of the current as far as the

torque is concerned. To some extent, it is possible to say that following the MTPA, the current will be optimally used and not wasted. In fact, from a thermal point of view, it gains importance because the copper losses are caused by the stator current and applying the minimum current to produce a certain torque will make them decrease. The equation 2.31 gives us some information about how the MTPA for IPM should be: thanks to the reluctance component of the torque, it is correct to say that not only the i_q will contribute to the final result but also the d axis component. The former scenario is typical for machines that does not show reluctance, like the surface PM motors. In fact, their MTPA basically coincides, on $d - q$ axes, with the q one, for obvious reason. It follows that, for IPM machine, adopting the MTPA law means finding the correct current phase angle.

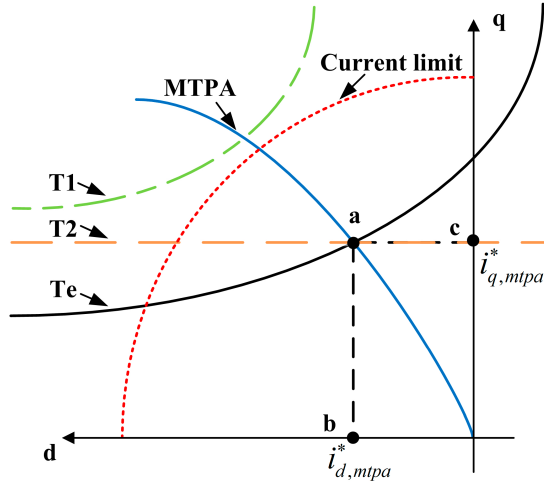


Figure 2.13: MPTA locus for IPM machine [35].

The figure 2.13 shows a detail of figure 2.12. What stands out is the fact that MTPA locus is not a straight line as it would be expected. In order to understand why, it is helpful to write again the equation 2.11, substituting the i_d and the i_q with their definitions as functions of the current phase angle γ :

$$\begin{aligned} i_q &= |i_{dq}| \cos(\gamma) \\ i_d &= |i_{dq}| \sin(\gamma) \end{aligned} \quad (2.38)$$

$$T_e = \frac{3}{2}p(\lambda_{PM} |i_{dq}| \cos(\gamma) - \frac{1}{2}(L_q - L_d) |i_{dq}|^2 \sin(2\gamma))$$

and deriving the torque respect to γ :

$$\frac{dT}{d\gamma} = 0 \quad (2.39)$$

we obtain the MTPA condition. As a consequence, the angle γ_{MTPA} will change, following the torque. To an higher torque, corresponds an higher γ . The γ_{MTPA} for IPM will be around the 20-30°. Because of the saliency ratio, always higher than one for those motors, the i_d component should be negative in order to exploits the reluctance torque. Having a positive i_d will not lead to any benefit, because it would create a negative effect, fighting against the production of torque.

It follows that the ξ will affects the γ_{MTPA} as well. In particular, the higher it is, the higher will be MTPA angle.

Looking at figure 2.13, it can be clearly seen that the intersection between the MTPA locus and the constant torque curve will give the i_d and i_q components. As mentioned above, the only limits that occurs in constant torque zone is the current one. So, the components of the current vector will be controlled in order to stay on MTPA locus. The result is an improved efficiency for the electric machine.

Constant power zone

In the moment in which the base speed is crossed the MTPA law cannot be applied anymore. If we think about the performance wanted for an electric vehicles, having a wide CPSR is surely one of the most important.

It has been already mentioned that a back-EMF component exists and it is depending on the speed of the drive. At low speed, this quantity is extremely low and the stator voltage can easily provide for it and also for the voltage drop due to stator resistance. As the speed increases the back-EMF term increases as well and, consequently, the voltage applied to the motor will increase too. At the base speed, the voltage available from the V_{dc} bus, or more precisely, from the inverter, reaches its limit and so it is not possible to increment the voltage anymore. At this point, if it is needed to increase the speed of the motor, the only feasible way is to act on the flux, weakening it. In fact, if we look at equation 6.28 and consider the steady state, we will see that the flux is proportional to the voltage and inversely proportional to the speed. In this sense, the flux will naturally be weakened because of the voltage limit. This way of operating is called Flux weakening. The key concept is the following: since there are two sources of magnetic flux inside the machine and one of them cannot be changed (PMs one), you will be act on the stator one, namely, injected current will make the magneto-motive force decrease. In particular, to do that, a negative i_d component will be injected.

It follows that below the base speed, the flux is constant because both voltage and speed are increasing proportionally. Thus, if the flux and current (controlled through MTPA) are both constant, the torque is constant as well, as 6.28 equation suggests. Furthermore it also means that the power is increasing. But above the base speed the flux is decreasing as the torque, meaning that the power keeps on staying constant because speed rises.

In this sense a fundamental factor that affects the flux weakening capability is the above mentioned characteristic current(equation 2.22), also called short-circuit current, because it also indicates the values that are obtained by connecting the terminals of the machine in short circuit and putting it rotating by a second motor. It has already been said this is the center of the ellipses voltage limit. It is desired that this quantity is almost similar to the rated current, because it will lead to an higher CPSR.

To be more precise, a distinction can be made between drives:

- $i_{ch} < i_{rated}$: infinite speed drives;
- $I_{ch} > i_{rated}$: finite speed drives.

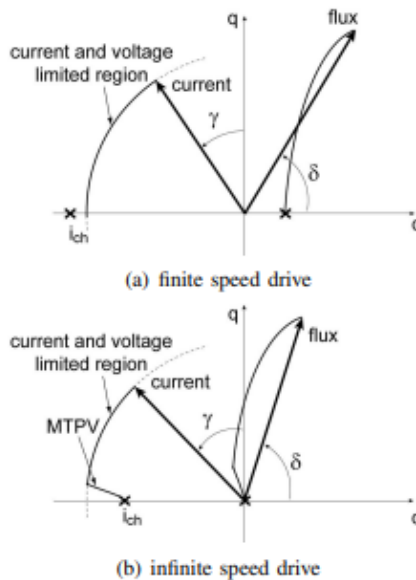


Figure 2.14: Infinite drive and finite drive [36].

In the former case, the center of the ellipes resides within the current limit circumference, whereas the latter one has it outside the area. For them, the possibility of control are different. In case in which the rated current was lower than the characteristic one, the drive could reach limited speed.

As it can be seen from figure 2.14, for finite speed drives the only possibility to have flux weakening is that of moving following the circumference of the maximum current available. In this case, there is a limitation in both current and in voltage. As already said, we are injecting negative i_d in order to flux weaken as much as possible. Unfortunately, at the end, the $-i_d$ will be only equal to i_{rated} . As a

consequence, in the flux weakening a limit exists for those machines. It is evident that flux has not reached the origin of the d - q frame.

On the other hand, if we follow the same reasoning but for the infinite speed drive, at some point, the current circumference and the MTPV curve intersect. The term MTPV stands for Maximum Torque Per Volt; it could be said that is a sort of counter part of MTPA, referring, this time, to the voltage. The locus represents the points in which the exploit of the voltage will be the highest; in this sense, we will manage optimally the voltage, retrieving the highest torque. It represents the best way to spend one volt inside the machine; it has been obtained through the ellipses that limit the voltage. During the MTPV operation, the quantity of $-i_d$ injected is decreased, namely, its absolute value increases, moving closer to origin. Because of that, the amplitude of the current vector will slightly decrease, meaning that it will not be constant anymore. However, the closer the i_{ch} is to the i_{rated} the more the power is constant. From figure 2.14, it appears that the flux will end up exactly in the origin. This is why, the drives are supposed to reach ideally infinite speed.

2.3.5 Chosen typology: V-type shape

As above mentioned, different typology of IPM machines can be realized and all of them are characterised by a particular rotor geometry. The rotor can be modified adding more magnets or adding, removing, changing the shape of the flux barriers. As a consequence, every category will have some benefits and drawbacks; it is always a matter of finding the proper trade-off.

It already been said that the interior permanent magnets motors present some features that perfectly match the needs in the automotive field, as:

- **High power and torque density:** the reason is always the same: the reduced space in the vehicle has pushed the research towards the direction of having smaller motors.
- **High specific power:** The reduced weight of the motor beneficially affects the performance of the vehicle.
- **High efficiency:** in order to not waste energy the electric machines must be efficient. In this case, the efficiency ranges between the 95% to 98%.
- **High CPSR:** To achieve higher speeds, the ratio must be as high as possible.

It seems that the geometry that enhances those characteristic is the **V – type** one. This is the reason why the design of the above mentioned electric machine topology has been carried out in this thesis work.

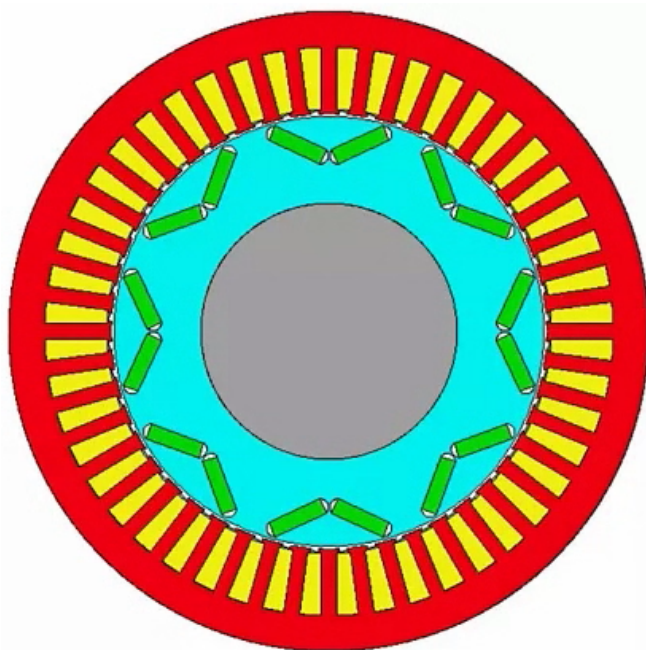


Figure 2.15: Example of v-type rotor geometry [37]

Analyzing the the v-type structure shown in figure 2.15 , it is possible to notice that every pole of the machine is composed by two simmetric magnets, facing each other, inclined of a certain angle; from it, the particular name of the typology. Furthermore, the inclination of those will have an affect on the torque production, since it will affect the inductance on the q axis and, as a consequence, the saliency ratio. In fact, acting on the two inductances is fundamental in order to improve the torque.

It would be feasible to modify the dimensions of the magnets, in order to have an higher production of flux, as well. However, it implies an increment of the cost of the whole machine. In this sense, it should be necessary to cover the polar pitch as much as possible with the magnets. It follows that the former strategy sounds clever. In fact, this structure is deliberately used because of the simplicity with whom the dimensions can be modified. The performance of the machine are highly influenced by the geometry. It means that it is easy to obtain an higher or lower torque, only adjusting the parameters of the rotor geometry. It follows that the machine lends itself to a straightforward optimisation.

However, it is always needed to find a proper trade off between the inductances on both axes. High values of saliency can be reached, because the magnets are placed along the d -axis which means that the inductance along that axis is low. This is due to the magnetic permeability, similar to the one of the air. It leads to an higher

reluctance and, consequently, a lower inductance. It follows that an increment of the number of the magnets barrier could involve a further increment of ξ . It is a solution that can be found in some applications and it is called **double V-type**.

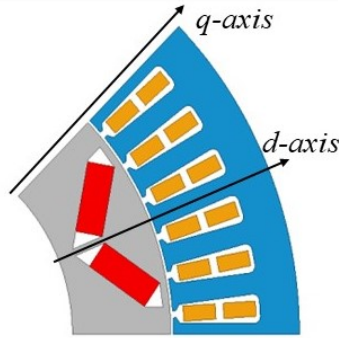


Figure 2.16: *d* and *q* axes orientation in V-type geometry. Adapted from [38]

In any case, having a low L_d leads to another problem: the decrease of the characteristic current. As known from the equation 2.22, the higher is the L_d , the lower will be the i_{ch} . As consequence, the machine will not reach higher speeds because it will not be capable of exploiting flux weakening as much as possible. In this case, the v-type geometry allows to overcome the problem granting a very high L_q , so that the L_d does not have to be so low for having higher torque. Indeed, the flux weakening capability is high in the typology considered, thanks to the possibility to let the magnetic flux flows along the tangential bridges. As a consequence, the constant power area will be higher and the CPSR will reach remarkable values as expected in the automotive field. Furthermore, the presence of the tangential bridges and the one in the middle of the two magnets are fundamental in order to avoid the magnetisation of them, during the injection of a negative i_d component.

For all of what it has been said, in this project, it has tried to realize a rotor design that enhances those features; so, the multi-barrier geometry seemed the more adapt for the particular application and we have focused on that.

Chapter 3

Traction design

In the following chapter, the desired motor performance have been investigated, in terms of torque, speed and power. A brief overview of the already existing solutions has been conducted. Then, the reference chosen has been the WLTP driving cycle, in order to represent faithfully the working conditions of the motor in the $T - \omega$ graph. To do that, the vehicle dynamics and an simple vehicle model have been introduced.

3.1 Trends in the EV market

Once that the type of electric machine has been chosen, before starting to think about which choices must be taken as far as the stator and ,especially, the rotor geometry are concerned, is necessary to define the main parameters of the $T - \omega$ and $P - \omega$ graphs. As already mentioned in chapter 2 and shown in figures 2.11, the parameters that have to be carefully noted are:

- the maximum power;
- the maximum torque;
- the base speed;
- the maximum speed.

The first thing to do is to define properly the particular application. In this case, the vehicle for whom the electric motor will be design is a urban/extra urban vehicle. As a consequence, the maximum speed will not reach values higher than $200 \frac{km}{h}$.

In order to broadly think about what features the electric vehicles should have, you may observe the already existing solutions in market and see what are the typical

trends. The cases of interest only deals with the BEV vehicles, because the motor design has been thought for that peculiar application. Referring to table 3.1, the main characteristic of the most common solutions in the market are summarized:

	Chevy Bolt	Nissan Leaf	e-Golf	Zoe	Fiat 500e
Market introduction	2016	2010	2014	2017	2020
Vehicle type	BEV	BEV	BEV	BEV	BEV
Peak Power (kW)	150	80	85	65	83
Peak Torque (Nm)	360	280	270	220	200
Max Speed (rpm)	11400	10400	12000	11300	12800

Table 3.1: Main performance data of EVs in the market[22][39].

Another interesting parameter to consider for the traction design is the acceleration. It is usually considered the acceleration needed to reach 100km/h ; in particular, the time needed is a key factor for starting the decision-making process. Here, in table 3.2, it is possible to observe the acceleration values, referred to the vehicles considered in the table 3.1.

Acceleration time (s)	
Chevy Bolt	6.4
Nissan Leaf	11.5
E-Golf	10.4
Zoe	13.5
Fiat 500e	8.9

Table 3.2: Acceleration time (0- 100km/h) [39].

What emerges is that for electric utilities cars, the power ranges from 60 – 150 kW and torque from 200 – 360 Nm. As far as the acceleration is concerned, 10 s is the average time to reach $100 \frac{\text{km}}{\text{h}}$.

3.2 Driving cycle

In order to estimate which could be the working points of a vehicle regardless the type of traction or the specific goal, it is better to take into account the driving cycle. The correct definition is the following: a driving cycle represents the working point of a vehicle, showing the speed it can reach related to time[40]. Depending on the area of interest, a different driving cycle will be considered. Every country, or

better continent, produces its own driving cycle. In fact, they are strictly connected with legislative approval of vehicles. This implies that they have to be tested, following the predetermined cycle for the country of interested, before having been put on the market of that area. Moreover, the cycles are used to estimate some features of vehicles as the fuel consumption, the pollutant emissions, but also the autonomy, especially in electric car.

In the case of study, the driving cycle has been used to have a rough idea of how much torque the motor must produce in order to pass the test, namely to understand what should be the minimum torque needed to make sure the test has been validated and the related speed.

WLTP

Since the 1980s, the driving cycle used in Europe to test the vehicles on the market has been the NEDC (New European Driving Cycle). It was based on theoretical driving; in particular, it was simulating a urban cycle and an extra-urban cycle. It has been used to test the vehicle till the emission limits EURO 6c. However, it does not represent faithfully the different operating condition of a vehicle. For these reasons, it has been developed a new driving cycle, called WLTP (Worldwide Harmonized Light Vehicles test procedure).

As the name suggests, it applies to every vehicles across the world. It has been introduced in 2017 with the intent of overcome the diversity among the several cycles used in the different areas. It is based on real-driving data and, as a consequence, it represents better the on-road performance. As the figure 3.1 shows, the cycle is divided into 4 parts, according to the speed reached. So, first part refers to an urban trip, the medium-high to an extra urban trip, whereas in the extra-high you can find the speeds normally reached in an highway. Furthermore, acceleration phases and deceleration ones are considered [41]. In this sense, it follows better the a real on-road situation.

It exists three different version of the WLTP, according to the PWr (power/weight ratio, expressed in $\frac{W}{kg}$):

- Class 1: $PWr \leq 22$
- Class 2: $PWr < 22 \leq 34$
- Class 3: $PWr > 34$

The case shown in figure 3.1, illustrates the WLTP driving cycle for a class 3, because it is the class of most of common cars on the markets and it is the one used for the vehicle for whom the motor has been designed [42].

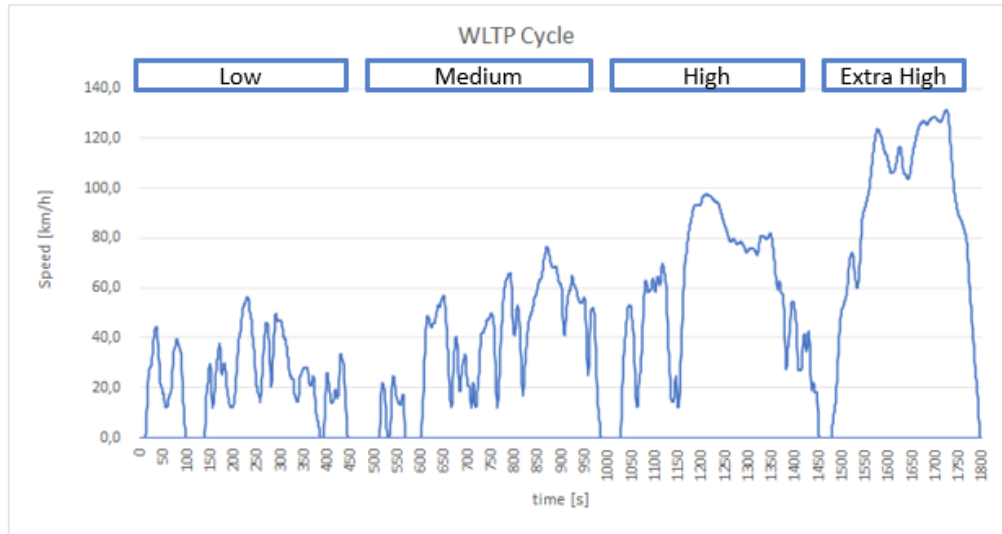


Figure 3.1: WLTP driving cycle.

3.3 Vehicle dynamics

The performance of the vehicle, and, consequently, the main parameters of the motor can be found applying some basic principles of vehicles dynamics. The term refers to the discipline that studies the behaviour of every kind of vehicle when moving, on the road, for automobiles or in the air, for an airplane. In particular, it deals with the response of the vehicle to certain inputs, given by the driver, like an acceleration, a braking, or a fast steering. Furthermore, other elements that have an influence on that are the weather, the road conditions for cars, or of the air in case of planes [43]. The reason why it has a relevant importance in the electric motor design is that it gives a broad idea of what could be the load whom the electric machine must sustain, in order to guarantee determined performance, like the maximum speed or acceleration. Moreover, the vehicle dynamics can also be useful to determine the energy needed and, so the autonomy, for a determined driving cycle.

Of no less importance, the vehicle modeling is a crucial choice to be taken into account. Thinking about the application chosen for this thesis, a car has an irregular shape, so it lends itself to different models ranging from a more complex one to those simpler. It is reasonable to say that the level of complexity depends on what has to be observed. In the case of study, the principles of vehicle dynamics have been applied in order to understand which torque and speed the motor must have in order to respect some fixed performance. As a consequence, it has been preferred

to model the vehicle using a lumped approach method; it means that the car has been considered as a rigid body, with its all mass concentrated inside its center of gravity. Moreover, the movement of the vehicle has been kept unidirectional, in order to have a functional and easy model.

3.3.1 Newton's second law

The basic principle used describe the dynamic of the vehicle is the **Newton's second law**.

$$m \frac{dv(t)}{dt} = ma = F(t)_{tractive} - F(t)_{resistive} \quad (3.1)$$

where:

- m is the equivalent mass (kg) of the vehicle considered;
- a is the desired acceleration ($\frac{m}{s^2}$).

As it can be possible to observe from equation 3.3.1, the acceleration of the vehicle itself is an effect of all the forces acting on it. In this case, the forces balance is straightforward because the analysis is conducted only along one direction. In particular it exists two main forces:

- $F(t)_{tractive}$: this is the sum of forces that keep positive the acceleration, making the vehicle advance.
- $F(t)_{resistive}$: this is the sum of forces that push against the advancement of the vehicle.

An example of $F(t)_{tractive}$ is the one produced by the motor itself and transmitted to the wheels by means of the shaft and gearbox. Whereas examples of $F(t)_{resistive}$ are the aerodynamic friction, due to the particular shape of the vehicle and the fluid in which it is flowing. Indeed, the friction caused by the rolling wheels has to be taken into account as well as the force due to the slope of the path. It follows that the advancement of the vehicle depends only on this balance: if the $F(t)_{resistive}$ was higher than the $F(t)_{tractive}$ the car would not continue proceeding ahead, instead, it would rapidly decrease its speed, until a new balance is reached.

Thus, it seems of remarkable importance underlining the nature of the three above-mentioned $F(t)_{resistive}$ because they are strictly connected to the vehicle features.

Slope force

In the case of an hill, the vehicle will be subjected to a resistive force that hinders its progress upwards. There is a tangential component in the direction of the move, due to the gravitational force acting on the vehicle mass, called slope force.

$$F_s = m_c g \sin(\alpha) \quad (3.2)$$

where the m_c is the vehicle mass at full load and expressed in kg , g is the gravitational acceleration in $\frac{m}{s^2}$ and α represents the inclination of the plane and it usually ranges from 25 % and 30%. Furthermore it is express in the following manner:

$$\alpha = \frac{h}{d} \quad (3.3)$$

where h is the height of inclined plane and d is the other cathetus of this imaginary triangle. In the moment in which the vehicle is crossing an ascent, the force can properly named resistive, whereas during a descent, it acts as an addictive tractive force.

Aerodynamic drag

When a vehicle moves in the air, it faces a barrier that tries to stop it; this resistive force is called aerodynamic drag. The effect has been studied a lot during the years, especially for some particular applications like in car races where every tenth of second matters and having the highest acceleration is something fundamental [44]. It has to be said that having a simple equation that summarize the effect of the aerodynamic drag is not an easy task, because of the several parameters to be taken into account. First of all, the car body can widespread change; in addition, the fluid can have a peculiar behaviour, due to its composition. As a consequence, the equation of the aerodynamic drag is based on empirical considerations.

$$F_s = \frac{1}{2} C_x \rho_\alpha A_f v^2 \quad (3.4)$$

where C_x is called drag coefficient, ρ_α is the air density, expressed in $\frac{kg}{m^3}$, the A_f is the frontal vehicle area and finally v is the vehicle speed, expressed in $\frac{m}{s}$.

Starting from the drag coefficient C_x , it represents the effect of the shape on the aerodynamics drag and gives an idea of how good shape itself is in reducing drag effect on the vehicle that is approaching. It follows that for some application having a low C_x is fundamental in order to make the vehicle faster. In this sense,

the car will not face a remarkable obstacle coming from the air, because its shape make the air flows without any particular resistance. On the other hand, having an higher C_x implies that the body shape is creating a resistance and, consequently, the vehicle will decelerate [45]. Thus, the drag coefficient is highly influenced by the vehicle shape. Due to the complexity of the its calculation, some empirical values have been found associating them with a simple geometrical shape. Nowadays, cars have a C_x that ranges from 0.20 to 0.30. In any case, having a low drag coefficient could be beneficial also from an efficiency and CO_2 emissions reduction, but it must face with the choices imposed by the market, in terms of passenger comfort [46].

The \mathbf{A}_f indicates the frontal vehicle area. As it can be possible to think, vehicles do not have shapes whose area can be straightforwardly calculated. As a consequence, in order to obtain the bi-dimensional impact area, a good choice could be to inscribe the whole area in a rectangle.

The $c\rho_\alpha c$ stands for air density. This quantity is affected by multiple parameter, like temperature, humidity and altitude. In automotive application, the value is basically the same and equal to $1.225 \frac{kg}{m^3}$, referred to a standard condition for dry air with a temperature of $15^\circ C$ at sea level.

Rolling resistance

With the term rolling resistance we refer to the friction force due to the rolling of the tyre on the road. To be more accurate, when the wheel starts to roll, it is subjected to a deflection caused by the gravitational force that pushes the vehicle downward. Indeed an additional force is applied to wheel by the movement of the vehicle. In this sense, while the car is proceeding forward, the effect of the weight decreases and, consequently, the tyre can recover its original shape. It follows that the cycle is losing energy, because during the alternation of deflection and restoring the original shape, the energy is employed to make the wheel roll. This process is called hysteresis and it is the main reason why the rolling resistance has to be considered [47]. Looking at equation 3.6, we can observe a way to define it:

$$F_v = C_v m g \cos(\alpha) \quad (3.5)$$

where C_v is the rolling resistance coefficient, m is the vehicle mass in kg , g is the gravitational acceleration in $\frac{m}{s^2}$ and α represents the inclination of the plane and, obviously, it depends on the track, but in most cases, in the design stage, is kept equal to zero.

The only parameter that deserves a further definition is \mathbf{C}_v . The quantity is always obtained empirically by means of road tests. It is possible to give an experimental definition of the above mentioned parameter:

$$C_v = f_0 + f_2 v^2 \quad (3.6)$$

where f_0 represents a constant road load, whereas f_2 a second order load. A typical test plans to drag the vehicle on which the two parameters wanted to be calculated, with another car. After that, the coasting down phase follows, leaving the vehicle decreasing its speed. This gives the opportunity to calculate the f_0 and f_2 . So, they depends on the type of vehicle, of surface on which the tyres are rolling as well as the temperature of it. The pressure of the tyres has to be considered as well in the calculus. Typical values for cars of f_0 are 0.045-0.16; in case of ground and for the homogeneous asphalt, the quantity goes down to 0.013.

3.3.2 WLTP working points

At this stage, knowing what are the forces that influence the dynamic of the vehicle, it has been possible to have a broad idea of what should be the point of interest in which focus the attention for the design process.

As it can be noticed from the previous paragraph, some choices must already be taken, in order to obtain an initial and easy model of the vehicle for whom the electric motor will be design.

In the table 3.3 are shown the parameters that have used to estimate the forces applied to vehicles dynamics.

Vehicle information		
Total weight (kg)	1368	kg
Wheel radius	0.2159	m
Frontal area (A_f)	1.746	m_2
Aer. drag coeff.	0.3	
Rolling coeff.	0.009	[48]
Air density	1.225	$\frac{kg}{m_3}$

Table 3.3: Vehicle features

For the the car parameters, the vehicle chosen as reference has been the Toyota Prius model. In particular, A_f has been retrieved using the height and the width of the motor. The wheels radius has been found looking at the tyre code of the most used ones for the Prius. The aerodynamic drag coefficient and the rolling coefficient are the most common for road vehicles. Finally, the air density has been calculated considering a temperature of $20 \text{ }^\circ C$ and 1 atm of pressure.

At this point, the goal has been to retrieve the working points imposed by the WLTP on the $T - \omega$ graph. The driving cycle gives us already the time steps and also the speed that must be reached. So, the acceleration can be easily found. Thus, considering the equation 3.1, once that the resistive forces are calculated, the tractive force can be straightforwardly obtained adding to them the product of the acceleration and the mass of the vehicle. However, the performance requested by the driving cycle refer to the wheel side. It follows that, in order to understand where the motor will work in the $T - \omega$ graph, it is necessary to shift the attention to the motor side. To do that, a proper gear ratio must be decided. As already mentioned, the electric vehicles usually adopts a fixed gear ratio. In the thesis, the value adopted is 4; the choice comes from the solution already available on the market, like the Prius that adopts a 1:4.11 gear ratio. Of course, having an higher value of gear ratio would imply an higher value of rotational speed and a lower torque at motor side than the wheels one. However, defining the gear ratio is not enough: in order to obtain the desired torque and speed, an efficiency profile of the traction line must be pointed out. It is about to broadly fix the efficiency for each component of the power train. The choices are summarized in the following table (3.4).

Efficiency	
Wheels	1
Gear	0.98
Motor	0.98
Converter	0.99
Battery	0.90
Overall	0.93

Table 3.4: Efficiency of the traction line

All values are quite typical for every electric vehicle; it has been decided to consider the wheels ideal.

The reason why the efficiencies need to be fix is that during a acceleration phase, the torque transmitted to the wheels through shaft from the motor suffers from the non ideality of the transmission. Consequently, to retrieve the torque at motor side, the one at wheel side must be divided for the efficiency of the transmission at vice versa. Finally, in figure 3.5 the working points from WLTP for the vehicle are shown.

The points retrieved will be further analyzed during the control and optimisation stages. The main idea is to focus the attention on these peculiar working points because it is more likely that the motor will end up working there. As a consequence,

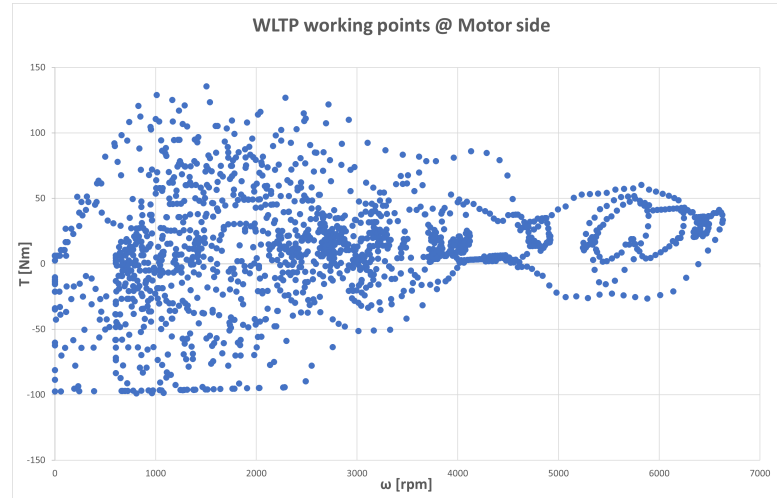


Figure 3.2: WLTP working points for the vehicle considered.

thanks to the control it will be possible to have a proper exploitation of electrical quantities and the optimisation will be carried out only for that positions that are a good representation of the vehicle actual behavior.

At this stage, it has been convenient to find an ideal $T - \omega$ graph, that can be used as a reference of the performance wanted for the electric machine under design. Thus, as first consideration, the aforementioned characteristic needs to overcome the WLTP working points in order to be sure that the motor is capable of respect the goals. One way to that is to impose a certain initial acceleration at wheels. In this case, it has been considered an acceleration of $2.84 \frac{m}{s^2}$ equal to an acceleration time ($0 - 100 \frac{km}{h}$) equal to $9.82s$. Remembering the equation 3.1, it has been possible to calculate the tractive force that should be transmitted to the wheel by the motor. Then, the traction force can be easily found reversing it and the traction torque as well, as the following equation suggests:

$$T_{traction} = F_{traction}r \quad (3.7)$$

where r is the radius of the wheels.

Using the same reasoning of the working points, the tractive force at motor has been found. In order to fix the base speed, it has been considered a broad power value of $60kW$.

As it can be noticed, the initial acceleration decreases as long as the speed increases, because the tractive forces are proportional to the speed. This has been a choice made in order to easily find the specification of the motor in terms of

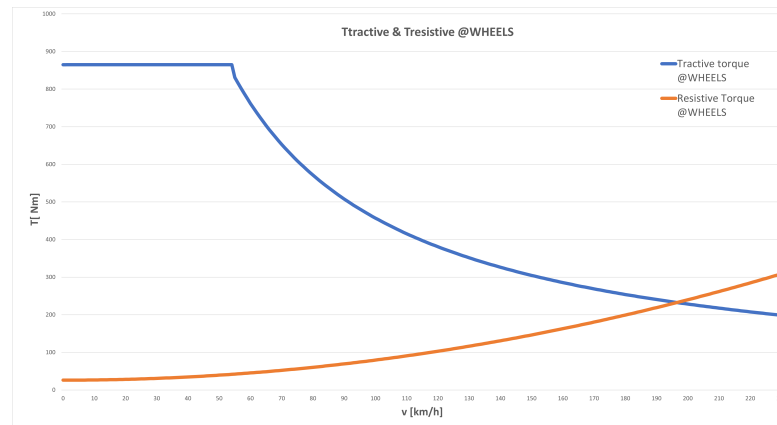


Figure 3.3: $T_{tractive}$ and $T_{resistive}$ at wheels side.

performance. It has been decided to maintain only at the beginning the fixed acceleration. Otherwise, the tractive torque would increase with the speed, until the base speed. Furthermore, the intersection points of the curves defines the maximum theoretical speed. Applying the proper fixed ratio, the WLTP points and the $T - \omega$ graph at motor side have been found.

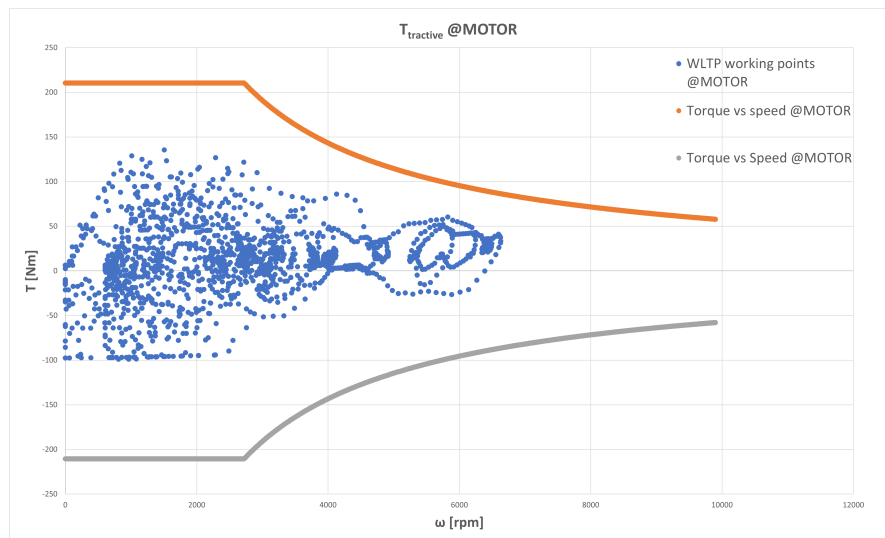


Figure 3.4: WLTP working points and $T - \omega$ graph at motor side.

Finally, the *power – speed* graph is found.

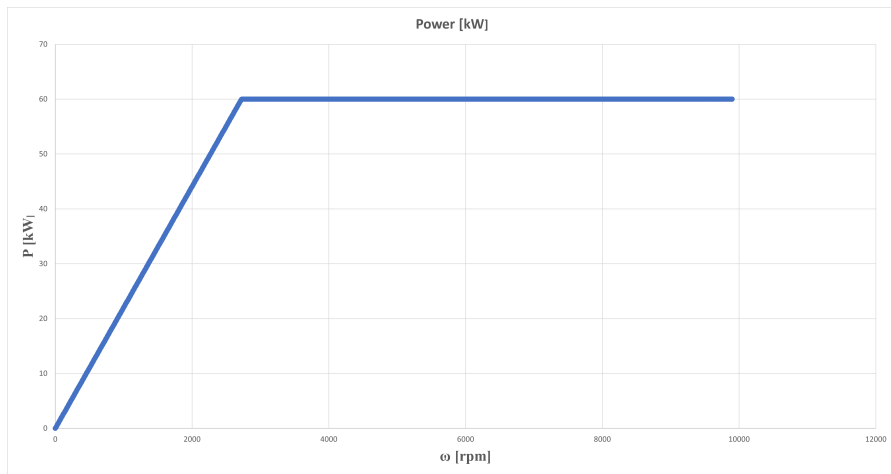


Figure 3.5: $P - \omega$ graph of the motor.

Chapter 4

Geometry description

In the following chapter the geometry adopted for the machine under design will be described. A particular focus will be reserved to the rotor which has been subjected to parameterization.

4.1 Overall view

Once defined the working points of the electric machine, the following step consists in defining a proper geometry through setting a number of parameters. It would be preferable to have as less parameters as possible; in fact, if the number is quite contained, it will follow an easy and fast optimization. Furthermore, as already said in the chapter 2, for these motors, the structure has a key role in defining their features. For these reasons, a careful study has been carried out in order to comply with the needs.

The discussion has been organized as follows:

- Stator description
- Rotor description

As far as the stator is concerned, the situation does not present great difficulties, since it is basically identical to the other three phase electrical machines. In this sense, its construction follows the traditional principles and does not have any innovation. On the other hand, what has been at the centre of the focus has been the rotor geometry, for several reasons that will be explained in paragraph 4.3.1.

Before going into the details of the two parts of the motor, it is better to introduce some main dimensions that affect all the structure.

As it can be noticed from figure 4.1, there are some fundamental quantities that need to be fixed:

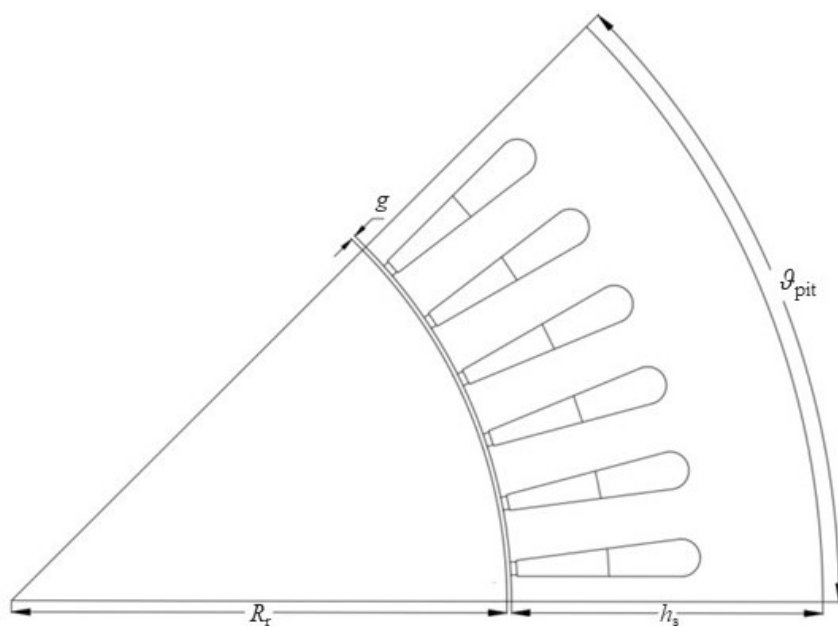


Figure 4.1: Main dimensions of the electric machine.

- the airgap g ;
- the rotor radius R_r ;
- the stator height h_s ;
- the polar pitch θ_{pit} .

The airgap g has a fundamental role in every machine. It is the air space between the rotor and the stator that allows the rotation of the rotor within the stator. A lot of proprieties are strictly correlated to it: to make an easy example, the lower it is, the better it is from an electromagnetic point of view. Having the stator and rotor closer would be beneficial for the torque production, since it has strong relationship with the flux at the airgap. It would be possible to increment its value because the the fluxes, produced by the rotor and the stator, could interact more. Thus, the linkage flux is highly affected by it and the flux density at the airgap will be higher. Furthermore, the efficiency and other parameters like the back EMF and the power factor are influenced by the geometrical value. On the other hand, having a small airgap would produce more cogging torque, since the interaction between the stator teeth and the rotor will be higher [49]. In any case, it would also produce mechanical problem, since there could be an interference between the stator and the rotor. It will lead to friction, to an increment of the internal temperature and possible damages. Optimal values of airgap should not

be lower than 0.7 mm and not bigger than 1.6 mm.

The rotor and stator radius, R_r and R_s , define the main structure of the motor. In order to find the stator radius the following expression can be adopted:

$$R_s = R_r + g + h_s \quad (4.1)$$

Together with the active length of machine L , they represent an important parameters to catheterize the power and torque production. It comes natural that having a bigger volume implies an higher power and torque. However, as already said, the first thing to consider during the design is to keep the ratio between power and volume as high as possible, so not to occupy too much space in the vehicle. In order to give a broad idea of what relationship exists between those dimensions, the equation 4.2 comes to help.

$$\frac{L}{R_s} = 1.2 \div 3 \quad (4.2)$$

Finally, the θ_{pit} represents the opening angle for every pole in the machine.

$$\theta_{pit} = \frac{2\pi}{p} \quad (4.3)$$

where p is the number of poles in the machine.

Having an high number of pole pairs would be good from the different points of view: the flux that passes through the airgap will be increased, the efficiency and the torque too. As suggested by [50], a proper number of pole pairs ranges between 3 and 6. If the number was lower than the range, it would have not been observed the flux concentration; in the opposite case, the flux in air gap could decrease.

4.2 Stator geometry

The stator structure of a three phase machine is shown in figure 4.2. As it can be seen, its shape is identical to that of AC machines, since the aim is same: to produce magnetic voltage and to link as much flux as possible coming from the rotor.

It is composed by two main elements:

- slots
- teeth

A value that must be set is the number of slots N_s . From it, the number of slots per pole q_f and per pole and phase q are obtained with the following expression:

$$q = \frac{N_s}{pm} \quad (4.4)$$

$$q_f = \frac{N_s}{p} \quad (4.5)$$

where p is the number of poles and m the number of phases.

It is more usual referring to q than N_s . In any case, defining the proper number of slots is not an easy task, since there is not a strict rule on how deciding it. What is usually done is firstly to decide q , looking at the already existing solutions for the particular application and retrieve from it the N_s , reversing the equation 4.4.

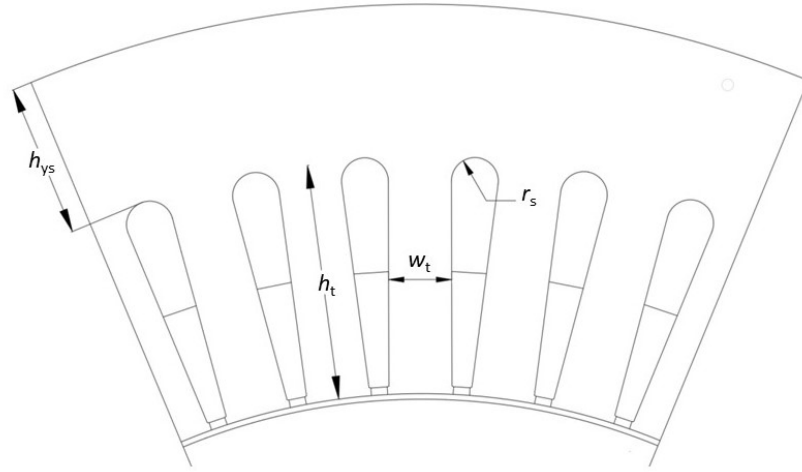


Figure 4.2: Structure of the stator.

Looking at the figure 4.2 and 4.3, it can be noticed that the main dimensions of the slot, once decided its shape, will be fixed if the dimensions of the tooth are given. If the slots present a trapezoidal shape, the width of the teeth w_t will be constant and consequently, the width of the slot will be obtained with the following equation:

$$\omega_{slot} = \frac{r\theta_{pit}}{N_s\omega_t} \quad (4.6)$$

where r is the generic radius depending at which height we want to calculate the slot width.

The figure 4.3 presents a detail of the slot; from it, the slot opening w_{so} can be observed. The parameter affects some properties of the machine. In particular, the

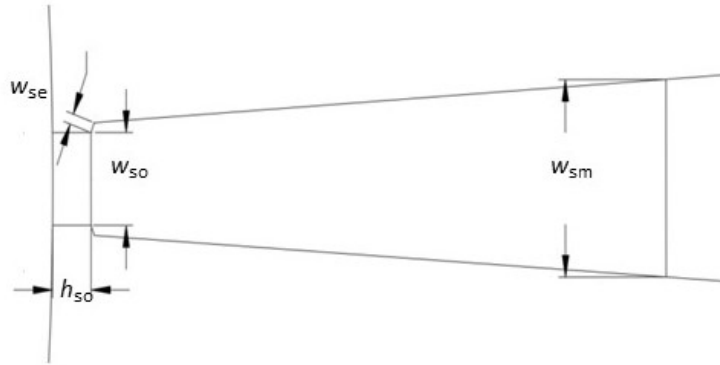


Figure 4.3: Detail of the stator slot.

main effect is the distortion of the magneto motive-force that presents holes due to the slots opening. The phenomenon is different for every harmonic and can be translated in a fictitious increment of the airgap, through the *Carter coefficient* \mathbf{k}_c . In particular, the coefficient increases when the slot opening is higher, causing a more distorted magneto-motive force. As far as the slot tooth is concerned, it is described by the height h_{so} and the tangential depth w_{se} . There are not optimal values for them, but they usually come out from the experience. The w_{sm} is the width in the middle of the height of the slot.

From the teeth point of view, the description is straightforward: the width w_t is constant due to the shape of the slots. It is an input parameter and it has a fundamental role in the flux density of the tooth itself. Having narrower teeth implies the flux coming from the airgap is more concentrated and, thus, the flux density will be higher. If the values are too high, a non-negligible part of the magnetic flux will flow in the slot and, as a consequence, the magnetic voltage drop of the tooth will be lower.

The only remaining parameter to be still defined is the height h_t , linked to the stator yoke height h_{ys} as well by the following relationship:

$$h_s = h_t + h_{ys} \quad (4.7)$$

The h_{ys} must be decided so that the flux density ranges between $1.2 \div 1.4$ T, in order to limit the magnetizing current and the iron losses.

SyR-e code

In order to easily draw the stator geometry, the open source code **SyR-e** has been adopted. It has been born from the collaboration of two Italian universities,

the Polytechnic of Turin and the Polytechnic of Bari. It can be used for the design of the most common machines like the SPMs, the interior v-type motors but also for synchronous reluctance machines. The idea behind the code is to firstly draw a parametrized geometry and ,then, save it as a *.fem* file. Through the FEMM 4.2 software, fast analysis are carried out and the results are sent back to the Matlab environment in order to obtain the performance. The code presents different functionalities like the possibility to design the dimensions of the machine, the windings, to set a proper rotor structure depending on which of the above mentioned machines are considered. It is also possible to build a thermal model of the motor and to set the mechanical constraint. Then, the motor can be also subjected to optimization. Looking at the results it is possible to obtain, it gives access to the flux maps and to all the parameters that affect the behaviour of the motor. The efficiency map can be obtained from the manipulation of the magnetic model [51].

For the case of interest, the GUI (graphic user interface) of Syr-e has been used to obtain a quick draw of the stator.

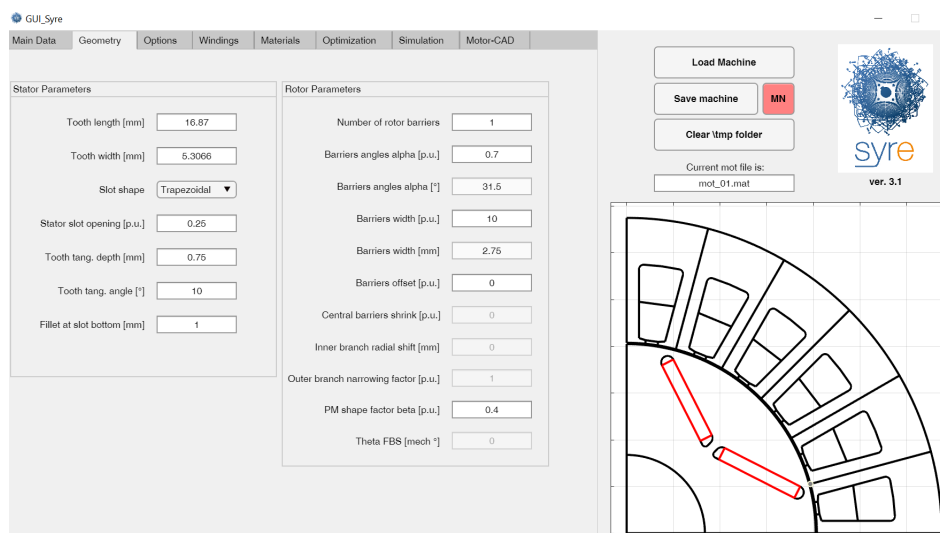


Figure 4.4: Syr-e GUI.

As it can be possible to notice from figure 4.4, the above mentioned parameters that have an influence on the stator are the inputs of the GUI. It would have been possible to adopt the code also for the rotor geometry. The reason why it has not been done is that it has been tried to describe the rotor in a manner that will be beneficial from the optimisation point of view.

4.3 Rotor geometry

As it is known, for this type of machine, the magnets are positioned inside the rotor and most of the properties are strictly related to it. For this reason, it is fundamental having a good description of it and a proper space management.

In the work, a custom geometry has been applied for the rotor. The main concept behind it is to decide a small amount of parameters and only through them being capable of get all the dimensions. In other words, once fixed the main parameters, all the quantities can be easily obtained. This way to proceed has been thought in order to make the optimisation process as fast as possible. If the number of parameters is not too wide, the optimization algorithm will be faster because the number of cases to be explored will be lower.

Before taking into consideration the particular shape of the magnet barrier, the first task has been to define the space available in which allocate the magnets. The figure 4.5 shows the criteria adopted for the rotor geometry and the main dimensions.

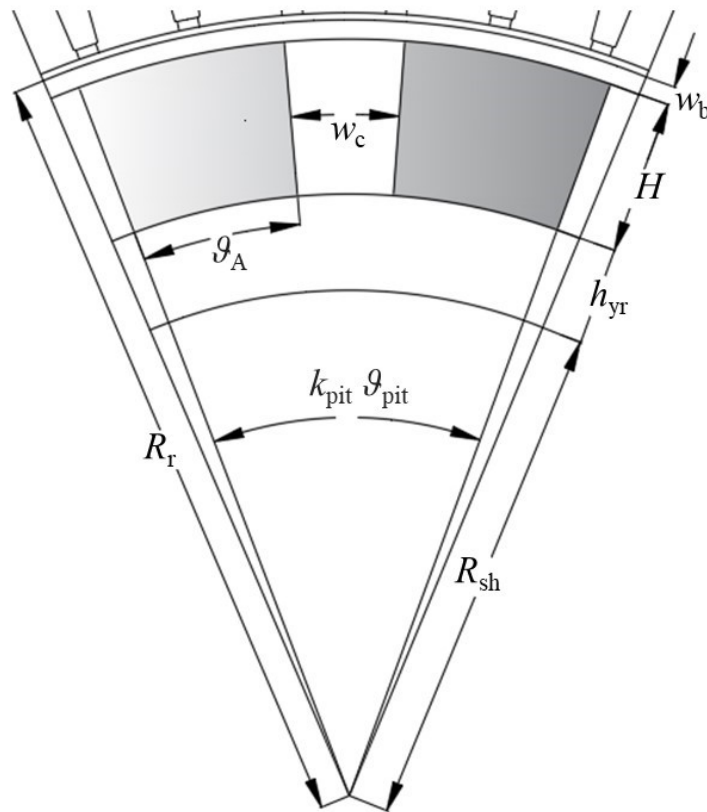


Figure 4.5: Rotor main dimensions.

The grey areas are the ones dedicated to house the magnets. In order to obtain them, the following inputs parameters have been employed:

- the rotor radius \mathbf{R}_r ,
- the rotor shaft radius \mathbf{R}_{sh} ,
- the coefficient \mathbf{K}_c ,
- the coefficient \mathbf{K}_{pit} ,
- the bridges width \mathbf{w}_b ,
- the rotor yoke height \mathbf{h}_{yr} ,

First of all, it must be chosen a proper value for the rotor radius \mathbf{R}_r . Every dimension will be affected by it, in particular the rotor shaft radius \mathbf{R}_{sh} that has the closest relationship. They are linked by an input parameter called \mathbf{r}_o , through the following equation:

$$R_{sh} = r_o R_r \quad (4.8)$$

The rotor shaft is responsible for transmitting the torque; thus, a proper value of r_o must be chosen. In order to that, it is useful to take into consideration that the shaft will be subjected to vibration. So, it is necessary opt for a material that can handle the forces applied to it [52]. Feasible values of r_o could be $0.4 \div 0.6$.

Proceeding along the radial direction, other two parameters needed to be fixed: the width bridge \mathbf{w}_b and the rotor yoke height \mathbf{h}_{yr} . Considering the first one, as already said in the paragraph 2.3.1, it plays a crucial role for the flux path. While operating below the base speed, the bridges are completely saturated, pushing the flux produced by the magnets in the direction of the airgap. On the other hand, during the flux weakening region, they constitute a passage for the flux along the d-axis. It follows that, the narrower are the more saturated they will be. Furthermore, it is not possible having too small bridges, because the mechanical stress, due to the rotation, will be too high, putting in danger the whole structure. Thus, defining in this way the geometry allows an optimal control of the every quantity.

The rotor yoke is the iron space between the rotor shaft and the magnets area. Through it, the magnetic flux flows, closing its path. As far as the design is concerned, this is a parameter that highly influence the width of the magnets.

Now that, every radial element have been defined, it could be possible that not all the polar pitch θ_{pit} is used to locate the magnets but only a part of it. In this

sense, the parameter \mathbf{k}_{pit} has been defined, indicating the portion of the polar angle that is considered. θ_{mag} is the real angle considered.

$$\theta_{mag} = k_{pit}\theta_{pit} \quad (4.9)$$

Typical values of it range between $0.7 \div 0.95$; an higher value could allow to have more magnets, but on the other hand, it will make the passage for the flux along the q-axis narrower, provoking saturation.

Finally, the last parameter to be taken into account is the space between the magnets. The reasoning is the same as the one adopted for the θ_{mag} : the coefficient k_c is introduced to set the angle that corresponds to that distance.

$$\theta_c = k_c\theta_{pit} \quad (4.10)$$

It follows the distance will be slightly different according the height at which it is considered. This dimension has a role similar to that of the bridges. It will be highly saturated when working below the base speed, in order to force the magnetic flux path along the d -axis; it is also a path for the flux leakage that will not reach the airgap, making the torque decrease. On the contrary, when there is a negative i_d component, pushing the flux along the negative d -axis, the space constitute a way for the flux. It is very important from the permanent magnets point of view: thanks to it, the destruction of the PMs is avoided because there would be an alternative way to let the flux flows, not acting against them.

In conclusion, the two symmetric magnets area can be defined introducing the height \mathbf{H} and the opening angle θ_A as follow:

$$H = (1 - r_o)R_r - w_b - h_{yr} \quad (4.11)$$

$$\theta_A = \frac{\theta_{pit}}{2}(k_{pit} - k_c) \quad (4.12)$$

4.3.1 Magnets design

Once defined the area in which allocate the magnets, their dimensions have been obtained applying some basic geometrical principles. First all, it useful to remember that, in the thesis, the V-type shape has been investigated; consequently, every pole of the machine presents two magnets, inclined with a fix angle, along the d -axis, in order to reproduce that particular shape. Since it has been said that having a multiple barriers structure permits to exploit better the features of the machine, a three barriers geometry has been investigated. This choice increments the saliency

of the machine, letting us obtain an higher torque. Besides it, using more barrier increases the amount of flux coming from the PMs, and, thus, a lower value of current is needed to reach a determined value. On the contrary, it also implies an higher cost due to the rare earth materials. Furthermore, it could negatively affect the characteristic current that could become higher than the nominal one, not permitting to fully explore the flux wakening region.

In order to obtain the dimensions of the magnets, the function *Magnetdesign.m* has been defined in Matlab. In addition to the parameters cited in paragraph 4.3.1, the other inputs needed are:

- the magnets angle of inclination θ_{PM} ,
- the height of the magnets h_{PM} ,
- the coefficient k .

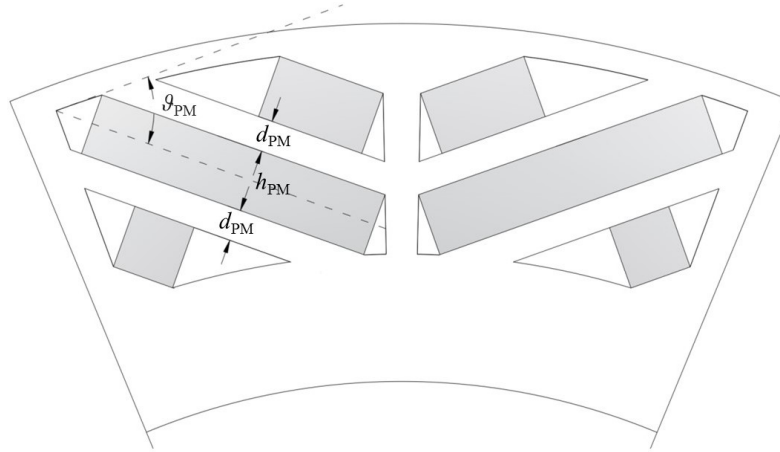


Figure 4.6: Magnet barriers in the rotor.

As it is shown in figure 4.6, all the barriers present the same angle of inclination θ_{PM} . Its measure is taken from the tangent to the upper side of the area and it can range from 30° to $60^\circ - 70^\circ$, according to the case of study. The height h_{PM} and the coefficient k are strictly related because they hugely affect the width of the magnets. In particular, the distance between them is given by the following relationship:

$$d_{PM} = kh_{PM} \quad (4.13)$$

Classical values of it are $0.5 \div 2$.

The main idea behind the whole proceeding is to obtain the width through the diagonal of every barrier. In fact, they are composed by the magnet itself and two air barriers. The latter, mainly have a triangular form, that could slightly change according to θ_{PM} . Once obtained the diagonal, the lengths h_1 and h_2 , related to the air barriers, will be subtracted to it, obtaining the width of the magnets, as shown in figure 4.7.

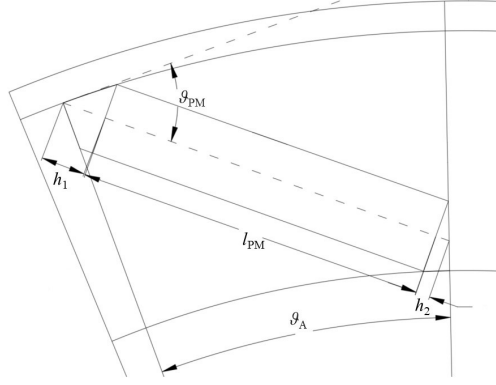


Figure 4.7: Particular of the central magnet barrier.

$$l_{PM} = d_g - h_1 - h_2 \quad (4.14)$$

The way in which the three sizes are calculated depend on which barrier and θ_{PM} is considered.

Central barrier

As already said, the way to find the three dimensions could change according to the angle. Referring to figure 4.7, it can be possible to say that the diagonal could either get in touch with the right side of the area or with the lower one; d_{gc} and h_2 are affected by it.

Applying the sine theorem, the angle limit θ_{PMLIM} used to distinguish the two cases, and also the maximum amplitude of the diagonal can be obtained as follow:

$$d_{glimc} = \sqrt{(R_r - w_b)^2 + (h_{yr} + r_o R_r)^2 - 2(R_r - w_b)(h_{yr} + r_o R_r)\cos(\theta_A)} \quad (4.15)$$

$$\theta_{PMlimc} = \frac{\pi}{2} - \arcsin\left(\frac{(h_{yr} + r_o R_r)\sin(\theta_A)}{d_{glimc}}\right) \quad (4.16)$$

Starting from the d_{gc} , when $\theta_{PM} < \theta_{PM_{limc}}$, we have:

$$d_{gc} = (R_r - w_b) \frac{\sin(\theta_A)}{\sin(\frac{\pi}{2} + \theta_{PM} - \theta_A)} \quad (4.17)$$

$$h_{2c} = \frac{h_{PM}}{2} \frac{1}{\tan(\frac{\pi}{2} + \theta_A - \theta_{PM})} \quad (4.18)$$

Otherwise:

$$x = \arcsin\left(\frac{(R_r - w_b)\sin(\frac{\pi}{2} - \theta_{PM})}{r_o R_r + h_{yr}}\right) \quad (4.19)$$

$$d_{gc} = (R_r - w_b) \frac{\sin(\frac{\pi}{2} + \theta_{PM} - x)}{\sin(x)} \quad (4.20)$$

$$h_{2c} = \frac{h_{PM}}{2} \frac{1}{\tan(x - \frac{\pi}{2})} \quad (4.21)$$

Furthermore, for h_1 , two cases must be considered: when $\theta_{PM} < 45^\circ$ or $\theta_{PM} > 45^\circ$. In the first case, h_{1c} is equal to:

$$h_{1c} = \frac{h_{PM}}{2} \frac{1}{\tan(\theta_{PM})} \quad (4.22)$$

Otherwise:

$$h_{1c} = \frac{h_{PM}}{2} \frac{1}{\tan(\frac{\pi}{2} - \theta_{PM})} \quad (4.23)$$

In conclusion, depending on the inclination and the size of the magnets area, we obtain the width of magnet related to the central barrier:

$$l_{PMc} = d_{gc} - h_{1c} - h_{2c} \quad (4.24)$$

As already said above, the shape of the air barriers is mainly triangular, but it could vary according the inclination of the barrier.

Upper barrier

For the upper barrier, the reasoning is similar to that of central barrier. The only difference is the introduction of the angle θ which is the angle between the contact points of the diagonals d_{gc} and d_{gu} with the upper side of the magnets area.

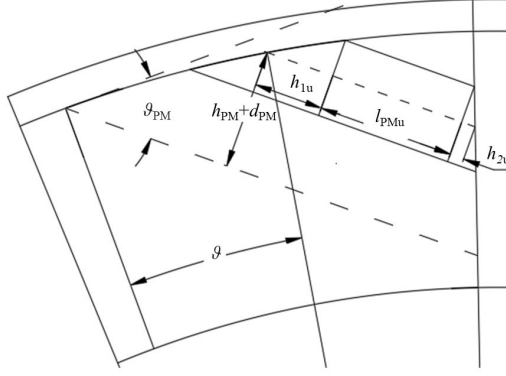


Figure 4.8: Detail of the upper barrier.

It is influenced by the distance d_{PM} and it will responsible for a wider or narrower upper barrier, according to the remaining space available.

Looking at the figure 4.8, θ can be found as follow:

$$\theta = \frac{\pi}{2} + \theta_{PM} - \arcsin\left(\sin\left(\frac{\pi}{2} - \theta_{PM}\right) + \frac{(d_{PM} + h_{PM})}{R_r - w_b}\right) \quad (4.25)$$

Now, it is possible to find the $d_{g_{limu}}$ and the $\theta_{PM_{limu}}$ for the upper barrier:

$$d_{g_{limu}} = \sqrt{(R_r - w_b)^2 + (h_{yr} + r_o R_r)^2 - 2(R_r - w_b)(h_{yr} + r_o R_r)\cos(\theta_A - \theta)} \quad (4.26)$$

$$\theta_{PM_{limu}} = \frac{\pi}{2} - \arcsin\left(\frac{(h_{yr} + r_o R_r)\sin(\theta_A - \theta_{PM})}{d_{g_{limu}}}\right) \quad (4.27)$$

Following the same procedure of the central barrier, for $(\theta_{PM} - \theta) < \theta_{PM_{limu}}$, we have:

$$d_{gu} = (R_r - w_b) \frac{\sin(\theta_A - \theta)}{\sin\left(\frac{\pi}{2} + \theta_{PM} - \theta_A\right)} \quad (4.28)$$

$$h_{2u} = \frac{h_{PM}}{2} \tan(\theta_{PM} - \theta_A) \quad (4.29)$$

In the case in which, $(\theta_{PM} - \theta) > \theta_{PM_{limu}}$

$$x = \frac{\pi}{2} - \arcsin\left(\frac{(R_r - w_b)\sin(\frac{\pi}{2} - \theta_{PM} + \theta)}{r_o R_r + h_{yr}}\right) \quad (4.30)$$

$$d_{gu} = (r_o R_r + h_{yr}) \frac{\sin(\frac{\pi}{2} + \theta_{PM} - \theta - x)}{\sin(\frac{\pi}{2} + \theta - \theta_{PM})} \quad (4.31)$$

$$h_{2u} = \frac{h_{PM}}{2} \frac{1}{\tan(x - \frac{\pi}{2})} \quad (4.32)$$

For h_1 , there is only one equation equal to:

$$h_{1u} = \frac{h_{PM}}{2} \frac{1}{\tan(\theta_{PM} - \theta)} \quad (4.33)$$

It follows that, the width of the upper magnet is the following:

$$l_{PMu} = d_{gu} - h_{1u} - h_{2u} \quad (4.34)$$

Lower barrier

The $d_{gl_{iml}}$ and $\theta_{PM_{liml}}$ can be found as follow:

$$d = (R_r - w_b) - \frac{(d_{PM} + h_{PM})}{\sin(\frac{\pi}{2} - \theta_{PM})} \quad (4.35)$$

$$d_{gl_{iml}} = \sqrt{d^2 + (h_{yr} + r_o R_r)^2 - 2d(h_{yr} + r_o R_r)\cos(\theta_A)} \quad (4.36)$$

$$\theta_{PM_{liml}} = \frac{\pi}{2} - \arcsin\left(\frac{(h_{yr} + r_o R_r)\sin(\theta_A)}{d_{gl_{iml}}}\right) \quad (4.37)$$

For $\theta_{PM} < \theta_{PM_{liml}}$, we have:

$$d_{gl} = (R_r - w_b) - \frac{(d_{PM} + h_{PM})}{\sin(\frac{\pi}{2} - \theta_{PM})} \frac{\sin(\theta_A)}{\sin(\frac{\pi}{2} + \theta_{PM} - \theta_A)} \quad (4.38)$$

$$h_{2l} = \frac{h_{PM}}{2} \frac{1}{\tan(\frac{\pi}{2} + \theta_A - \theta_{PM})} \quad (4.39)$$

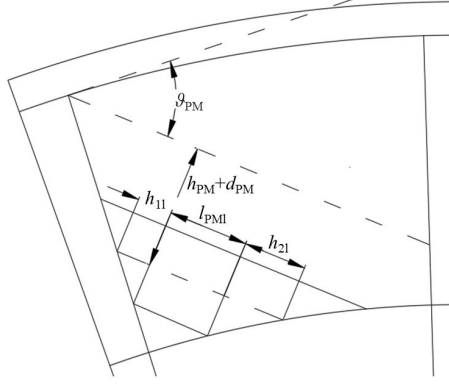


Figure 4.9: Detail of the lower barrier.

On the contrary, we obtain:

$$x = \arcsin\left(\frac{(R_r - w_b - \frac{(d_{PM} + h_{PM})}{\sin(\frac{\pi}{2} - \theta_{PM})})\sin(\frac{\pi}{2} - \theta_{PM})}{r_o R_r + h_{yr}}\right) \quad (4.40)$$

$$d_{gl} = (R_r - w_b - \frac{(d_{PM} + h_{PM})}{\sin(\frac{\pi}{2} - \theta_{PM})}) \frac{\sin(\frac{\pi}{2} + \theta_{PM} - x)}{\sin(x)} \quad (4.41)$$

$$h_{2l} = \frac{h_{PM}}{2} \frac{1}{\tan(\frac{\pi}{2} - x)} \quad (4.42)$$

Finally, the l_{PMI} can be found, as usual, from:

$$l_{PMI} = d_{gl} - h_{1l} - h_{2l} \quad (4.43)$$

Bridges along the d-axis

Besides, the dimensions of the magnets, other important measures that must be calculated are the ones referred to bridges, because in those points, the saturation of the iron happens and it is strictly connected to their sizes. Looking at the figure 4.10, the quantities of interest can be calculated as follow:

$$W_C = 2(h_{yr} + R_r + l_c) \sin\left(\frac{k_c \theta_{pit}}{2}\right) \quad (4.44)$$

$$w_c = 2(h_{yr} + R_r) \sin\left(\frac{k_c \theta_{pit}}{2}\right) \quad (4.45)$$

$$l_c = H - l_{PMu} \cos\left(\frac{\pi}{2} + \theta_A - \theta_{PM}\right) \quad (4.46)$$

$$w_{bc} = \frac{h_{PM}}{2 \sin(\theta_{PM})} \quad (4.47)$$

$$w_{bu} = \frac{h_{PM}}{\cos\left(\frac{\pi}{2} - \theta_{PM} + \theta\right)} \quad (4.48)$$

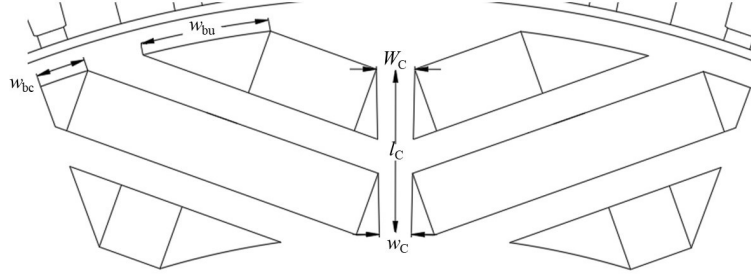


Figure 4.10: Dimensions of the bridges.

Dimensions along q-axis

All the dimensions presented till now have been referring to quantities along the d -axis. It is better investigate the q -axis too, in order to retrieve some important information that will be used in the design method. As known, for this machine, the q -axis is located along the direction of maximum permeance. All the sizes needed are depicted in figure 4.11. Starting from l_{qt} , l_q , W_t and w_q :

$$l_q = l_{PMl} \cos\left(\frac{\pi}{2} - \theta_{PM}\right) \quad (4.49)$$

$$l_{qt} = (H - l_q + (h_{yr} + r_o R_r)) - \sqrt{(h_{yr} + r_o R_r)^2 - \frac{W_Q^2}{4}} \quad (4.50)$$

$$W_t = 2(H + h_{yr} + r_o R_r) \sin\left(\frac{(1 - k_{pit} \theta_{pit})}{2}\right) \quad (4.51)$$

$$w_q = 2(l_q + h_{yr} + r_o R_r) \sin\left(\frac{(1 - k_{pit} \theta_{pit})}{2}\right) \quad (4.52)$$

W_Q can be obtained as follow:

$$\alpha = (1 - k_{pit})\theta_{pit} + 2 \arcsin\left(\frac{l_{PMc}}{(h_{yr} + r_o R_r)} \sin(\theta_{PM} - \frac{\pi}{2})\right) \quad (4.53)$$

$$W_Q = 2(h_{yr} + r_o R_r) \sin\left(\frac{\alpha}{2}\right) \quad (4.54)$$

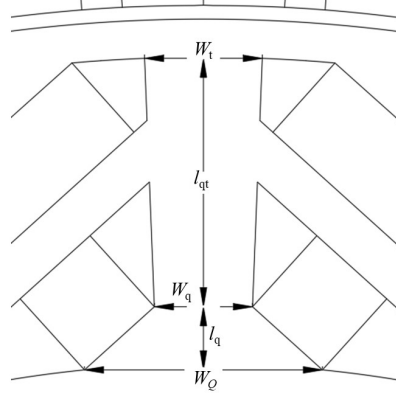


Figure 4.11: Dimensions along the q-axis.

Chapter 5

Design method

In this chapter, the design method chosen for the machine, the reluctance network approach, has been described. Its base principles, the benefits and the drawbacks have been explained together with magnetic equivalent circuits adopted for the motor of interest. Finally, the validation procedure and the results have been shown, starting from two initial designs of the machine.

5.1 Choice of the design method

Nowadays, most of the designs of the electrical machines are carried out with software that rely on the finite element methods. It consists in a numerical technique that helps to approximate the solutions of different problems, described by partial differential equations. Then, those are reduced to a system of algebraic equations. The main idea behind is to decompose the area that must be investigated, for example the entire surface of a motor, in small elements, called finite elements with the intent to discretize the entire region of interest [53]. In this way, a *mesh* of these *finite elements* is created. Furthermore, the latter have fixed forms, for example, triangular, quadrilaterals and even more complex ones for a 3D representation. It should be noted that sometimes the function is approximated, and consequently, the exact values of it will not necessarily be the ones calculated in the points, but those which provide the least error on the whole solution.

It follows that the selling points of the finite elements method are the following:

- reaching accurate solutions;
- adaptability to several geometries;
- capability of dealing with any kind of boundary conditions.
- capability of dealing with anisotropic and non-homogeneous elements.

On the other hand, there are always side effects to be considered: it is true that this approach will lead to accurate results, but in most of the cases, it would be necessary to refine the mesh; it follows that the number of finite elements would increase. In the FEM software, this corresponds to a request of bigger number of operations that must be handle by the CPU. As a consequence, the **computational time will be higher**. The same problem comes for particular geometries in which dense meshes are needed. Thus, it is possible to say that the biggest problem faced during the implementation of the FEM is the **time** for every simulation. In addition, there could be calculation errors inherent to the limited number of significant digits a computer can handle and, consequently, to the decimal truncation of the numerical quantities. It follows a difficulty for the computer to operate with extremely large and extremely small numbers.

Considering what has been said above, for the thesis, it has been decided to follow a method that leads to create a **tool** which makes possible to design the V-type IPM machine, without employing a great computational effort. In other words, we have been looking for a method that permits to obtain results as **fast** as possible and capable of representing the electromagnetic behaviour of the motor in a faithful way. The reason why we have been looking for something that has these features is the following: as input of the design process, we have received the working points coming from the WLTP driving cycle, from which a limit torque-speed characteristic of the motor has been drawn. In order to have the motor that is compliant with this curve, we have needed to implement a control in order to properly optimize the machine in those characteristic points and also trace the efficiency map.

As it can be noticed, if we had used the FEM approach to follow the path, it would have taken a lot of time, because the computational time would have been considerable high, especially in the optimization part, in which several machines are tested in order to find the one that maximize the objective function. Therefore, it has been thought to implement a method that, although not capable of reaching the accuracy of the FEM software:

- it is very fast;
- it leads to a model of the electrical machine that can be easily controlled;
- it leads to a straightforward optimization process.
- it represents quite well the electromagnetic behaviour of the motor.

Taking into consideration what said until now, the method chosen for the design of the machine is the **reluctance network** one (RN), something expressed as magnetic circuits model (MEC).

5.1.1 Reluctance network principles

It is one of the oldest methods to model and to analyse electrical machines. It consists in creating a representation of the motor, through an *equivalent magnetic circuit*. The aim is to simulate the magnetic flux behaviour, with a lumped-parameter circuit, similarly to what is done for an electric circuit. It follows that the advantage of the fast computation of the results comes from this equivalency, since it is even possible to solve analytically the circuit and retrieve the value of the flux in different parts of the machine. There are two main parameters that constitute the reluctance network:

- the reluctance R that measures the opposition of a material to the transit of a magnetic flux, equivalent to a resistance in an electric circuit.
- a source of magneto motive force Mmf or a source of magnetic flux Φ , respectively equivalent to a voltage source or a current source in an electric circuit.

The equations that link these quantities are based on the magnetic Ohm's law, also called Hopkinson's law:

$$mmf_i = Ni = R_i\Phi_i \quad (5.1)$$

and on the Kirchhoff 's laws, for nodes and for loops:

$$\sum_i \Phi_i = 0 \quad (5.2)$$

$$\sum_i mmf_i = 0 \quad (5.3)$$

The main idea behind the reluctance network is to build the magnetic circuit, trying to better predict the path of the flux inside the machine, making some initial assumptions. A first difference with the FEM method is now observed: in the approach an higher degree of knowledge of the magnetic behaviour of the machine is required.

For example, we can expect that flux will be unidirectional in some parts of the machine, making the modelling process easier. Furthermore, if a discontinuity in the material is noted, another reluctance must be inserted in the circuit; the same reasoning is applied in case of a change in the dimensions.

It follows that the easier is the circuit, the faster will be its resolution even though the accuracy could be negatively affected. In order to have results more similar to those coming from the finite elements analysis, the number of reluctances of the circuit must increase.

Reluctance network in literature

In the literature there are several works that propose a reluctance network for the V-type interior permanent magnets motor. They range from very simple magnetic circuits to more complex ones. First of all, looking at the structure of an IPM motor, we should aspect a model in which we have two sources of flux: the PMs and the stator. The former can be represented either as a magnetic voltage source or as a flux one, in case in which the Thevenin equivalent or the Norton one is applied. On the other hand, the stator is a source of magneto motive force. The other parts of the machine, like the iron core and the air-gap are represented by reluctances; they have some peculiarity that will be later discussed.

In [54], the authors propose a straightforward model of the motor. They have considered a Thevenin equivalent for both magnets. There is a reluctance that represents the airgap and the other three the bridges. As already said, the bridges are the parts subjected to saturation; the assumption done here is to consider a fixed value of 2 T for those parts.

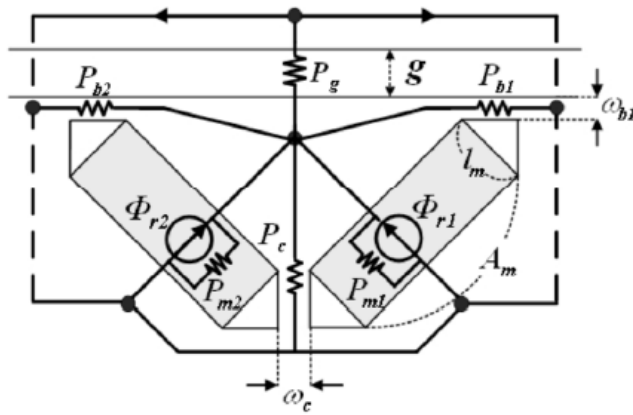


Figure 5.1: MEC model a V-type IPM motor from [54].

As the figure 5.1 suggests, it has been thought a central node to which the fluxes produced by the magnets, converge. In the model the presence of the stator is neglected.

On the other hand, it is also possible to obtain more complex networks adding more reluctances in order to better follow the flux and material behaviour. In this sense, it could be feasible introducing a discretization of the surface, representing it through elementary units in a nodal configuration. The work presented in [55] seems to follow the idea: as the figure 5.2 shows, it has been created a dense mesh of the stator and the rotor. The approach seems similar to the one adopted in the finite elements method.

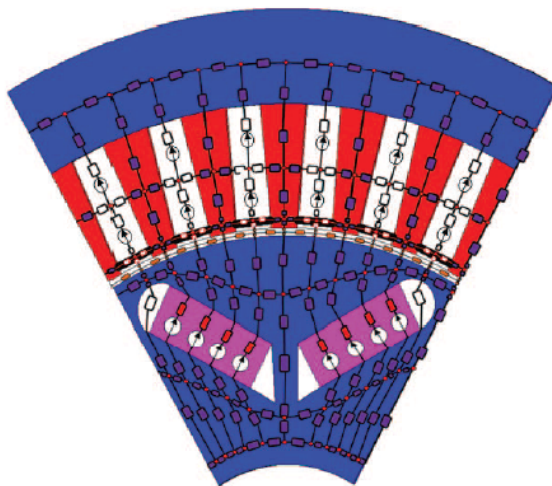


Figure 5.2: Mesh of the motor [55].

This model gives accurate results, but it comes into conflict with the initial idea of obtaining a tool that could be easy to use and especially fast. This is the reason why, what has been fought for the thesis is something in the middle of the two above mentioned models.

5.2 Reluctance network proposed for the machine

In this work, for the reasons already discussed, it has been fought to approach the problem, building two reluctance networks, one for d -axis and another one for q -axis. Since the aim is to follow the working points given by the WLTP, as inputs we have had a torque and a speed reference. It follows that the primary goal has been to calculate the torque from through the RN. In other words, from the tool the values of the flux along the d -axis and from q -axis must be observed.

As a consequence, the advantages of pursuing this path seem clear:

- Obtaining easily the electromagnetic torque;
- Control the machine, in order to follow the driving cycle points, given as references.

Looking at the torque production, it is correct to say that the results will have higher accuracy if an higher number of reluctances is employed, especially to take into consideration the behaviour of some peculiar parts of the machine, like the bridges. Another advantage will be the possibility to have a fast check of how the torque is influenced by the variation of some fundamental parameters, like the air-gap or the different shape or number of the magnetic barriers.

From a control point of view, this scheme could be of easy use because it would be possible to operate directly on the d and q components of the stator current, so directly on the magneto motive force along the axes. In addition, thinking about different control algorithms, like the FOC and DVFC, they can be implemented as well. The feature could gain interest in some contest, like in the flux weakening area, in which it would be possible to directly observe the demagnetizing action the negative i_d , along the axis where the magnets are located.

The two schemes have been obtained observing the magnetic flux path of an already existing V-type motor. In particular, the attention has been focused on a pole of the motor, in a no load condition, because in that configuration, the magnetic flux is practically aligned with the d-axis for these kind of machines, because it is only produced by the permanent magnets. Thinking about the geometry, depicted in figure 4.6, we know that every pole is formed by three barriers and every of that is composed by two magnets. It has been noted that, once overcome the air-gap, the flux splits itself in two equal part and re-closes itself on the other magnetic pole. Looking more closely, we have noticed that the flux produced by half north pole concludes its path passing through the closer half south pole. So, the magnetic circuits will represent this path: in particular, due to the symmetry that governs the motor, it has been possible to represent only one pole and then readjust the results, considering the number of pole pairs.

Once obtained the reluctance network, it has to be validated with another method that can be considered a good reference. This is the reason why, after having built the two magnetic circuits, the values of the electromagnetic torque have been compared to that of finite elements software, called FEMM 4.2. Considered what above said about the accuracy of the method and its computational time, obtaining an error below the 20 % can be considered acceptable.

Cross coupling effect

On the other hand, there is a problem that has appeared since the first steps of the approach: how to obtain the **the cross coupling effects** between the fluxes. With this term, we refer to the particular behaviour of the flux Φ_d and Φ_q to be both functions not only of the current on the own axis but also of the one on the other axis. In this sense, their behaviours are not linear, since they depend on both current components. To be more precise, it can be said that, once fixed i_d , in case of a i_q component, the Φ_d will be slightly higher if it increases. For instance, in the moment in which the current along the d -axis is zero, it will be observed a value of flux linkage that is not equal to the that produce by the PMs, but slightly higher than it. On the other hand, a decrease in the value of the flux linkage Φ_q can be observed as soon as the i_d augments [56]. It seems clear that if the phenomenon is

neglected, the accuracy of the model will be dramatically affected, especially in machines like those where a big cross coupling effect can be observed [57].

To confirm this, in the early stages of the thesis, it has been tried to solve the reluctance network without coupling the axes. To do that, the two circuits has been implemented in Simulink and then, the torque calculated from it, has been compared to that of FEMM 4.2. The results have shown, that, in this case, the error could reach non feasible values, reaching 40 % to 50%. To solve the problem, the two circuits has been coupled together through the non linearity of the machine itself, as it will be explained the in paragraph 5.2.2. In order to understand the concept, before entering into the descriptions of the two circuits, it is better to observe the behaviour of the magnetic materials whom the motor is composed with.

5.2.1 Magnetic materials in the machine

In order to understand some phenomena happening inside the motor, it is of interest deepening into the magnetic materials present in it. There are two kinds:

- electrical steel;
- permanent magnets.

Both belong to the category of *ferromagnetic materials*. The ferromagnetism is the property of some materials to be highly magnetized, if subjected to an intense magnetic field and to preserve the feature even in case it disappears. They present a peculiar $B-H$ characteristic, where B is the flux density and H stands for the magnetic field.

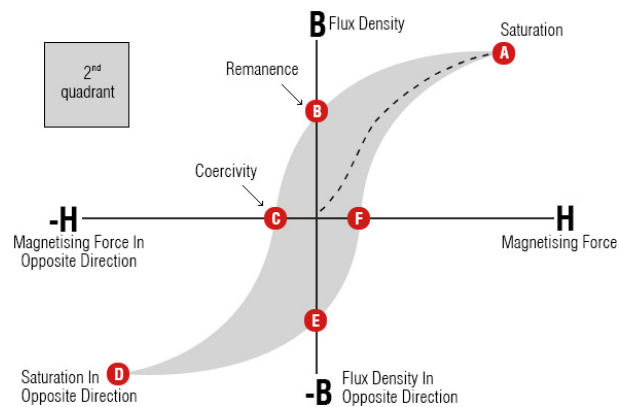


Figure 5.3: $B-H$ curve of ferromagnetic material [58].

As it can be seen from figure 5.3, this particular characteristic is represented by a *hysteresis cycle*. Starting from a non magnetized material and applying a magnetic

field H to it, the flux density B increases according to the first magnetization curve, till the maximum value H_m . After a certain value of H , the flux density tends to be constant, because it has reached its **saturation** point. The corresponding value of B to that point is called *saturation limit*. Once reached the value, the H is forced to decrease until it reaches the flux density axis, in which the relationship $H = 0$ is respected. Because of the fact the material has gained a magnetization, the corresponding B is not 0 but B_r , called **Remanence**. If the H continues to decrease, it reaches a value in which it is possible to complete demagnetize the the material and it is called *coercivity* and indicated with H_c . Augmenting the magnetic field, we observe a symmetric behaviour respect to the first quadrant. Varying the magnetic field across H_m and $-H_m$, we will go through the hysteresis cycle.

From it, it is possible to introduce a quantity called **magnetic permeability**, which stands for the capability of the material to get magnetized and it is equal to:

$$\mu = \frac{B}{H} \quad (5.4)$$

Accordingly to what said before, μ will not be constant in these materials, due to the **non linearity** of the magnetic behaviour. In particular, from figure 5.3, it seems clear that, at the beginning of the cycle, the ratio, so the μ is practically constant. On the other side, once reached the *knee* of the curve, the saturation phenomenon happens and μ faces a decrease. This behaviour will be the cause of most of the choices taken during the construction of the two reluctance networks, as it will be observed in the paragraph 5.2.2.

Electrical steel

As known, the steel is an alloy, composed by iron and carbon. The presence of the carbon makes the material stronger and resistant form a mechanical point of view, especially in machines that reaches high speed and, consequently, are subjected to high centrifugal forces. However, nowadays, the electrical machines are composed by silicon steel; to be more precise, the laminated core of the motor is composed by this material. It is used in order to *drive* the magnetic flux along paths that present a higher μ , so that it can be persuaded to follow more that.

Increasing the percentage of silicon will be helpful to reduce the amount of **iron losses**: it exists two kind of iron losses:

- the eddy currents losses;
- hysteresis losses.

In the first case, the losses are due to the effect of the flux that flows in the iron core: according to the Faraday-Lenz principle, the variation in the time of flux

density, produce currents inside the core, causing extra losses. The phenomenon is due to the electrical conductivity of the iron itself. This is not the only parameters that counts: they increase with the frequency and the intensity of B and also with surface of the conductive material. This is the reason why the core of the motor is laminated, so that the area in which the currents flow is smaller. In this sense, the stacking factor can be introduced as:

$$K_{st} = \frac{\delta}{\delta + \delta_{is}} \quad (5.5)$$

where δ is the width of one sheet and δ_{is} is the space between two of them. Classical values range between 0.92 to 0.96. Adopting the silicon steel is useful to increase the resistivity of the material, thus, to reduce the eddy currents.

On the other hand, the hysteresis losses are a phenomenon that is strictly connected to the B - H characteristic. The phenomenon can be explained looking at the curve in figure 5.3. Considering the magnetic energy variation, it can be expressed through the following expression:

$$\frac{dW_m}{V_{fe}} = HdB \quad (5.6)$$

where W_m is the magnetic energy and V_{fe} is the core volume. If a positive variation of dB happens, the quantity above presented is the area inside the cycle and delimited by the curve and the B axis. It can be seen that in case of an alternative source, the flux density ranges cyclically from $-B_{max}$ to B_{max} . Graphically, it can be observed that the increase of the energy going from $-B_{max}$ to B_{max} is lower than the energy lost in the opposite path. The difference gives the hysteresis cycle. Every time the cycle is crossed, an amount of energy is lost because of this. It follows that they are linked to the frequency of supply.

It exists different way to consider both losses in the iron. In the work, the Steinmetz approach has been used to model them, through the following expression, derived from [59].

$$P_{iron} = k_{add}(k_{hys}\omega + k_{edd}\omega^2)(V_t B_t^2 + V_y B_y^2) \quad (5.7)$$

where k_{hys} and k_{edd} are coefficients related to hysteresis and eddy currents losses; ω is the electrical speed, V_t and B_t and V_y and B_y are respectively the volume and the flux density in the teeth and the yoke. The k_{add} is the parameter that takes into account additional effects.

Permanent magnets

These materials are considered as magnetic flux source. For this reason, they are required to have an high value of Remanence B_r : if the value is remarkable, it means that it is possible to produce flux without current (so, magnetic field H). As a consequence, the value $-H_c$ gains importance, because it can be considered as the magneto motive force needed to completely demagnetize the PM. Following what said above, the second quadrant is the only one in which they should operate. The most common permanent magnets are the *Alnico 5*, the *Samarium-cobalt*, and especially for the electric vehicles, the *neodymim-iron-boron*(NdFeB).

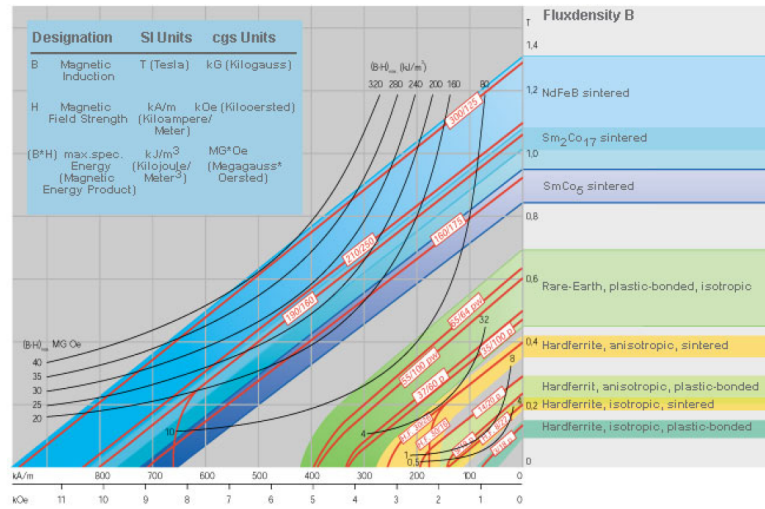


Figure 5.4: Demagnetizing curve of the most common PM materials.

As it can be seen from the figure 5.4, the NdFeB seems the most promising one, because they can allow higher B_r and H_c , making them very good flux sources and also very difficult to demagnetize. In fact, the entire industry faced a significant advance with the discovery of the rare earth materials.

Another important parameter to understand how good is the material is to know its *maximum energy product*. With the term, we refer to the highest $B-H$ product, that matches a point in the hysteresis loop. The higher will be the quantity, the smallest volume will be required to produce the fixed flux density [60].

A particular feature of the demagnetizing curve is its dependence on the temperature. In case of a higher temperature, the working point of the magnet will go inside the curve and, consequently, the Remanence and the coercivity will be lower. If the working point maintains itself in the linear part of the $B-H$ curve, it is always possible to come back to the original values. Whereas, if the temperature overcomes the limit value, called *Curie's temperature* T_c , the magnetic material

loses its magnetic features. It follows that it is extremely important to control the temperature inside the motor, in which high temperature could be easily reached. In that unfortunate event, after having reached again the initial temperature, it could be feasible to recreate the magnetization. Of course, this path cannot be followed in an electrical machine in which the permanent magnets cannot be changed.

5.2.2 Description of the reluctance network

The description of the reluctance networks modelled for the machine can be now done. To simplify the discussion, it has been divided according the two axes.

d-axis

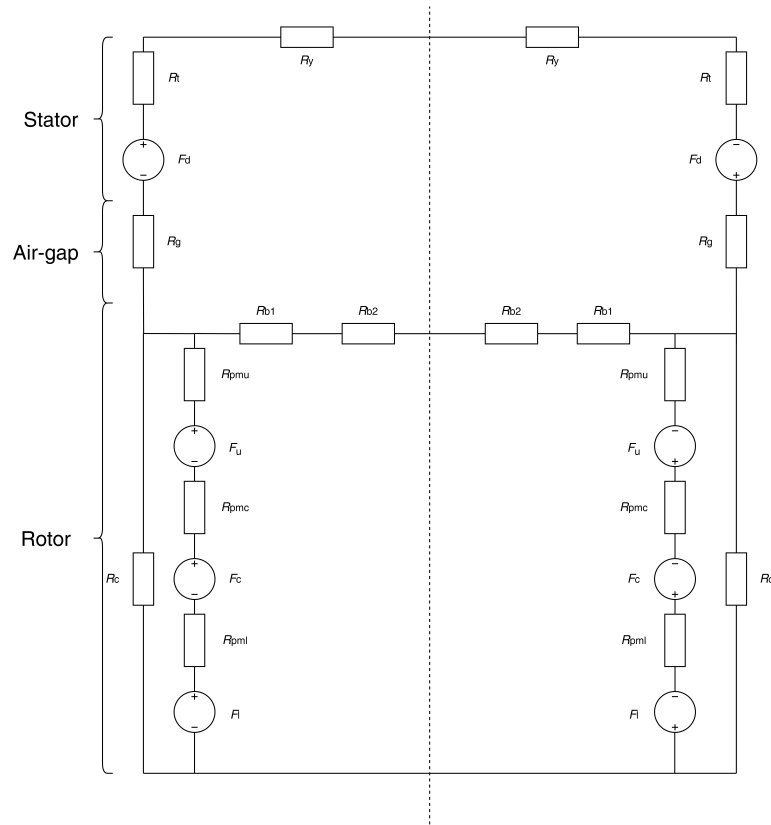


Figure 5.5: *d*-axis reluctance network of the machine.

As it can be seen from figure 5.5, the circuit has been divided into three macro section: rotor, air-gap and stator and they will be described following this order.

Rotor

Starting from the rotor, it can be observed that the three magnetic barriers have been modelled as three magnetic voltage sources, following the Thevenin representation. Their values can be easily found considering the *Ampere's law* and the *Hopkinson's law*:

$$\oint_{\partial S} \mathbf{H} \cdot d\mathbf{r} = NI = R\Phi \quad (5.8)$$

where ∂S is a closed line.

In the case of interest, the H is equal to the coercivity of the permanent magnet and d corresponds to the height of the barrier as the figure 5.6 shows. Furthermore, the scalar product becomes a simple product due to the parallelism.



Figure 5.6: Permanent magnet dimensions.

Thus, the magnetic voltage can be obtained as followed:

$$F_{PMi} = H_c l_{PMi} \quad (5.9)$$

for $i=l,c,u$, thus to lower, central and upper barrier.

Consequently, the related reluctances are not affected by non linearity and, so, the definition can be applied without any problem:

$$R_{PMi} = \frac{h_{PM}}{\mu_{PM} w_{PM} L} \quad (5.10)$$

for $i=l,c,u$, where L is the length of the permanent magnet, μ is the magnetic permeability of the PM, that is usually equal to that of the air.

As far as the bridges are concerned, all of them are affected by the non linearity. As already told, these parts are subjected to high saturation. For these reasons, the μ is not a constant value but a function of the flux density. Starting from the upper bridges, it has been indicated a reluctance for both central and upper barrier, R_{b1}

and R_{b2} . The lower barrier does not require it because of the particular geometrical configuration.

$$R_{b1} = \frac{w_b}{\mu(B)l_c L} \quad (5.11)$$

$$R_{b2} = \frac{w_b}{\mu(B)l_u L} \quad (5.12)$$

$$(5.13)$$

where, the l_c and l_b are respectively, the length of the upper air barrier for the central and the upper barrier.

On the other hand, R_c is the reluctance that considers the flux behaviour between the magnets. This area will be highly saturated too and, consequently, subjected to non linearity. The reluctance has been obtained through integration along the height of the area, as the figure 4.10 and 5.7 shows.

Following what said above, R_c is obtained as followed:

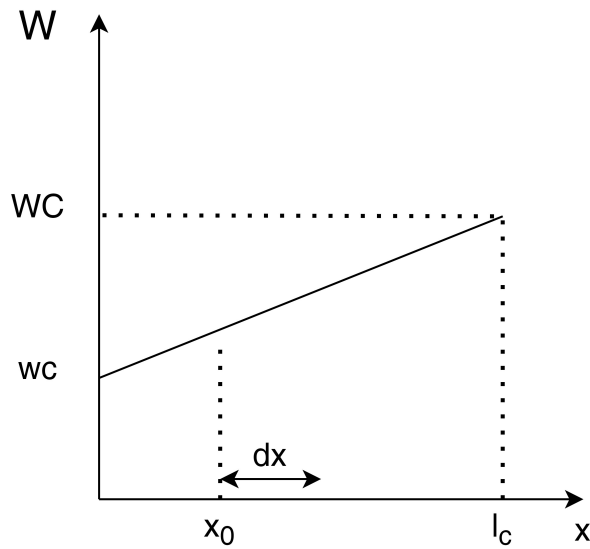


Figure 5.7: Integration of the reluctance.

$$r(x) = \frac{dx}{\mu_c(B)L \left[(W_c - w_c) \frac{x}{l_c} + w_c \right]} \quad (5.14)$$

$$R_c = \int_0^{l_c} r(x) = \frac{l_c}{\mu_c(B)L(W_c - w_c)} \left[\ln\left(\frac{W_c - w_c}{w_c} + 1\right) \right] \quad (5.15)$$

The air-gap can be modelled with the following reluctance, that presents the following expression:

$$R_g = \frac{g}{\mu_0 l_g L} \quad (5.16)$$

where μ_0 is the magnetic permeability of the air, g is the air-gap height and l_g its length and can be expressed as followed:

$$l_g = \frac{p(R_r + \frac{g}{2})}{p} \quad (5.17)$$

As it can noticed, the length has been calculated referring to the centre of the air-gap, in order to have a more precise trend of the actual flux behaviour.

As far as the stator is concerned, consistently to what explained before, the magneto-motive force produced by the current has been modelled with a voltage source. This is one of the most interesting benefits that comes the approach: the possibility to act directly on this element facilities incredibly the control and make easier the design of the winding as well. In particular, F_d has been defined as follow:

$$F_d = N_s i_d \quad (5.18)$$

where N_s is the number of turns per phase and per pole.

The last two elements represent the magnetic flux behaviour across the teeth and the yoke: none of them shows a non linear behaviour, so it has been applied an expression similar to the reluctance of the air-gap. For, the stator teeth, we have:

$$R_t = \frac{p h_t}{\mu_{ir} Q_s w_t L} \quad (5.19)$$

where w_t is the width of the teeth. The term $\frac{Q_s}{p}$ appears and it represents the number of slots per pole. It has been used in order to take into account all the teeth in the pole. In particular, it decreases the value of this resistance: in fact, the flux will flow in more than one tooth, which means that the magnetic resistance to its passage is reduced.

The stator yoke reluctance is described by the following expression:

$$R_{ys} = \frac{l_y}{\mu_{ir} h_{ys} L} \quad (5.20)$$

where h_{ys} is equal to the stator yoke height and l_{ys} is its length for one pole and expressed as follow:

$$l_{ys} = \frac{\pi(R_s - \frac{h_{ys}}{2})}{p} \quad (5.21)$$

The length has been calculated at middle height for this case too.

q-axis

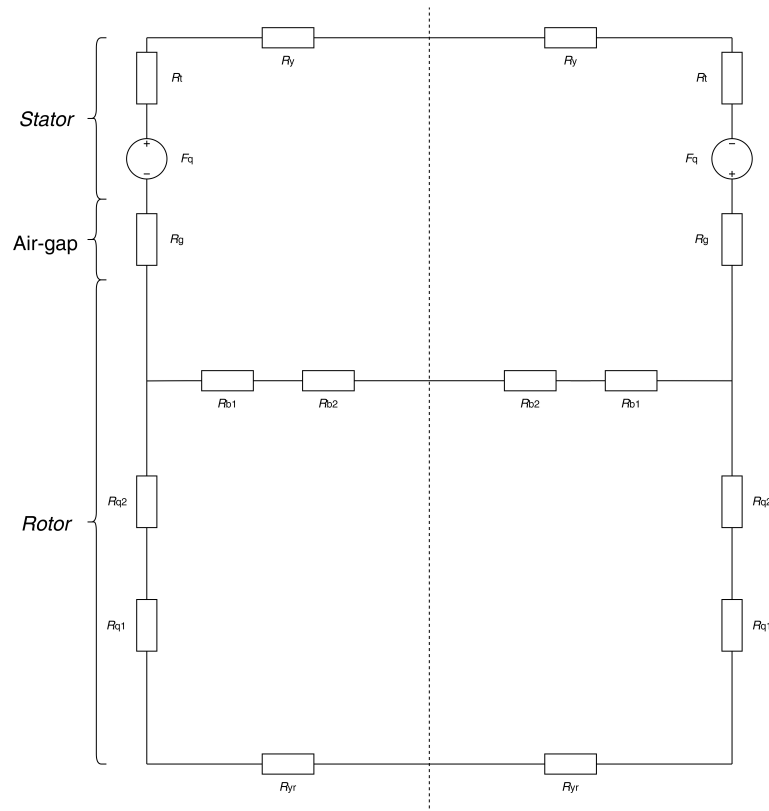


Figure 5.8: *q*-axis reluctance network of the machine.

As the figure 5.8 shows, the reluctance network of the *q*-axis ends up being simpler than the *d*-one. The rotor does not host any magnetic flux source, but only the reluctance R_{q1} and R_{q2} . Referring to the figure 4.11, they have been set in order to model the flux along the axis, dividing the area in two parts: an upper part whose height is l_t and delimited by W_{qt} and W_q and a lower one whose height is l_q and delimited by W_q and W_Q . The formulas of the reluctances have been found in the

same exact way of R_c , making the proper substitutions.

$$R_{q1} = \frac{l_q}{\mu_{q1}(B)L(W_Q - w_q)} \left[\ln\left(\frac{(W_Q - w_q)}{w_q} + 1\right) \right] \quad (5.22)$$

$$R_{q2} = \frac{l_{qt}}{\mu_{q2}(B)L(W_{qt} - w_q)} \left[\ln\left(\frac{(W_{qt} - w_q)}{w_q} + 1\right) \right] \quad (5.23)$$

For the q axis, the rotor yoke has been modelled because it has an important role in understanding the magnetic behaviour of the machine. Thus:

$$R_{yr} = \frac{l_{yr}}{\mu_{ir}h_{yr}L} \quad (5.24)$$

where h_{yr} is equal to the rotor yoke height and l_{yr} is its length for one pole and expressed as follow:

$$l_{yr} = \frac{\pi(R_o - \frac{h_{yr}}{2})}{p} \quad (5.25)$$

The air-gap is modelled with the same reluctance of d -axis, whereas the only difference in the stator concerns with the different current component adopted which is, in this case, the q one.

The part that must be deepen is the bridges one. As already said, the main problem of the whole approach was **having initially neglected the cross coupling** between the two axis. In order to solve it, it has been fought to add an *additional path* in the q -axis which links the two poles. It is represented by the bridges considered along the d -axis, that are known to be an intensely saturated part of the machine. In other words, the cross coupling has been obtained **through the non linearity of the circuit**. Doing that, the influence of the latter axis will be always present on the other one and vice versa.

It has been done the following hypothesis: the flux density of the two bridges along d -axis are equal and named B_{bD} . The same reasoning can be done with those along the other axis; in this case the flux density has been called B_{bQ} . In conclusion, it has been defined a unique flux density for all the bridges expressed as follow:

$$B_b = \sqrt{(B_{bD})^2 + (B_{bQ})^2} \quad (5.26)$$

5.2.3 Solution of the Reluctance network

The next step has been solving the two magnetic circuits in order to obtain the electromagnetic torque value. Unfortunately, the non linearity is a phenomenon

that hugely affects the proposed method, especially from the solution point of view. In fact, it has been necessary to implement a method of solving for systems of non linear equations. For those systems, the solution cannot be found in a close way, but it is required to use an iterative method, in which the solution is always updated in order to get closer to real value. For the thesis, it has been applied one of most common iterative method, the so called *Newton-Raphson method*. It is a numerical method that gives an approximated solution of an equation that present the following expression $f(x) = 0$. In order to find the root, a proper range has initially to be set. The main idea of the method is to substitute the curve $y = f(x)$ with the tangent to it. The intersection between this curve and the $f(x) = 0$ axis will be the new solution, as the figure 5.9 clearly shows.

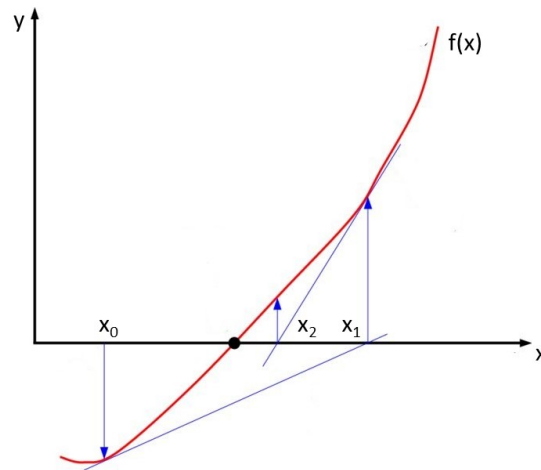


Figure 5.9: Graphical representation of Newton-Raphson method.

The blue lines represent the tangent to the curve $f(x) = 0$. As it can be seen, at each new iteration a new value x_i is found and in correspondence of that point, the new tangent is drawn, until the last solution is close *enough* to the real root. From an analytical point of view, we imagine to have the following function $f(x)$ and an initial point x_0 . The tangent to the curve in that point can be expressed as follow:

$$f(x_1) = f(x_0) + f'(x_0)(x_1 - x_0) \quad (5.27)$$

where $f'(x_0)$ is the derivative of the function in that point but also the slope of the

tangent. From it, the new approximation is found:

$$x_1 = x_0 - \frac{f(x_0)}{f'(x_0)} \quad (5.28)$$

$$Res = x_1 - x_0 \quad (5.29)$$

where *Res* is called *Residual* and it is expected to become equal to zero as fast as possible. The euclidean norm of it gives the *error* on the method. In the iterative methods, a key aspect is the number of iterations that are needed to make the algorithm converge. To be clearer, there are two options:

- Set a number of maximum iteration;
- Set a tolerance on the final solution.

In the first case, the algorithm would immediately stop being executed when the number of maximum iterations has been reached. This would decrease the speed of convergence of the method, because all the iterations would be required to be explored even if the solution was not becoming more accurate anymore. On the other hand, what is usually done is to rely on the tolerance: if the error is higher than the tolerance, the algorithm will continue working, otherwise it will stop. This method is very powerful because of rapidity with whom is converging. In fact, it a quadratic convergence, which basically means that the accuracy doubles at each step.

In the case in which we have a system of a non linear equations, like in this project, the derivative is substituted by the *Jacobian matrix*. It contains the derivatives of all the functions, respect to all variables.

Coming back to the project, the roots required to be found are the flux densities of the non linear parts, namely, the ones of the bridges and on the *q*-axis. The figure 6.2 clearly explained what procedure has been set. It provides for solving both the circuits together, simplifying them with the basic principles of electrical circuits, like the series or the parallel relationship between the reluctances or applying voltage or current dividers.

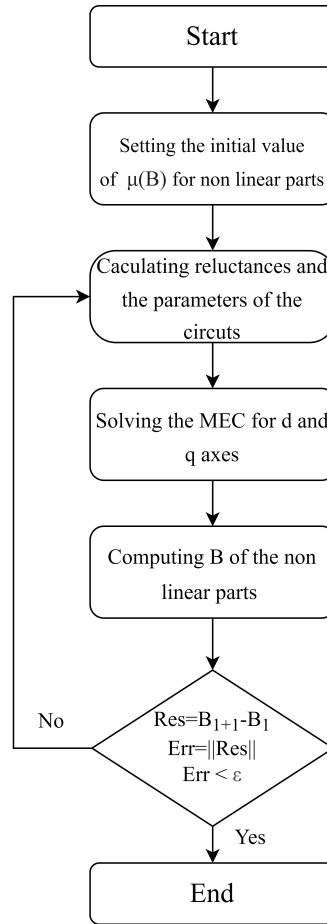
Once obtained the value of the magnetic flux in each part of the circuit, the new value of flux density is found applying the following expression:

$$\Phi = \int \mathbf{B}d\mathbf{S} = BS \quad (5.30)$$

$$B = \frac{\Phi}{S} \quad (5.31)$$

where *S* is the surface in which the magnetic flux flows.

In this case, it has been implemented a simplified version of the Newton method,



H

Figure 5.10: Solution path of the MEC.

called *Quasi – Newton* method. Because of the high complexity of the Jacobian matrix, it has been substituted by a constant value. The new expression will be:

$$Res = B_{i+1} - B_i \quad (5.32)$$

$$B_{i+1} = B_i - \gamma Res \quad (5.33)$$

$$B_{i+1} = \gamma B_{i+1} + (1 - \gamma) B_i \quad (5.34)$$

where γ is a constant value already fixed.

As it can be seen, the equation solved is an implicit one. The value of γ is adopted to let the algorithm proceed with a certain speed: opting for a lower γ value will drop the speed of convergence. Sometimes, this approach is used to avoid the algorithm makes too big steps and then failure in converging.

5.3 Validation of the tool

At this stage, the tool has been validated in order to trend its accuracy and the computational time. To to that, the software FEMM 4.2 has been employed as a good reference for testing different cases. The comparison between Matlab and the finite elements software has been conducted on the electromagnetic torque value and on the flux density in the air-gap at no load condition.

The test has been done on two different possible designs; both of them takes inspiration from the Toyota Prius V-type IPM motor, showed in [61]. The only difference concerns in the shape and the number of the V-type barriers. In this case, due to the different rotor geometry, it has been tried to set the input parameter of the rotor structure in order to have a similar shape. Furthermore, the tests has been done to check the geometry function had been well implemented too.

5.3.1 Test 1

In the table 5.1 are shown the initial design dimensions and parameters chosen for this first test. Given these first inputs, it has been possible to obtain the lengths of the magnets barriers through the function *magnetdesign.m*, in order to have the needed quantities to calculate all the reluctances. Their values are shown in table 6.3. In this way, it has been possible to draw the design of the motor in *Autocad*, depicted in figure 5.11.

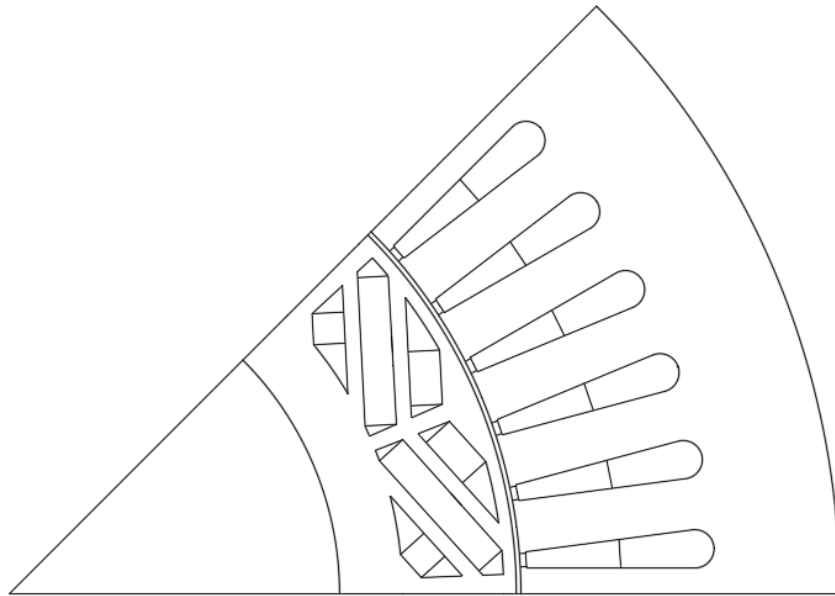


Figure 5.11: Design of the *Test 1* IPM motor.

	Symbol	Quantity	Unit of measurement
Main dimensions			
Poles	p	8	
Slots	Q_s	48	
Rotor outer radius	R_r	80.6	<i>mm</i>
Stator outer radius	R_s	132	<i>mm</i>
Stack length	L	60.7	<i>mm</i>
Air-gap	g	0.73	<i>mm</i>
Stator			
Teeth height	h_t	30.7	<i>mm</i>
Teeth width	w_t	8.2	<i>mm</i>
Slots width	w_s	0.45	<i>mm</i>
Yoke height	h_{ys}	19.73	<i>mm</i>
Number of turns per pole and phase	N_s	14	
Filling factor	k_{fill}	0.4	
Rotor			
Rotor shaft radius	r_o	0.6514	<i>p.u.</i>
Bridges height	w_b	2	<i>mm</i>
Yoke height	h_{yr}	10	<i>mm</i>
Magnet inclination angle	θ_{PM}	0.7	<i>rad</i>
Pole pitch coefficient	k_{pit}	0.9	<i>p.u.</i>
Middle bridge coefficient	k_c	0.05	<i>p.u.</i>
Magnet height	h_{PM}	5	<i>mm</i>
Barriers distance coefficient	k_i	0.5	<i>p.u.</i>

Table 5.1: Dimensions of the motor.

The lengths of the magnets barrier are, then, summarized in the following table:

	Symbol	Quantity	Unit of measurement
Central barrier length	l_{PMc}	23.7	<i>mm</i>
Upper barrier length	l_{PMu}	9	<i>mm</i>
Lower barrier length	L_{PMl}	4.6	<i>mm</i>

Table 5.2: Lengths of the magnets barriers.

In order to proceed, we have fixed the properties of the material employed in the

motor, in particular as far as the iron and the permanent magnets are concerned.

	Symbol	Quantity	Unit of measurement
Electrical steel	ISOVAC	M330 – 50A	
PM Remanence (NdFeB)	B_r	1.24	T
thermal coefficient	k_{cv}	25	$\frac{W}{m^2K}$
Ambient temperature	T_{amb}	20	$^{\circ}C$
Maximum temperature	T_{max}	120	$^{\circ}C$

Table 5.3: Materials chosen for the motor.

It is now possible to calculate the stator resistance, applying the expression taken from [59]:

$$R_s = \rho_{cu} L_{wind} \frac{6ppN_s}{k_{fill}\pi(1 - k_t((R_r + g + h_t)^2 - (R_r + g)^2))} \quad (5.35)$$

where ρ_u is the copper resistivity at the maximum temperature and L_{wind} is the length of the winding expressed in this way:

$$L_{wind} = L + \frac{1.2\pi(R_r + g)}{pp} + 0.05; \quad (5.36)$$

Thanks to it, the maximum current of the machine can be found. In fact, the value has been retrieved imposing a *thermal limit*: considering only the convention phenomenon, through the area of the entire motor, the maximum current is obtained as follow:

$$I_{max} = \sqrt{\frac{(T_{emg} - T_{amb})h_{cv}S_{th}}{3R_s}} \quad (5.37)$$

with:

$$S_{th} = D_s\pi L + 2\pi\frac{D_s^2}{2} \quad (5.38)$$

So, we obtain:

- $R_s = 0.0579\Omega$
- $I_{max} = 46.73A$

The first step in building the tool, has been to define a function to represent the *reluctivity* of the magnetic materials for the non linear parts. Once taken the value

of B - H curve, from [62], it has been possible to obtain an expression of the inverse of the magnetic permeability, following shown:

$$\nu(B) = aB^{b-1} + c \quad (5.39)$$

where a, b, c are coefficient that help to follow better the trend of the data shown in figure 5.12 with the name *ISOVAC*. They have been obtained with the *curve fitting tool* of Matlab and they are equal to $a = 5.81$, $b = 13.14$, $c = 35.04$.

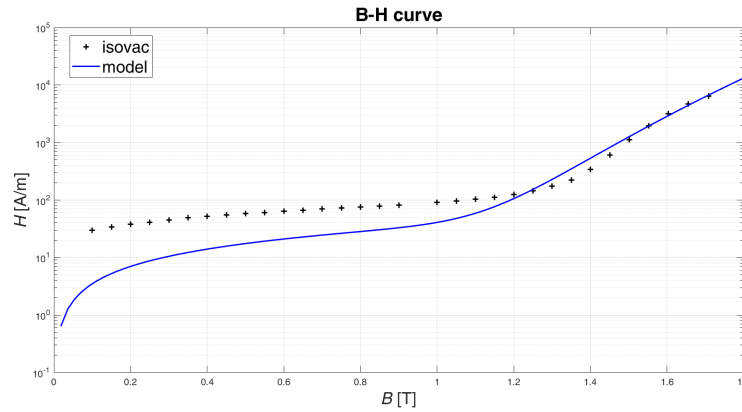


Figure 5.12: Design of the *Test 1* IPM motor.

The next step is to make the simulation run and obtain the electromagnetic torque to be compared with the FEMM 4.2 results. Before doing it, a first check has been done on the air-gap flux density along the d -axis in no load condition.

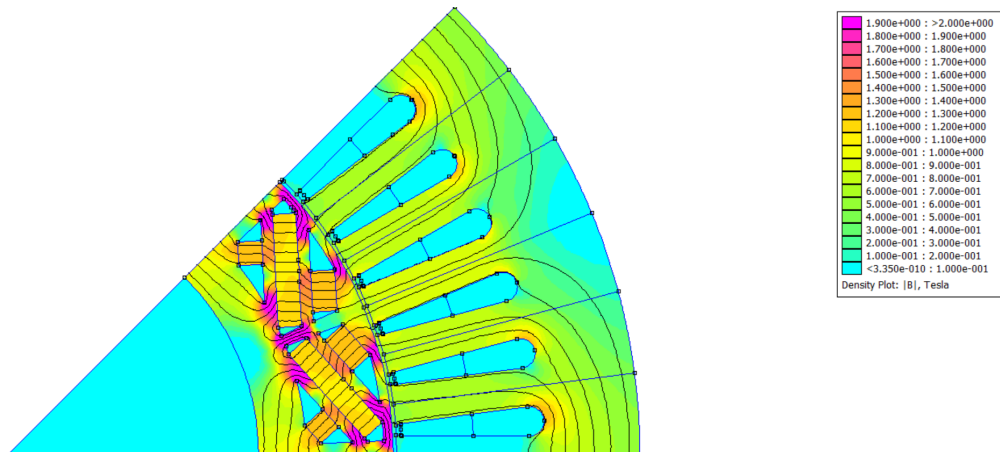


Figure 5.13: FEM simulation in no load condition: flux density and magnetic flux path.

The value obtained from FEMM 4.2 is **0.736 T**, whereas Matlab gives **0.664 T**. It means the error is equal to **10.8 %**, considered acceptable, considered the particularity of the geometry and the grade of precision with whom the magnetic path has been represented.

In testing the tool, it is also possible to observe the effectiveness of the iterative method and see in how many iteration it will converge.

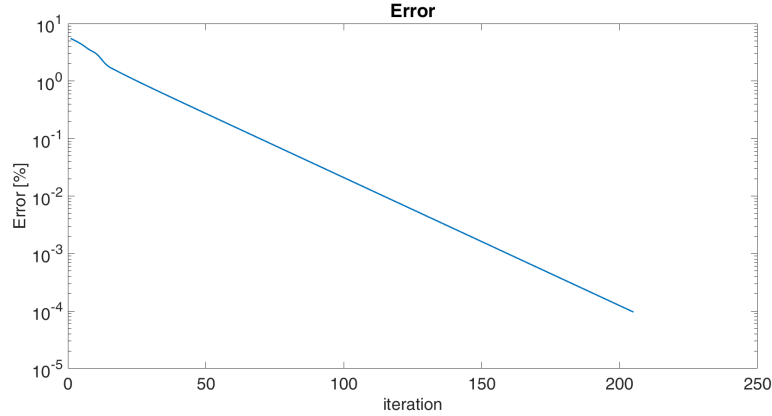


Figure 5.14: Error on the iterative method.

The method adopted seems working fine, taking 205 iteration to reach a value under the tolerance once. Its speed can be increased if the relax coefficient is wisely increased.

To obtain the accuracy of the tool, a series of test have been implemented: it basically means that for a set of different currents we have checked the electromagnetic torque and compared with the finite elements method one. From the current point of view, the difference hides in the planes used: for the FEM simulation the i_a, i_b, i_c components are needed, whereas in the reluctance network, the $d-q$ ones be used.

I_m [A]	γ [°]	i_d, i_q [A]	i_a, i_b, i_c [A]
40	30	-24.5 42.6	34.6 0 -34.6
50	20	-20.9 57.54	46.98 -8.68 -38.3
60	35	-42.14 60.19	49.19 5.22 -54.37
60	60	-63.63 60.19	30 30 -60
25	70	-28.74 10.47	8.55 16.06 -24.62
55	75	-65 17.43	14.23 38.89 -53.1
75	40	-59 70.36	57.45 13.1 -70.47

Table 5.4: Current components in the cases.

where γ is the angle between the current vector and the q -axis. It has been tried to explore as wide as possible the combinations, in order to have an overall idea of the accuracy.

Finally the torque values are shown in the following table:

RN [Nm]	FEM [Nm]	Error [%]
82.51	98.36	19.2
102.91	124.83	21.3
123.91	151.17	22
141.33	173.7	22.9
35.214	39.47	12.1
75.34	89.58	18.9
152.94	191.79	25.4

Table 5.5: Torque computation and relative error.

As it can be noticed, the error fluctuates around the 20 % as expected. Considering the results obtained, we can say that the tool has been validated. Furthermore, it is possible to notice that the error tends to be higher in the case in which the amplitude of current is higher. This phenomenon can be justified by the level of saturation reached: when the level of the flux density overcomes the 3 T, the tool loses its accuracy and also the results from FEMM cannot be considered reliable anymore.

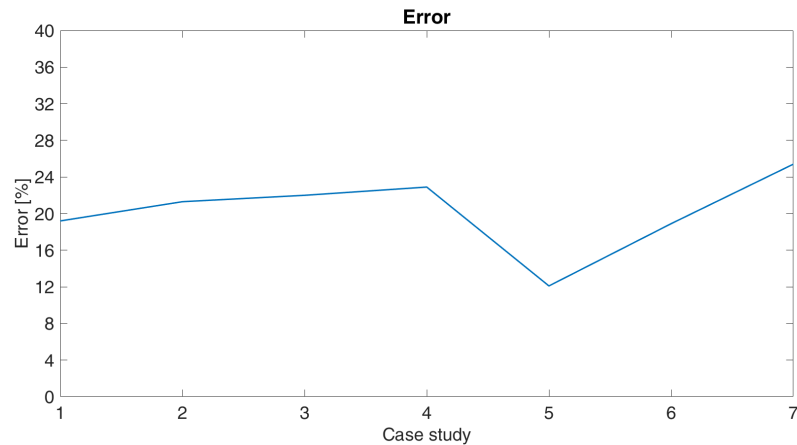


Figure 5.15: Error on the torque.

Flux and torque map

Once, validated the tool for a series of cases, it has been also possible to find the flux maps for Φ_d and for Φ_q , introducing an *for cycle* trough which explore all the possible components for a negative i_d and a positive i_q . They have been fundamental to proceed with the control and the optimization part. The map fluxes of *Test 1* are shown in figure 5.22 and 5.23

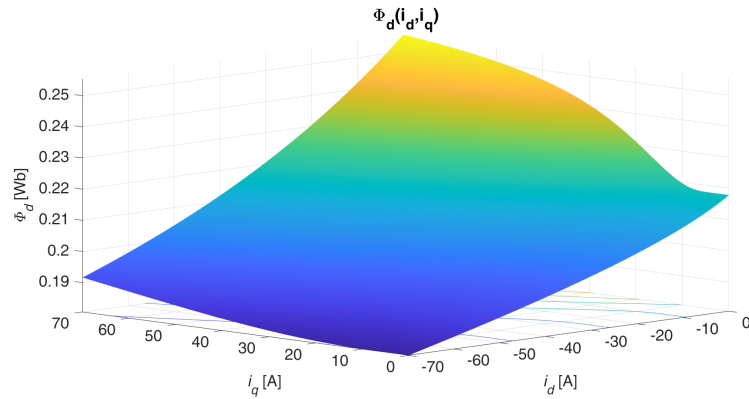


Figure 5.16: Φ_d flux map for *test 2*

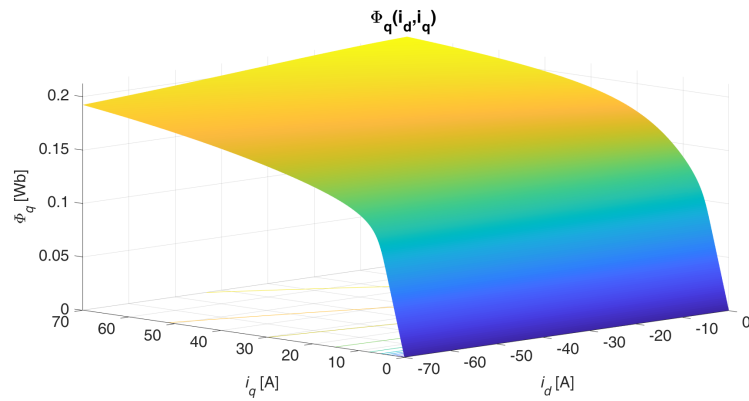


Figure 5.17: Φ_q flux map for *test 1*

With the same proceeding, it is possible to track the trend of torque respect to the current components.

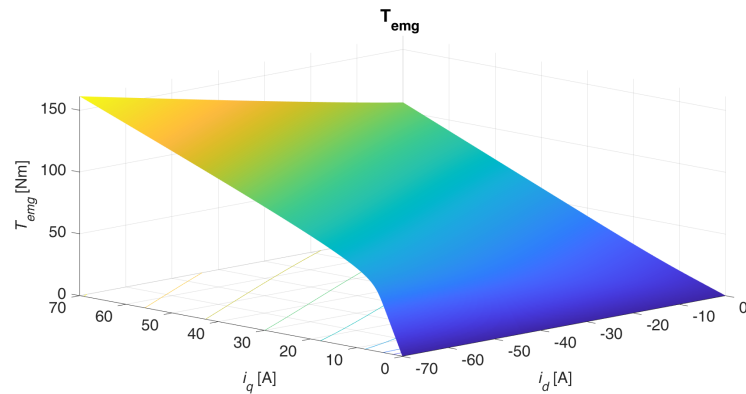


Figure 5.18: Torque map for *test 1*

5.3.2 Test 2

A second test has been conducted in order to have a further proof of effectiveness of the method adopted and to check the accuracy. Furthermore, it has been possible to see that the *magnetdesign.m* is working as expected, giving results that are consistent to the effective available magnet area. The steps are equal to the previous one and the choice of the materials too. The difference between the tests concerns the different geometrical dimensions adopted, in particular as far as the rotor ones are concerned. In the same way of the previous design, in the table 6.2, all the main dimensions are shown. The figure 5.19 depicts the machine design of this new motor.

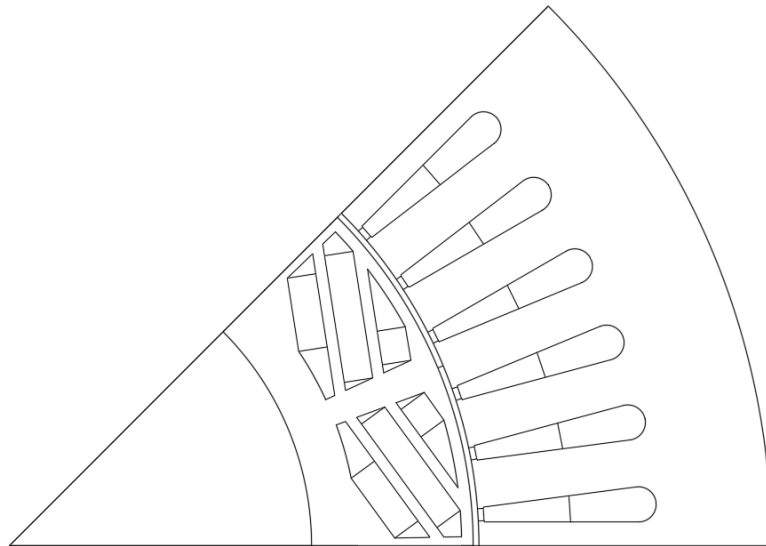


Figure 5.19: Design of the *Test 2* IPM motor.

	Symbol	Quantity	Unit of measurement
Main dimensions			
Poles	p	8	
Slots	Q_s	48	
Rotor outer radius	R_r	80.33	mm
Stator outer radius	R_s	132	mm
Stack length	L	60.7	mm
Air-gap	g	1	mm
Stator			
Teeth height	h_t	30.7	mm
Teeth width	w_t	8.2	mm
Slots width	w_s	0.45	mm
Yoke height	h_{ys}	19.73	mm
Number of turns per pole and phase	N_s	14	
Filling factor	k_{fill}	0.4	
Rotor			
Rotor shaft radius	r_o	0.6514	$p.u.$
Bridges height	w_b	2	mm
Yoke height	h_{yr}	8	mm
Magnet inclination angle	θ_{PM}	0.60	rad
Pole pitch coefficient	k_{pit}	0.95	$p.u.$
Middle bridge coefficient	k_c	0.1	$p.u.$
Magnet height	h_{PM}	5	mm
Barriers distance coefficient	k_i	0.4	$p.u.$

Table 5.6: Dimensions of the motor.

In the lines in red are representing the quantities that have been changed. We

	Quantity	Unit of measurement
Central barrier length	l_{PMc}	22.4 mm
Upper barrier length	l_{PMu}	6.3 mm
Lower barrier length	L_{PMl}	11.6 mm

Table 5.7: Lengths of the magnets barriers.

are expecting longer magnets, because we are using more space for them. In fact, as the table 5.7 shows, in the overall, the magnets have become bigger.

Now, the R_s and the I_{max} are obtained, presenting the following values:

- $R_s = 0.0579\Omega$
- $I_{max} = 46.5A$

As usual, the error of the d -axis flux density at no load is observed.

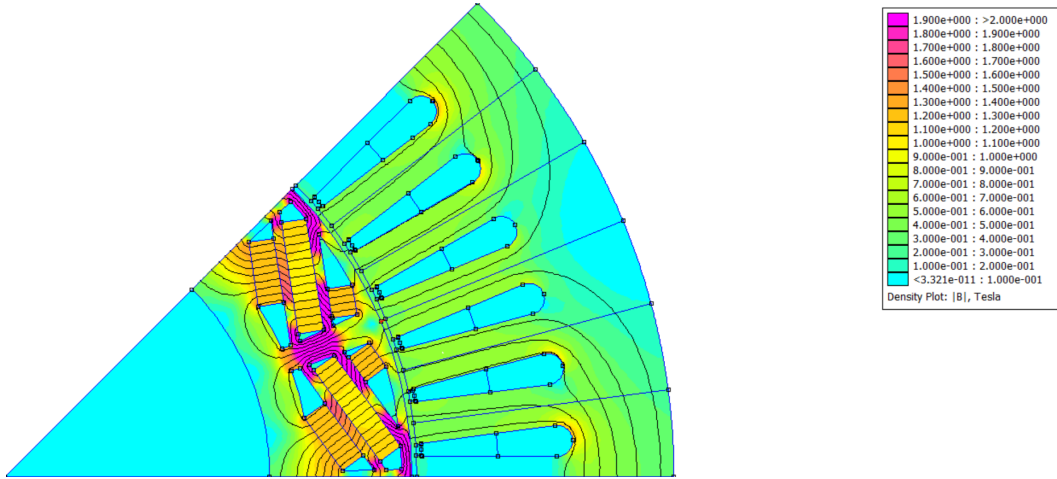


Figure 5.20: FEM simulation in no load condition:flux density and magnetic flux path.

As shown in figure 5.20, the air-gap flux density that FEM gives is equal to **0.53 T**, whereas the reluctance network **0.64 T**, observing an error of the **20.7 %**. In particular, due to the increased space in between the magnets, less flux is crossing the air-gap and more flux leakage will be present, making the bridge saturate more. The last step has been to check the value of electromagnetic torque in the same cases of the previous test.

RN [Nm]	FEM [Nm]	Error [%]
85.25	99.92	17.2
111.63	132.84	19.9
123.29	149.30	21.2
130.35	160.86	23.4
28.57	33.06	15.7
55.24	65.03	17.7
146.76	179.93	22.7

Table 5.8: Torque computation and relative error.

For this test too, the error seems to oscillate around the 20%. Sometimes the error is getting bigger because, in that particular case, the value of the saturated parts is becoming higher than 3 T, making the RN method losing accuracy.

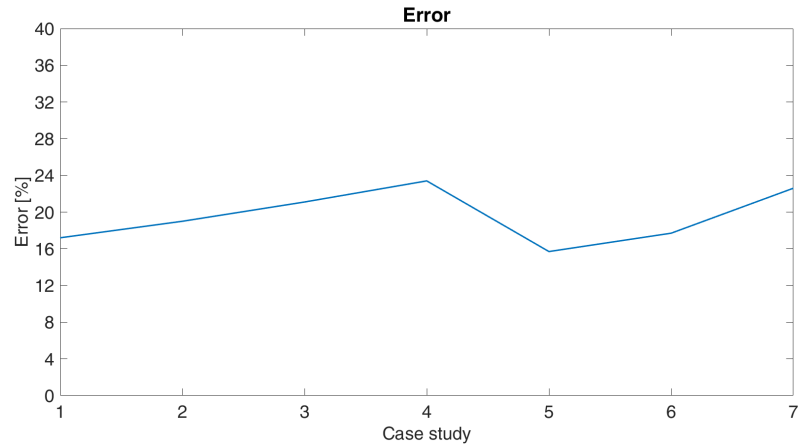


Figure 5.21: Error on the torque

Flux and torque map

As already done for *test 1*, the flux maps and torque one are retrieved for this machine.

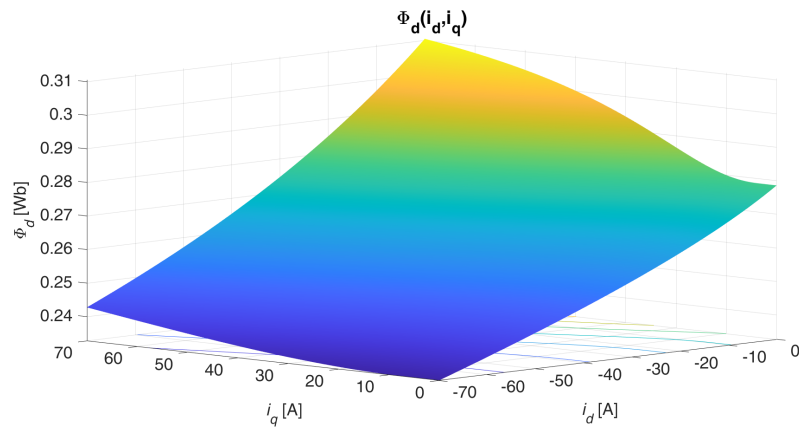


Figure 5.22: Φ_d flux map for *test 2*

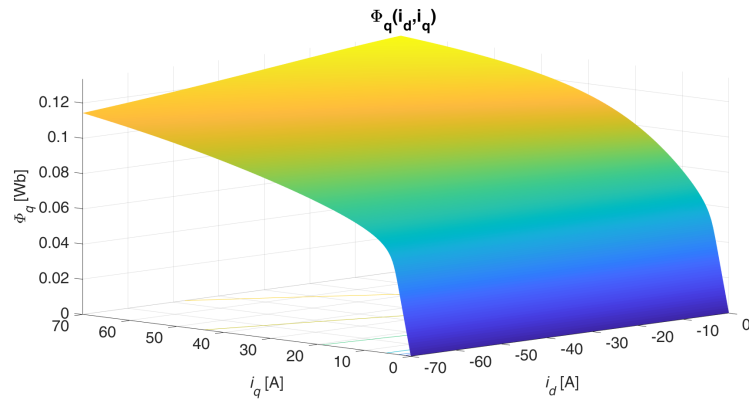


Figure 5.23: Φ_q flux map for *test 2*

The torque map is here shown:

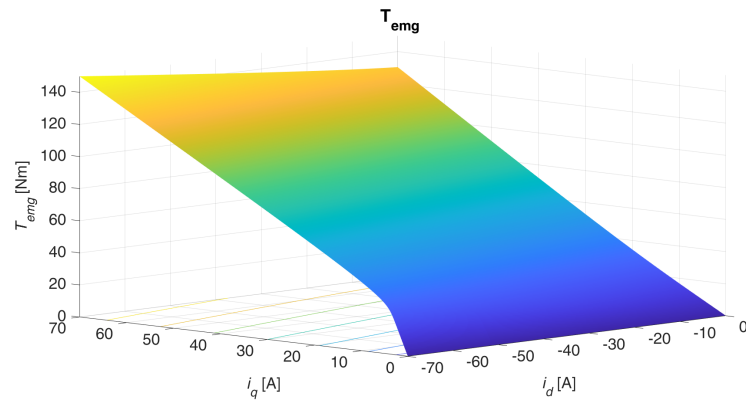


Figure 5.24: Torque map for *test 2*

5.3.3 Computational time

The parameter that marks the advantage of the reluctance network approach on the FEM one is the computational time.

In all the simulation done, the time needed by the finite elements software for one single simulation has ranged around the **7-8 seconds**. On the contrary, the computational time of the RN is incredibly small compared to the previous one. Using the Matlab stop-watcher *tic-toc*, the time has been retrieved: most of the simulations have presented a time equal to **0.007 seconds**. Understanding the benefit is straightforward. On the other hand, the accuracy error is still about the 20%.

Chapter 6

Control and optimization

In the last chapter, the control principles and the optimization process have been pointed out. In particular, it has been shown how to find the MTPA and MTPV loci to be adopted for an optimal control of the machine. Once obtained, it has been explained how the objective function to be maximized has been built. In the last part of the chapter, the results coming from the optimization algorithm, the particle swarm optimization, has been shown.

6.1 MTPA and MTPV loci

Once built an effective tool that allows to calculate the electromagnetic torque and through which is possible to monitor the magnetic flux behaviour in a fast way and with a reasonable grade of error, the next step is to *optimize* the design. To do this, we firstly need to have a machine that is well controlled in the WLTP working points. The reason is straightforward: through the optimization algorithm we are going to see which combination of parameters gives the highest efficiency in those working points, inside the desired $T-\omega$ characteristic. That working points are assimilated to a torque and a speed references that are the inputs of the optimization progress, together with the maximum torque requested. It follows a control law is needed in order to translate that requests in current components on the $d-q$ plane.

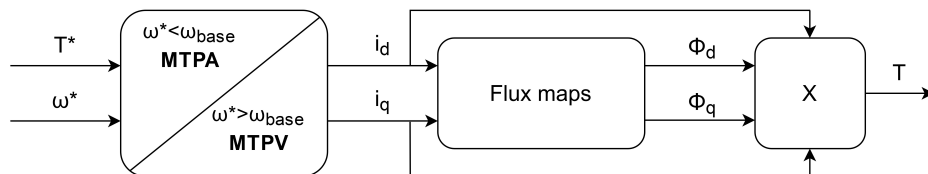


Figure 6.1: Control scheme.

As already explained in the chapter 2, in the paragraph 2.3.4, there are two laws to be followed in order to optimally control the machine: the MTPA and MTPV laws.

In the first case, MTPA stands for *Maximum Torque Per Ampere*, which basically means having the best exploitation of the current in order to obtain a certain amount of torque. This corresponds to solve the following equation:

$$\frac{dT}{d\gamma} = 0 \quad (6.1)$$

As far as the MTPV is concerned, it is the locus of the points in which the maximum exploitation of the voltage is reached to have a certain value of torque. For the thesis, instead of looking for the MTPV, it is also possible to check the MPPV locus, namely, the *Maximum Power Per Volt*, expressed as:

$$\frac{dP}{dV} = 0 \quad (6.2)$$

The reason of doing it is related to the optimization process; anyway, the results will be equal, which means that both methods are valid.

It seems clear that in order to obtain both loci we need to solve a **maximum problem**. However, as already said, we need to do that respecting some constraints, imposed by the torque and speed requests. This is the reason why the **Lagrange multiplier** strategy has been adopted.

It consists in a method through which the maxima and the minima of a function that must respect equality constraints, can be found. To make everything clearer, we imagine to consider a bi-dimensional case and have a function $f(x, y)$, where x, y are the variables of interest and the equality constraint $g(x, y) = 0$. We suppose that both function f, g allow continuous partial derivative.

Necessary condition but not sufficient so that (x_0, y_0) is a relative extremal point for f respect to the constraint $g(x, y) = 0$ is that:

- $\nabla g(x_0, y_0) \neq 0$;
- after having define the *lagrangian function*:

$$L(x, y, \lambda) = f(x, y) - \lambda g(x, y) \quad (6.3)$$

it exists a real value λ_0 so that the gradient of L in (x_0, y_0, λ_0) is zero.

$$\nabla L(x_0, y_0, \lambda_0) = 0; \quad (6.4)$$

In other words, thanks to this method, it is possible to define an auxiliary function L and studying its maxima and minima, in order to find those of the function $f(x, y)$ respect to the constraint $g(x_0, y_0)$.

6.1.1 MTPA implementation

For the MTPA locus, we need to maximize the torque respect to the current. Its components have the following expressions:

$$i_d = I_m \cos\left(\frac{\pi}{2} + \gamma\right) \quad (6.5)$$

$$i_q = I_m \sin\left(\frac{\pi}{2} + \gamma\right) \quad (6.6)$$

The electromagnetic torque can be found as follow:

$$T_{emg} = \frac{3}{2}pp(\Phi_d i_q - \Phi_q i_d) \quad (6.7)$$

The function of whom we want to find the maximum is the following:

$$F_1 = \frac{T_{emg}}{I_m} = \frac{3}{2}pp(\Phi_d \sin\left(\frac{\pi}{2} + \gamma\right) - \Phi_q \cos\left(\frac{\pi}{2} + \gamma\right)) \quad (6.8)$$

For implementing the MTPA, the constraint of the torque must be considered: we want to obtain a value equal to the reference torque. The variable whom F_1 is depending on are the angle of the current vector γ and its amplitude I_m . So, applying the definition of the Lagrange multiplier:

$$L_{MTPA}(I_m, \gamma, \lambda) = F_1(I_m, \gamma) - \lambda(T_{emg}(I_m, \gamma) - T_{ref}) \quad (6.9)$$

In order to find the maxima points, we need the value of γ, I_m and of the auxiliary variable λ . Because it is not a close problem, the *Newton's method* has been employed.

Firstly we need to define the residual expression:

$$\begin{aligned} \frac{\partial L}{\partial \gamma} &= \frac{\partial F_1}{\partial \gamma} - \lambda \frac{\partial T_{emg}}{\partial \gamma} = R_1 \\ \frac{\partial L}{\partial \lambda} &= (T_{ref} - T_{emg}) = R_2 \\ \frac{\partial L}{\partial I_m} &= \frac{\partial F_1}{\partial I_m} - \lambda \frac{\partial T_{emg}}{\partial I_m} = R_3 \end{aligned} \quad (6.10)$$

According the Newton's method, the roots can be found as follow:

$$\begin{bmatrix} \gamma_{i+1} \\ \lambda_{i+1} \\ I_{mi+1} \end{bmatrix} = \begin{bmatrix} \gamma_i \\ \lambda_i \\ I_{mi} \end{bmatrix} + \begin{bmatrix} \Delta \gamma \\ \Delta \lambda \\ \Delta I_m \end{bmatrix} \quad (6.11)$$

As already said in the paragraph 5.2.3, the way to make the algorithm stop executing is either fixing the tolerance or set number of maximum iteration. In the first case, the error should be lower than the tolerance defined in this way:

$$ERR = \left\| \begin{bmatrix} R_1 \\ R_2 \\ R_3 \end{bmatrix} \right\| = \|RES\| \quad (6.12)$$

Finally, the Δx , where x stands for the variables of interest, can be found as follow:

$$\begin{bmatrix} \Delta\gamma \\ \Delta\lambda \\ \Delta I_m \end{bmatrix} = - \begin{bmatrix} \frac{\partial R_1}{\partial \gamma} & \frac{\partial R_1}{\partial \lambda} & \frac{\partial R_1}{\partial I_m} \\ \frac{\partial R_2}{\partial \gamma} & \frac{\partial R_2}{\partial \lambda} & \frac{\partial R_2}{\partial I_m} \\ \frac{\partial R_3}{\partial \gamma} & \frac{\partial R_3}{\partial \lambda} & \frac{\partial R_3}{\partial I_m} \end{bmatrix}^{-1} \begin{bmatrix} R_1 \\ R_2 \\ R_3 \end{bmatrix} \quad (6.13)$$

6.1.2 MPPV implementation

For the MPPV, the proceeding is basically the same. However, some differences occur: as already explained, the point in which the $\omega base$ is crossed, also corresponds to having reached the voltage limit imposed by the DC-bus, so by the battery. For the whole MPPV locus, the voltage will be equal to the maximum one. From the analytical point of view, it means adding an extra equality constraint to the Lagrangian multiplier method:

$$V = V_{lim} \quad (6.14)$$

where V_{lim} is the voltage limit, expressed as follow:

$$V_{lim} = \frac{V_{dc}}{\sqrt{3}} k_{safety} \quad (6.15)$$

V_{DC} is the voltage imposed by the DC-link of the vehicle and k_{safety} is a coefficient used to avoid to reach the real maximum value, in order not to create failures in the components.

Starting from the definition of the power:

$$P = \frac{3}{2} pp\Omega(\Phi_d i_q - \Phi_q i_d) \quad (6.16)$$

where Ω is the mechanical speed, expressed in $\frac{rad}{s}$.

Once defined it, it is possible to write the expression of the function of interest:

$$F_2 = \frac{P}{V} = \frac{\frac{3}{2} pp\Omega(\Phi_d I_m \sin(\frac{\pi}{2} + \gamma) - \Phi_q I_m \cos(\frac{\pi}{2} + \gamma))}{\sqrt{\omega^2(\Phi_d^2 + \Phi_q^2) + R_s^2(i_d^2 + i_q^2)}} \quad (6.17)$$

The proceeding is now identical to the previous one, with the addition of the new equality constraint and the new auxiliary variable λ_2 :

$$L_{MPPV}(I_m, \gamma, \lambda_1, \lambda_2) = F_2(I_m, \gamma) - \lambda_1(T_{emg}(I_m, \gamma) - T_{ref}) - \lambda_2(V(I_m, \gamma, \Omega) - V_{lim}) \quad (6.18)$$

The residuals present the following expression:

$$\begin{aligned} \frac{\partial L}{\partial \gamma} &= \frac{\partial F_2}{\partial \gamma} - \lambda_1 \frac{\partial T_{emg}}{\partial \gamma} - \lambda_2 \frac{\partial V}{\partial \gamma} = R_1 \\ \frac{\partial L}{\partial \lambda_1} &= (T_{ref} - T_{emg}) = R_2 \\ \frac{\partial L}{\partial \lambda_2} &= (V_{lim} - V) = R_3 \\ \frac{\partial L}{\partial I_m} &= \frac{\partial F_2}{\partial I_m} - \lambda_1 \frac{\partial T_{emg}}{\partial I_m} - \lambda_2 \frac{\partial V}{\partial I_m} = R_4 \end{aligned} \quad (6.19)$$

Finally, adopting the Newton's method, the increment at each iteration of the variables is:

$$\begin{bmatrix} \Delta \gamma \\ \Delta \lambda_1 \\ \Delta \lambda_2 \\ \Delta I_m \end{bmatrix} = - \begin{bmatrix} \frac{\partial R_1}{\partial \gamma} & \frac{\partial R_1}{\partial \lambda_1} & \frac{\partial R_1}{\partial \lambda_2} & \frac{\partial R_1}{\partial I_m} \\ \frac{\partial R_2}{\partial \gamma} & \frac{\partial R_2}{\partial \lambda_1} & \frac{\partial R_2}{\partial \lambda_2} & \frac{\partial R_2}{\partial I_m} \\ \frac{\partial R_3}{\partial \gamma} & \frac{\partial R_3}{\partial \lambda_1} & \frac{\partial R_3}{\partial \lambda_2} & \frac{\partial R_3}{\partial I_m} \\ \frac{\partial R_4}{\partial \gamma} & \frac{\partial R_4}{\partial \lambda_1} & \frac{\partial R_4}{\partial \lambda_2} & \frac{\partial R_4}{\partial I_m} \end{bmatrix}^{-1} \begin{bmatrix} R_1 \\ R_2 \\ R_3 \\ R_4 \end{bmatrix} \quad (6.20)$$

6.1.3 Flux maps interpolation

Once that the proceeding has been pointed out, the only thing that must be still found is an expression of both Φ_d and Φ_q that could be easy to derive respect to the variables of interest. The task can be completed looking at the flux maps, shown in paragraph 5.3. It is possible to **interpolate** them, in order to find the equations that will be applied in the solving of the Lagrangian multiplier method. The *curve fitting tool* of Matlab has been employed, obtaining the following expressions:

$$\Phi_d = P_{dopt1} + P_{dopt2} * i_d + P_{dopt3} * i_q + P_{dopt4} * i_d^2 + P_{dopt5} * i_d * i_q + P_{dopt6} * i_q^2 \quad (6.21)$$

$$\Phi_q = (P_{qopt1} i_d^2 + P_{qopt2} i_d + P_{qopt3}) (P_{qopt4} \tanh(P_{qopt5} * i_q) + P_{qopt6} * i_q) + P_{qopt7} \quad (6.22)$$

where the coefficient P_{opt} are depending on the flux maps considered. In fact, they can change from machine to machine and they end up to be the best coefficients in order to interpolate as faithful possible the flux maps of the motor.

6.1.4 Base and maximum speed calculation

Once obtained the expressions of the flux maps, the MTPA and MPPV loci can be found. As explained in paragraph 2.3.4, the former law is used in the *constant torque zone* and the latter one in the *constant power zone*. It follows that a fundamental parameter to be calculated is the **base speed** ω_b . The reason of its importance is that it helps us to understand where applying the MTPA law or MPPV law, being the switching point of the two loci.

It can be obtained from the voltage equations along the d and q axes, expressed in 2.21. It is known that in this point, the voltage reaches its limit; thus, imposing the voltage equal to it and considering the Φ_d and Φ_q from the MTPA law, the ω_{base} is obtained solving the following equation:

$$\omega^2(\Phi_{d_{MTPA}}^2 + \Phi_{q_{MTPA}}^2) + \omega(2R_s(\Phi_{d_{MTPA}}I_q - \Phi_{q_{MTPA}}I_d)) + R_s^2(i_d^2 + i_q^2) - V_{lim}^2 = 0 \quad (6.23)$$

It has to remember that is an electrical speed; in order to obtain a mechanical one, we need to divide for the number of pole pairs.

However, the ω_{base} will not be constant inside the T - ω characteristic. In fact, if we explore that area, leaving the same voltage limit, it would mean that there is more space of action to balance the effect of the back-EMF and the resistive drop, because the torque requested is lower than the maximum one and for that speed, the voltage has not reached the limit yet. So, in order to have a proper knowledge of the limit lines between the operative areas, this has been investigated through, calculating the value for all the torques, starting from the maximum one to zero.

On the other hand, another important limit that must be fixed is the ω_{max} , namely, the maximum speed achievable. To do that, we have done an approximation: in the MPPV zone, having a torque equal to zero means having reached the maximum speed. This statement is not completely true, especially looking at the figure 2.11, but it is a good approximation to fix the limit of the operative function. In addition, in the MPPV, we can imagine that the current is keeping itself constant and equal to the maximum value. Furthermore, the zero torque condition is translated in having Φ_q and I_q equal to zero. If the simplifying hypothesis is accepted, the maximum speed can be found as follow:

$$\omega_{max} = \sqrt{\frac{V_{lim}^2 - (R_s(-I_{max}))^2}{\Phi(-I_{max}, 0)^2}} \quad (6.24)$$

For the mechanical ω_{max} , it is still valid the same reasoning done for the base speed.

6.2 Optimization function

Once obtained the MTPA and MPPV loci and understood the the limits in which applying them, the last step is to find a proper function through which is possible to **optimize the motor**. In other words, we need to find the *objective function* of the optimization algorithm. Thinking about the application of the motor, the objective function chosen is the **power density**. It represents the amount of power it is possible to obtain per unit of volume:

$$P_{den} = \frac{P}{V} = \frac{P - P_{loss}}{V} = \frac{\eta P}{V} \quad (6.25)$$

where V is the volume of the machine and P_{loss} are the losses and η is the efficiency. As it can be noticed from the equation 6.25, the losses play a fundamental role in the whole optimization process. For the electrical machines we are talking about the:

- Iron losses;
- Copper losses.

The former has been already explained and present the expression 5.7, whereas the latter are due to the Joule effect, namely, to the stator resistance.

$$P_{cu} = 3R_s(i_d^2 + i_q^2) \quad (6.26)$$

They are not only fundamental to find the effective power transmitted, namely, the efficiency of the motor, but also because, thanks to them, it is possible to set the constraints needed too.

In fact, in order to avoid an unrealistic optimization, in which the volume becomes incredibly small without any limit, a **set of constraints** must be imposed. In the case of interest, the main constraint is about the maximum temperature inside the motor, strictly linked to the losses:

$$\Delta T = \frac{P_{iron} + P_{cu}}{h_{cv} S_{th}} \quad (6.27)$$

This limit is imposed to avoid to damage the materials inside the electrical machine: thinking about the permanent magnets, it is known they cannot overcome the Curie temperature so not to lose their magnetism.

In order to evaluate the efficiency of every possible candidate motor, we have calculated the losses, namely, the temperature reached, in **15 WLTP points** inside

the T - ω graph limit of interest. It means that the temperature is a function of the torque and speed requested in those points. Once, obtained the 15 different temperatures, the mean value of them is taken. Thus, the optimization problem has the following expression:

$$\begin{cases} Obj = \max\left(\frac{P - P_{loss}}{V}\right) \\ T(T_{WLTP}, \Omega_{WLTP}) < T_{MAX} \end{cases} \quad (6.28)$$

It has been built an appropriate Matlab script of the objective function to be maximized with the algorithm of interest. As input of the function, we have the parameters that concerns the materials and the quantities that has been considered fixed and not subjected to optimization; we have also the design parameters that are going to change during the optimization process, the maximum torque requested and the WLTP points needed to calculate the efficiency and, consequently, the objective function. As output we have the latter, the base speed line, the maximum speed and the temperature. As optimization algorithm, the *particle swarm optimization* has been employed.

6.2.1 Particle swarm optimization

It is a meta-heuristic method of optimization: with the term *heuristic* we refer to a tool that helps to discover something, whereas the term *meta* indicates an higher level of strategy that leads the research. These methods tend to replicate the natural phenomena of the nature. In the case of interest, the PSO reproduces the social behaviour and organized movement without collision, as in the birds flocks. In particular, it takes inspiration from the idea that all the members of a group can benefit of the discovery of one. In other words, looking at the birds behaviour, instead of looking for food without following any rule, all of them can share the information about their researches in order to drive all flock towards a certain direction. We can also imagine that the birds are helping us finding the best solution in an multi dimensional space. Naturally, being an heuristic method, it is not possible having proofs that we have found the global optimal solution; in any case, it has been tested that the PSO goes close to the real one. [63]

Going into the details, at the first step, a *poulation*, the swarm, has been defined. It is composed by candidate solutions called *particles*. During the exploration, the particles move in the space, following simple rules. As before explained, the particles are driven by their own best known position, but also by the best position of the swarm. In the case in which a new best position is discovered, it will guide the swarm movement. The proceeding is then repeated until the last iteration. It follows that, the higher is the number of iteration, the more there is the *probability* to find the optimal solution but not the *certainty* to have found it. Looking at

the updating of the solution, we can imagine to have a particle P , that occupies a position at the i_{th} iteration, denoted as $X^i(t)$ with the coordinates:

$$X^i(t) = (x^i(t), y^i(t)) \quad (6.29)$$

The speed of the particle is represented in the following way:

$$V^i(t) = (v_x^i(t), v_y^i(t)) \quad (6.30)$$

At every iteration, the particle position is updated as follow:

$$X^i(t+1) = X^i(t) + V^i(t+1) \quad (6.31)$$

Parallel to this, the particle speed is updated:

$$V^i(t+1) = wW^i(t) + c_1r_1(pbest^i - X^i(t)) + c_2r_2(gbest - X^i(t)) \quad (6.32)$$

where r_1 and r_2 represent numbers ranging from 0 to 1, w, c_1 and c_2 are parameters of the optimization algorithm. $pbest$ is the position of the best solution for the maximization problem and $gbest$ is the one explored by the rest of the swarm.

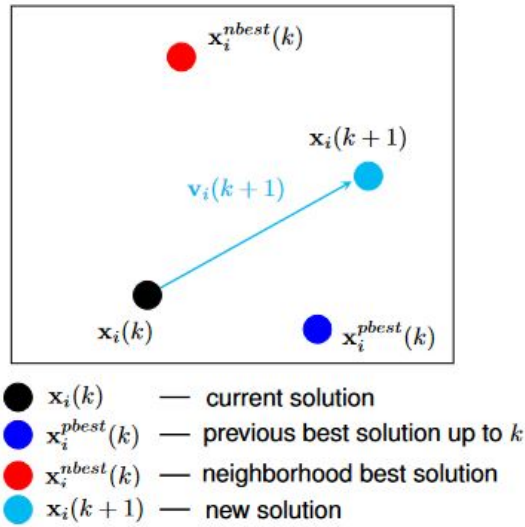


Figure 6.2: Updating solution process in PSO[64].

As far as the parameters are concerned, w is called *inertia weight constant*: it says how much the particle should preserve of its previous speed and direction. c_1 and c_2 are the *cognitive and social coefficients*: they determine how much to consider of the own particle search respect to that of the swarm. An interesting feature of this algorithm is that it can be parallelized due to the contemporary

research of the particles of the swarm.

In the case of our optimization problem, it maximizes the power density while maintaining the temperature below the limit. So the PSO, either minimize the distance to respect the constraints or maximize the power density when the temperature is below the limit. It finds the best particle at each iteration which first minimize the distance to respect to the constraint and then maximize the power density. It also follow the same principle to determine the best position reached by each particle along the iteration. Finally, the optimal result is obtained by selecting the best position among the historical best ones.

6.2.2 Optimization results

The algorithm needs a certain number of iterations to give satisfactory results: for this reason, it has been decided to set 150 iterations. In the case of interest, we have created a population of 32 identical machines.

The design parameters subjected to a possible change are the following:

Design parameters	Symbol	Unit of measurement
Yoke height	h_y	mm
Tooth height	h_t	mm
Bridge height	h_b	mm
Rotor active area height	H	mm
Magnets inclination	θ_{PM}	rad
Opening pitch	k_{pit}	
Barrier height	h_{barr}	mm
Magnet ratio	k_{PM}	
Number of turns per pole and phase	N_s	
Active length	L	mm

Table 6.1: Design parameters.

For some of them, the research area has been properly limited in order to avoid error in the proceeding and unrealistic geometries. All the others are considered fix and, consequently, they will not be affected by the optimization process.

The figure 6.4 shows the trend of research of the particle swarm optimization. As it can be possible to realize, despite the number of iteration had been fixed to 150, the algorithm have found what could be consider the maximum of the function in very few iterations.

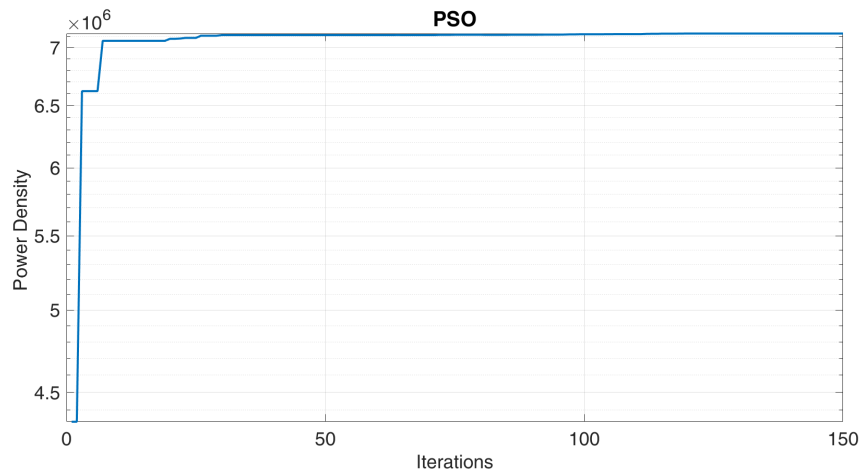


Figure 6.3: Iteration trend in the PSO.

In fact, after about 25 iterations, the improvements in the objective function are so small that cannot be anymore appreciated in the graph. It must be noted that in every iteration the **thermal constraints have been respected**, which means that the results are valid.

As already explained in the chapter 3, we have been looking for a machine capable of reaching an initial torque of **220 Nm** with a base speed of **2700 rpm** and a maximum speed of **10000 rpm**. In order to set the thermal constraint and evaluate the efficiency of the machine, the selected WLTP points are depicted in the following figure:

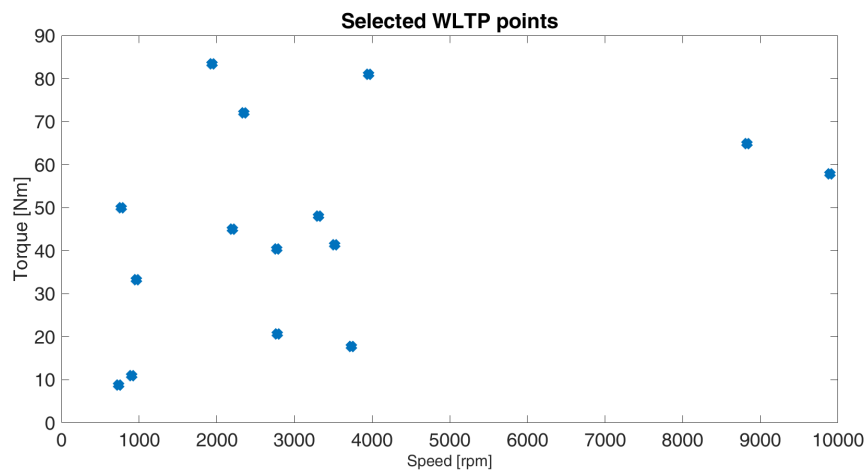


Figure 6.4: Selected WLTP points

	Symbol	Quantity	Unit of measurement
Main dimensions			
Poles	p	8	
Slots	Q_s	48	
Rotor outer radius	R_r	90.7	<i>mm</i>
Stator outer radius	R_s	137.1	<i>mm</i>
Stack length	L	50	<i>mm</i>
Air-gap	g	1.1	<i>mm</i>
Stator			
Teeth height	h_t	25	<i>mm</i>
Teeth width	w_t	4.8	<i>mm</i>
Slots width	w_s	7.2	<i>mm</i>
Yoke height	h_{ys}	20.3	<i>mm</i>
Number of turns per pole and phase	N_s	20	
Filling factor	k_{fill}	0.4	
Rotor			
Rotor shaft radius	r_o	52.5	<i>mm</i>
Bridges height	h_b	0.9	<i>mm</i>
Yoke height	h_{yr}	20.3	<i>mm</i>
Magnet inclination angle	θ_{PM}	0.532	<i>rad</i>
Pole pitch coefficient	k_{pit}	0.91	<i>p.u.</i>
Middle bridge coefficient	k_c	0.03	<i>p.u.</i>
Magnet height	h_{PM}	5.5	<i>mm</i>
Barriers distance coefficient	k_i	0.45	<i>p.u.</i>

Table 6.2: Dimensions of the motor.

As far as the materials are concerned, after initial tests in which the temperature was overcoming the maximum value permitted, it has been thought to increase the value of the convection coefficient from $25 \frac{W}{m^2K}$ to $150 \frac{W}{m^2K}$, typical of a water cooling. The other material parameters have not been changed and so the table 5.12 can be taken as reference.

The other values that must be listed are the DC-bus voltage and its safety coefficient and the losses parameters:

Looking at the electrical parameters obtained, we can observe this motor will have:

- $R_s = 0.0114\Omega$

	Symbol	Quantity	Unit of measurement
DC-bus voltage	V_{DC}	750	V
Hysteresis coefficient	k_{hys}	38	
Eddy currents coefficient	k_{edd}	3.87×10^7	
Additional coefficient	k_{add}	2.53	

Table 6.3: V_{DC} and losses coefficients .

- $I_{max} = 300A$
- $\eta = 96.2\%$

The reason of an high stator currents is hidden in the value of the stator resistance, which is small, because of N_s . In that sense, having a lower number of turns, implies having an higher current, in order to satisfy the torque request. Furthermore, it must be mentioned that, in the current calculation, we have considered only the convection coefficient, so it represents an esteem of the real I_{max} . The efficiency of the motor is in line with the value expected for this typology of motor. In addition, it represents the mean value of different WLTP points, spread inside the T - ω graph, which means that there will area in which the efficiency will be higher than it.

From the performance point of view, with this motor it is possible to obtain the torque requested. Furthermore, the value of the base and maximum speed are equal to:

- $\omega_{base} = 5500rpm$
- $\omega_{max} = 14000rpm$

They are slightly different from the reference wanted and they will lead to a CPSR equal to **2.54**. It means that the flux weakening area will not be as extended as wanted. This is due to the structure along the d -axis. On the one hand, having multiple barriers, have permitted to obtain high values of torque, due to the presence of PMs, but also because of the increased saliency of the whole structure. On the other hand, it will be more difficult to de-flux the machine, without reaching very high values of currents. In this sense, it can be considered as a finite drive. Once obtained the boundaries of the graph, to have an idea of the behaviour of the torque in the flux weakening area, they have been investigated two more points, in the MPPV zone. Once selected the torque wanted, the values of fluxes and current needed to calculate the related speed are found. Then, thanks to the curve fitting tool of Matlab, the final *torque – speed* graph is calculated.

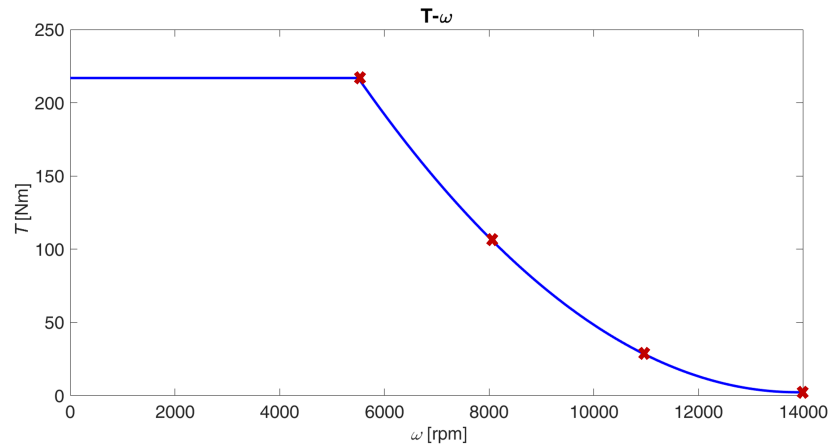


Figure 6.5: Torque-speed graph of the optimized motor.

The structure obtained from the optimization process has been shown in figure 6.12.

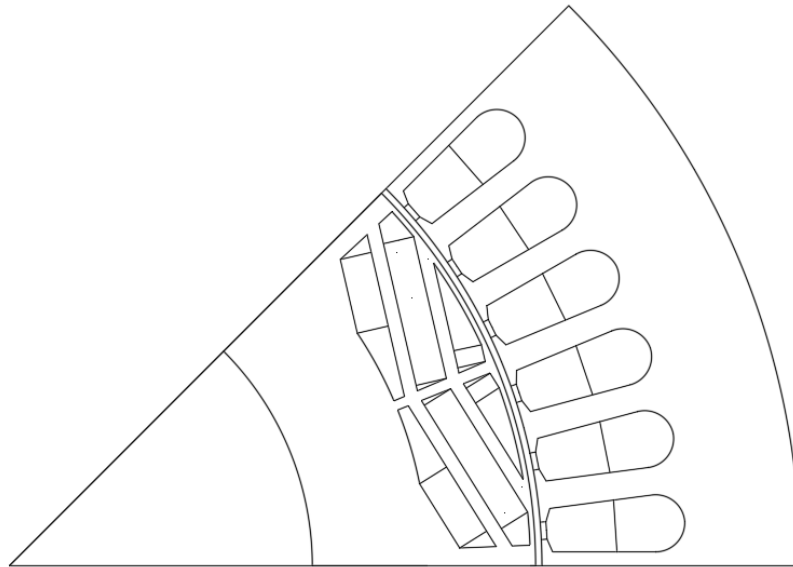


Figure 6.6: Optimized design of the motor.

After having shown the most important features of the motor, it is now possible to retrieve the flux maps and the torque one, from the reluctance network.

Flux and torque maps

Here, they are shown the flux maps along the d -axis and q -axis and the torque map:

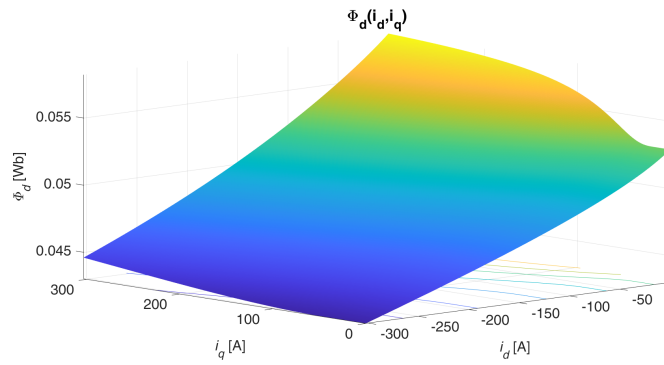


Figure 6.7: Φ_d flux map of the optimized motor.

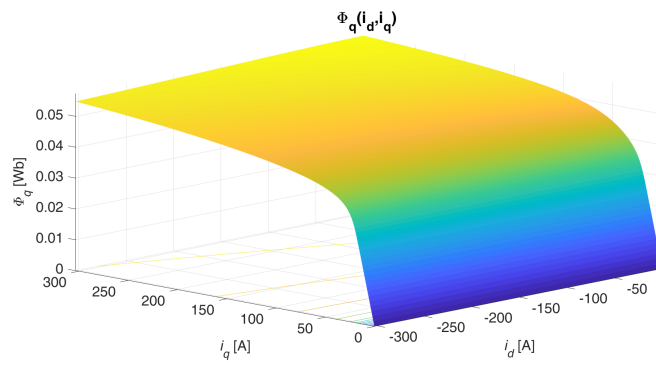


Figure 6.8: Φ_q flux map of the optimized motor.

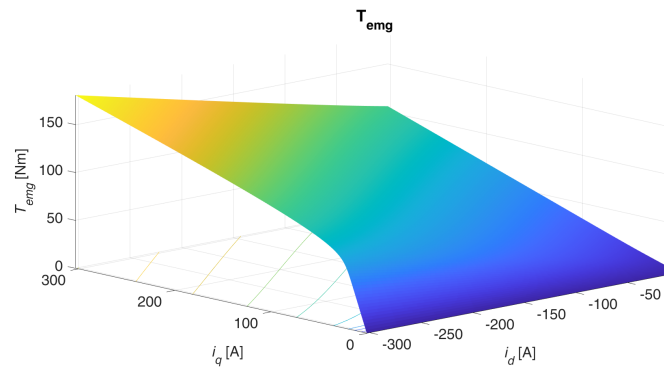


Figure 6.9: Torque map of the optimized motor.

As last task, the accuracy of the tool can be calculated again, making the comparison between the results of the reluctance network and the ones of finite elements software, for three different situations:

Test 1

For the first test, it has been chosen a current of amplitude $I_m = 54.8$ A and angle $\gamma = 34.6$. The torque calculated from the reluctance network is equal to **27 Nm**, whereas the one coming from FEMM 4.2 is **32.3 Nm**. It means that the error is equal to **19.63 %**.

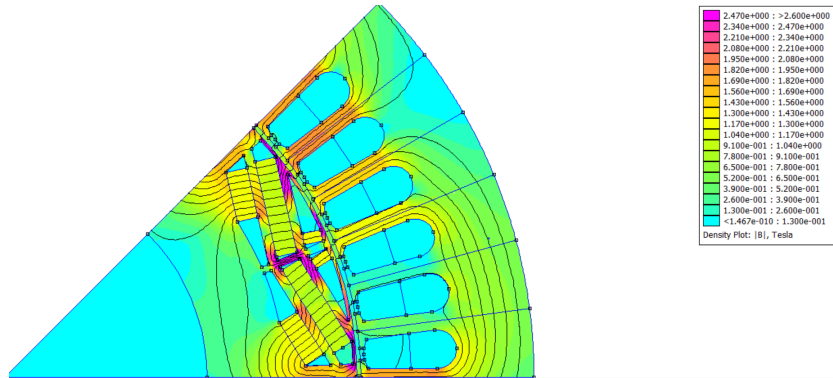


Figure 6.10: FEMM Flux map in *Test 1*.

Test 2

For the second test, it has been chosen a current of amplitude $I_m = 87$ A and angle $\gamma = 36$. The torque calculated from the reluctance network is equal to **44.9 Nm**, whereas the one coming from FEMM 4.2 is **54.8 Nm**. It means that the error is equal to **22.05 %**.

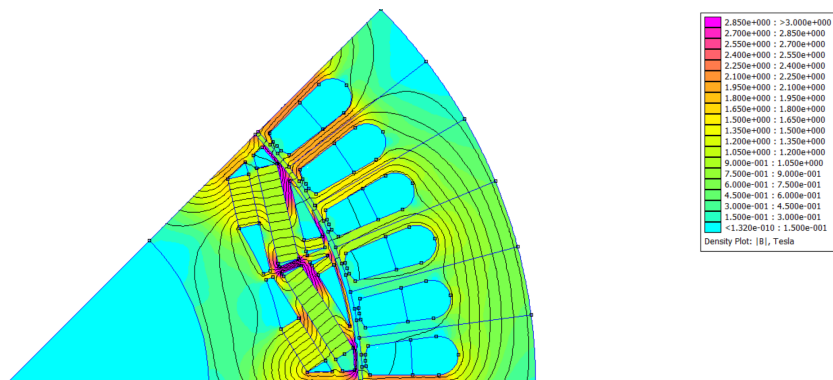


Figure 6.11: FEMM Flux map in *Test 2*.

Test 3

For the last test, it has been chosen a current of amplitude $I_m = 173$ A and angle $\gamma = 49$. The torque calculated from the reluctance network is equal to **88.6 Nm**, whereas the one coming from FEMM 4.2 is **110 Nm**. It means that the error is equal to **24.15 %**.

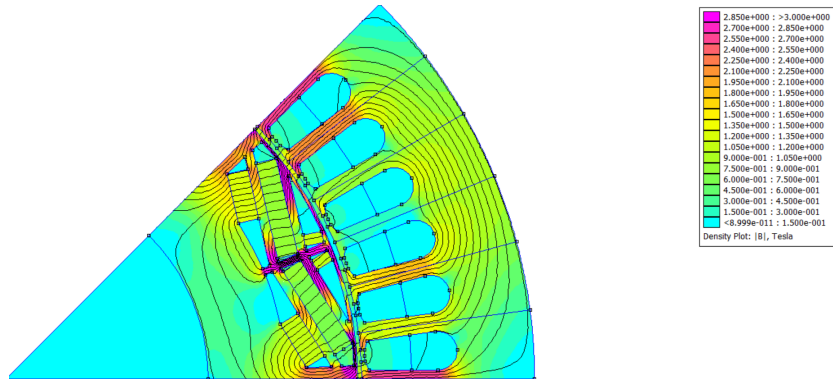


Figure 6.12: FEMM Flux map in *Test 3*.

As the previous results show, also in the case of the optimized motor, the accuracy of the whole reluctance network is stabilized under the **25%**.

Chapter 7

Conclusions

The goal the thesis has been to design and then optimize an interior permanent magnets motor that could be used for the traction of an electric vehicle. Nowadays, this typology is considered the most suitable for the application, thanks to the high torque and power density they can achieve, but also for the flux weakening capability they can guarantee. In addition, the saliency ratio different from zero allows to take advantage from the reluctance principle by granting an higher value of torque. In particular, according to the researches, the V-type shape seems to be the most promising, as it enhances the above mentioned features. In order to proceed with the design and the optimization path, it has been created a proper reluctance network of the machine, through which compute the electromagnetic torque in a fast way with a certain level of accuracy. The tool obtained has been validated with a finite elements software before proceeding with the control and optimization steps.

In the first part of the work, it has been investigated the features of the IPM motor for the EV application. An ideal $T-\omega$ graph reference has been found, setting an acceleration performance, taking inspiration from the already existing solutions in the market. In addition, the working points of the vehicle has been retrieved from the chosen driving cycle, the Worldwide harmonized Light vehicles Test Procedure.

Once obtained the reference, the structure of the motor has been described. In particular, as far as the rotor is concerned, it has been thought to realize a multi V-type geometry, composed by three barriers. To do that, it has been created a Matlab function through which it has been possible to calculate the main parameters of the rotor structure with a limited amount of inputs.

The design part has been carried out, adopting the reluctance network method. It has been built an equivalent magnetic circuit of the machine in order to represent

the magnetic flux behaviour and, from it, calculate the electromagnetic torque. It has been decided to create a circuit for each axis, in the d - q frame. In this way, the control of the motor would have become straightforward, giving the possibility to act directly on the components along these axes. Then, the two circuits have been coupled through the non linearity. Different tests have been carried out in order to validate the tool: it has been done making the comparison with the results coming from a finite elements software, FEMM 4.2.

The next step has concerned the control of the drive, following the MTPA and MPPV laws, according the speed requested. In order to implement them, the Lagrange multiplier method has been adopted. This is due to the fact that the research of the maximum was bound to respect torque constraint for the MTPA and an additional voltage one for the MPPV.

Once obtained the control laws, the last step was about the optimization of the motor. To do that, the particle swarm optimization algorithm has been adopted. The objective function to be maximized has been the power density of the motor. The process has been carried out respecting the thermal constraints. To verify them, the temperature, the efficiency and the objective function have been calculated in WLTP selected points inside the T - ω graph desired.

The reluctance network has proven to be a very quick method to monitor the magnetic flux, namely, the flux density in every part of the machine. The electromagnetic behaviour is well represented too: the torque has been easily and fastly calculated. On the other hand, the error on the torque is always present if compared to the finite elements method. To be more precise, it has been verified that it is not possible to obtain results with a percentage of error below the 10 % with the adopted circuits. In order to get more accurate results, it could be possible to add more reluctances: for instance, the space between the magnets barrier has not been modeled. Furthermore, the air barriers of the magnets do not find place in the adopted circuits. In a further improvements of the model they could be useful to trace better the flux path. In addition, some elements can be refined: for example, the magnets barriers can be modeled with more than one reluctance, all of them in parallel, according to the length of the barrier. The same reasoning can be made also for the stator. Looking at the circuits, it can be noticed that the air-gap has been modeled with just one radial reluctance. It could be possible to consider also the tangential ones, to get better results.

However, it must be noticed that an improvement of this kind will make the whole simulation slower, so a good trade off between the needs must be found.

In any case, the method is very effective from the control point of view, giving the possibility to act directly on the d and q components. This feature could gain

interest, especially thinking about the control algorithms usually implemented, like the Field oriented control and the direct flux vector control. Furthermore, in the d - q plane, all the quantities are considered continuous, because the frame is synchronous with the rotor.

Looking at the desired performance and optimized motor obtained, the results are almost in line. The motor is capable of giving the requested torque and the thermal constraint are respected in the selected WLTP points. It has been needed to increase the convection coefficient, passing through a water cooling. In reality, being only the convection considered, that value could be lowered. The efficiency in the selected WLTP working points is around the 96.2 %, a value that can be expected for a motor of this kind.

The base speed and the maximum speed are shifted more to right side of the graph and they are closer each other. It means that the constant power speed range is lower than expected. This is translated in a lower flux weakening capability. The reason of this is hidden in the particular rotor structure adopted. Placing more magnet barriers has increased the reluctance along the d -axis, meaning that the saliency of the machine would have been higher. It has led to have a bigger contribute from the reluctance principle as far as the torque production is concerned; on the other hand, having more permanent magnets has led not to explore the entire flux weakening area, because it is more difficult to act against the flux produced by them. The easiest solution could be to operate on the rotor structure, going back to a single barrier. In this case, more current would be needed to have the same torque, but the performance would benefit from the change. The reluctance network adopted, could give more accurate results, passing trough an easier geometry. As always, a good trade off must be found.

Bibliography

- [1] Virta. *The global electric vehicle market overview in 2022: statistics forecasts*. 2021. URL: <https://www.virta.global/global-electric-vehicle-market/> (cit. on p. 1).
- [2] Emmanuel Agamloh, Annette von Jouanne, and Alexandre Yokochi. «An Overview of Electric Machine Trends in Modern Electric Vehicles». In: *Machines* 8.2 (2020). ISSN: 2075-1702. DOI: 10.3390/machines8020020. URL: <https://www.mdpi.com/2075-1702/8/2/20> (cit. on pp. 2, 6, 7, 9, 11).
- [3] Gianmario Pellegrino, Alfredo Vagati, Paolo Guglielmi, and Barbara Boazzo. «Performance Comparison Between Surface-Mounted and Interior PM Motor Drives for Electric Vehicle Application». In: *IEEE Transactions on Industrial Electronics* 59.2 (2012), pp. 803–811. DOI: 10.1109/TIE.2011.2151825 (cit. on pp. 2, 9).
- [4] Vijay Prabakaran. «Future of Battery Technologies». In: (Jan. 2021) (cit. on p. 4).
- [5] Christine Gable and Scott Gable. *Inverters and Converters in Hybrids and EV (Electric Vehicles)*. 2021. URL: <https://www.treehugger.com/how-inverters-and-converters-work-85612> (cit. on p. 5).
- [6] Ion Boldea, Lucian N. Tutelea, Leila Parsa, and David Dorrell. «Automotive Electric Propulsion Systems With Reduced or No Permanent Magnets: An Overview». In: *IEEE Transactions on Industrial Electronics* 61.10 (2014), pp. 5696–5711. DOI: 10.1109/TIE.2014.2301754 (cit. on p. 6).
- [7] Pichit Lumyong and Piampoom Sarikprueck. «A Study on Induction Motor Efficiency Improvement for Implementing in Electric Vehicle». In: *2018 21st International Conference on Electrical Machines and Systems (ICEMS)*. 2018, pp. 616–619. DOI: 10.23919/ICEMS.2018.8549478 (cit. on p. 7).
- [8] J.G. Cowie and D.T. Brender. «Die-cast copper rotors for improved motor performance». In: *Conference Record of the 2003 Annual Pulp and Paper Industry Technical Conference, 2003*. 2003, pp. 42–49. DOI: 10.1109/PAPCON.2003.1216898 (cit. on p. 7).

- [9] Paolo Guglielmi. *Electric Machines for traction*. University lecture. 2021 (cit. on pp. 7, 8).
- [10] Wikimedia Commons. *File:Tesla Model S motor cutout.jpg — Wikimedia Commons, the free media repository*. [Online]. 2020. URL: https://commons.wikimedia.org/w/index.php?title=File:Tesla_Model_S_motor_cutout.jpg&oldid=508107177 (cit. on p. 8).
- [11] A. M. Omekanda. «Switched reluctance machines for EV and HEV propulsion: State-of-the-art». In: *2013 IEEE Workshop on Electrical Machines Design, Control and Diagnosis (WEMDCD)*. 2013, pp. 70–74. DOI: 10.1109/WEMDCD.2013.6525166 (cit. on p. 8).
- [12] Md Ashfanor Kabir. «High Performance Reluctance Motor Drives with Three-phase Standard Inverter». Doctor of Philosophy. North Carolina State University, 2017 (cit. on p. 9).
- [13] Yawei Wang, N. Bianchi, Silverio Bolognani, and Luigi Alberti. «Synchronous motors for traction applications». In: June 2017, pp. 1–8. DOI: 10.23919/EETA.2017.7993210 (cit. on pp. 10, 11).
- [14] Bogdan Varaticeanu, Paul Minciunescu, and Daniel Fodorean. «Mechanical design and analysis of a permanent magnet rotors used in high-speed synchronous motor». In: *EEA - Electrotehnica, Electronica, Automatica* 62 (Jan. 2014), pp. 9–17 (cit. on p. 10).
- [15] Emanuele Fornasiero, Luigi Alberti, N. Bianchi, and Silverio Bolognani. «Considerations on Selecting Fractional-Slot Nonoverlapped Coil Windings». In: *Industry Applications, IEEE Transactions on* 49 (May 2013), pp. 1316–1324. DOI: 10.1109/TIA.2013.2251853 (cit. on p. 11).
- [16] Michele Angelo Pastorelli. *Electrical drives*. University lecture. 2021 (cit. on p. 11).
- [17] Iqbal Husain et al. «Electric Drive Technology Trends, Challenges, and Opportunities for Future Electric Vehicles». In: *Proceedings of the IEEE* 109.6 (2021), pp. 1039–1059. DOI: 10.1109/JPROC.2020.3046112 (cit. on p. 12).
- [18] Myeong-Hwan Hwang, Jong-ho Han, Dong-Hyun Kim, and Hyun-Rok Cha. «Design and Analysis of Rotor Shapes for IPM Motors in EV Power Traction Platforms». In: *Energies* 11 (Sept. 2018), p. 2601. DOI: 10.3390/en11102601 (cit. on pp. 12, 14).
- [19] Hanwoong Ahn, Hyunjong Park, Changhyun Kim, and Hyung Woo Lee. «A Review of State-of-the-art Techniques for PMSM Parameter Identification». In: *Journal of Electrical Engineering & Technology* 15 (2020), pp. 1177–1187 (cit. on p. 12).

- [20] Pei Yulong, Shi Yanwen, Yanjun Yu, Chai Feng, and Liu Yue. «Increasing the saliency ratio of fractional slot concentrated winding interior permanent magnet synchronous motors». In: *IET Electric Power Applications* 9 (July 2015). DOI: 10.1049/iet-epa.2014.0336 (cit. on p. 13).
- [21] Peng Zhang, Dan M. Ionel, and Nabeel A. O. Demerdash. «Saliency ratio and power factor of IPM motors optimally designed for high efficiency and low cost objectives». In: *2014 IEEE Energy Conversion Congress and Exposition (ECCE)*. 2014, pp. 3541–3547. DOI: 10.1109/ECCE.2014.6953882 (cit. on p. 13).
- [22] Andreas Krings and Christian Monissen. «Review and Trends in Electric Traction Motors for Battery Electric and Hybrid Vehicles». In: *2020 International Conference on Electrical Machines (ICEM)*. Vol. 1. 2020, pp. 1807–1813. DOI: 10.1109/ICEM49940.2020.9270946 (cit. on pp. 14, 33).
- [23] Sung-Jin Kim, Sang-Yong Jung, and Yong-Jae Kim. «Air-Barrier Width Prediction of Interior Permanent Magnet Motor for Electric Vehicle Considering Fatigue Failure by Centrifugal Force». In: *Journal of Electrical Engineering and Technology* 10 (May 2015), pp. 952–957. DOI: 10.5370/JEET.2015.10.3.952 (cit. on p. 14).
- [24] P. Guglielmi, M. Pastorelli, A. Carrer, A. Beato, D. D’Antonio, and L. Fagnano. «An IPM-PMASR motor for home appliance washing machines». In: *IECON 2013 - 39th Annual Conference of the IEEE Industrial Electronics Society*. 2013, pp. 2608–2613. DOI: 10.1109/IECON.2013.6699542 (cit. on p. 15).
- [25] Alfredo Vagati, Paolo Guglielmi, Gianmario Pellegrino, and Eric Armando. «Optimal design of IPM-PMASR motors for wide constant power speed range applications». In: 2007 (cit. on p. 15).
- [26] B. A. Welchko, T.M. Jahns, W.L. Soong, and J.M. Nagashima. «IPM synchronous machine drive response to symmetrical and asymmetrical short circuit faults». In: *Energy Conversion, IEEE Transactions on* 18 (July 2003), pp. 291–298. DOI: 10.1109/TEC.2003.811746 (cit. on p. 19).
- [27] J. Shen, Dan Shi, Canfei Wang, Peng Li, Kang Wang, and Mengjia Jin. «Torque ripple analysis for IPM AC motors». In: *COMPEL: Int J for Computation and Maths. in Electrical and Electronic Eng.* 33 (Aug. 2014). DOI: 10.1108/COMPEL-09-2013-0294 (cit. on p. 22).
- [28] Seunghyeon Cho, Dong-Chan Lee, Jongyoung Kang Hwang, Kilju Kim, Gyeong Uk Jang, Daesung Bae, Hyung Soo Mok, and Chang-Wan Kim. «Optimal design to reduce torque ripple of IPM motor with radial based function meta-model considering design sensitivity analysis». In: *Journal of Mechanical Science and Technology* 33 (Aug. 2019). DOI: 10.1007/s12206-019-0740-0 (cit. on p. 22).

- [29] T Sumeet Singh and Amit Kumar Jain. «Improved Direct Torque Controlled IPM Synchronous Motor using variable band 12 sector control in two level inverter». In: *2016 IEEE 6th International Conference on Power Systems (ICPS)*. 2016, pp. 1–6. DOI: 10.1109/ICPES.2016.7584064 (cit. on p. 22).
- [30] Z.Q. Zhu and D. Howe. «Analytical prediction of the cogging torque in radial-field permanent magnet brushless motors». In: *IEEE Transactions on Magnetics* 28.2 (1992), pp. 1371–1374. DOI: 10.1109/20.123947 (cit. on p. 23).
- [31] Jae Seok Choi, Kazuhiro Izui, Shinji Nishiwaki, Atsushi Kawamoto, and Tsuyoshi Nomura. «Topology Optimization of the Stator for Minimizing Cogging Torque of IPM Motors». In: *IEEE Transactions on Magnetics* 47.10 (2011), pp. 3024–3027. DOI: 10.1109/TMAG.2011.2158572 (cit. on p. 23).
- [32] Wu Ren, Qiang Xu, Qiong Li, and Libing Zhou. «Reduction of Cogging Torque and Torque Ripple in Interior PM Machines With Asymmetrical V-Type Rotor Design». In: *IEEE Transactions on Magnetics* 52.7 (2016), pp. 1–5. DOI: 10.1109/TMAG.2016.2530840 (cit. on p. 23).
- [33] Gian Mario Pellegrino. *Laboratory of power converters and electrical drives*. University lecture. 2021 (cit. on p. 24).
- [34] Ming-Shyan Wang, Min-Fu Hsieh, and Hsin-Yu Lin. «Operational Improvement of Interior Permanent Magnet Synchronous Motor Using Fuzzy Field-Weakening Control». In: *Electronics* 7.12 (2018). ISSN: 2079-9292. DOI: 10.3390/electronics7120452. URL: <https://www.mdpi.com/2079-9292/7/12/452> (cit. on p. 25).
- [35] Jianxia Sun, Cheng Lin, Jilei Xing, and Xiongwei Jiang. «Online MTPA Trajectory Tracking of IPMSM Based on a Novel Torque Control Strategy». In: *Energies* 12.17 (2019). ISSN: 1996-1073. DOI: 10.3390/en12173261. URL: <https://www.mdpi.com/1996-1073/12/17/3261> (cit. on p. 26).
- [36] Gianmario Pellegrino, Eric Armando, and Paolo Guglielmi. «Direct-Flux Vector Control of IPM Motor Drives in the Maximum Torque Per Voltage Speed Range». In: *IEEE Transactions on Industrial Electronics* 59.10 (2012), pp. 3780–3788. DOI: 10.1109/TIE.2011.2178212 (cit. on p. 28).
- [37] Ansys blog. *Designing an E-Machine: An Electromagnetic Problem?* Jan. 2021 (cit. on p. 30).
- [38] Adem Dalcali. «OPTIMAL DESIGN OF HIGH PERFORMANCE INTERIOR PM MOTOR FOR ELECTRIC VEHICLE». In: *The International Journal of Energy and Engineering Sciences* 3 (2019), pp. 46–54. ISSN: 2602-294X (cit. on p. 31).

- [39] Emma Arfa Grunditz and Torbjörn Thiringer. «Performance Analysis of Current BEVs Based on a Comprehensive Review of Specifications». In: *IEEE Transactions on Transportation Electrification* 2 (2016), pp. 270–289 (cit. on p. 33).
- [40] Wikipedia contributors. *Driving cycle* — *Wikipedia, The Free Encyclopedia*. [Online; accessed 7-February-2022]. 2021. URL: https://en.wikipedia.org/w/index.php?title=Driving_cycle&oldid=1047777220 (cit. on p. 33).
- [41] WLTP FACTS.EU. *what is wltp and how does it work?* 2020 (cit. on p. 34).
- [42] Wikipedia contributors. *Worldwide Harmonised Light Vehicles Test Procedure* — *Wikipedia, The Free Encyclopedia*. [Online; accessed 7-February-2022]. 2022. URL: https://en.wikipedia.org/w/index.php?title=Worldwide_Harmonised_Light_Vehicles_Test_Procedure&oldid=1064472753 (cit. on p. 34).
- [43] Wikipedia contributors. *Vehicle dynamics* — *Wikipedia, The Free Encyclopedia*. [Online; accessed 8-February-2022]. 2021. URL: https://en.wikipedia.org/w/index.php?title=Vehicle_dynamics&oldid=1056854191 (cit. on p. 35).
- [44] S.M. Rakibul Hassan, Toukir Islam, Mohammad Ali, and Md. Quamrul Islam. «Numerical Study on Aerodynamic Drag Reduction of Racing Cars». In: *Procedia Engineering* 90 (2014). 10th International Conference on Mechanical Engineering, ICME 2013, pp. 308–313. ISSN: 1877-7058. DOI: <https://doi.org/10.1016/j.proeng.2014.11.854>. URL: <https://www.sciencedirect.com/science/article/pii/S1877705814029919> (cit. on p. 37).
- [45] Heinz Heisler. «14 - Vehicle body aerodynamics». In: *Advanced Vehicle Technology (Second Edition)*. Ed. by Heinz Heisler. Second Edition. Oxford: Butterworth-Heinemann, 2002, pp. 584–634. ISBN: 978-0-7506-5131-8. DOI: <https://doi.org/10.1016/B978-075065131-8/50015-4>. URL: <https://www.sciencedirect.com/science/article/pii/B9780750651318500154> (cit. on p. 38).
- [46] Wolf-Heinrich Hucho. «Chapter 1 - Introduction to automobile aerodynamics». In: *Aerodynamics of Road Vehicles*. Ed. by Wolf-Heinrich Hucho. Butterworth-Heinemann, 1987, pp. 1–46. ISBN: 978-0-7506-1267-8. DOI: <https://doi.org/10.1016/B978-0-7506-1267-8.50005-1>. URL: <https://www.sciencedirect.com/science/article/pii/B9780750612678500051> (cit. on p. 38).

- [47] Heinz Heisler. «1 - Vehicle Structure». In: *Advanced Vehicle Technology (Second Edition)*. Ed. by Heinz Heisler. Second Edition. Oxford: Butterworth-Heinemann, 2002, pp. 1–36. ISBN: 978-0-7506-5131-8. DOI: <https://doi.org/10.1016/B978-075065131-8/50002-6>. URL: <https://www.sciencedirect.com/science/article/pii/B9780750651318500026> (cit. on p. 38).
- [48] Chaoying Xia, Zhiming DU, and Cong Zhang. «A Single-Degree-of-Freedom Energy Optimization Strategy for Power-Split Hybrid Electric Vehicles». In: *Energies* 10 (July 2017), p. 896. DOI: 10.3390/en10070896 (cit. on p. 39).
- [49] Javad Soleimani and Abolfazl Vahedi. «IPM Synchronous Motor for Traction Applications: Performance Analysis Considering Airgap Variation». In: *Przegląd Elektrotechniczny* 12 (Dec. 2012), pp. 200–205 (cit. on p. 45).
- [50] Chao-hui Zhao, Haihong Qin, and Yang-guang Yan. «Analysis of the Pole Numbers on Flux and Power Density of IPM Synchronous Machine». In: *2005 International Conference on Power Electronics and Drives Systems*. Vol. 2. 2005, pp. 1402–1407. DOI: 10.1109/PEDS.2005.1619908 (cit. on p. 46).
- [51] F. Cupertino, G. Pellegrino, and et al. *SyR-e: Synchronous Reluctance (machines) - evolution*. [Online]. 2022. URL: <https://sourceforge.net/projects/syr-e/> (cit. on p. 49).
- [52] Hayder Y. Ahmad and David Bonnieman. «Fundamental Recommendations for the Design Configuration of Rotor Shafts for Use in Electric Motors and Generators». In: *Procedia Engineering* 160 (2016). XVIII International Colloquium on Mechanical Fatigue of Metals (ICMFM XVIII), Gijón (Spain), September 5-7, 2016, pp. 37–44. ISSN: 1877-7058. DOI: <https://doi.org/10.1016/j.proeng.2016.08.860>. URL: <https://www.sciencedirect.com/science/article/pii/S1877705816330958> (cit. on p. 51).
- [53] Vishal Jagota, Amanpreet Sethi, and Dr-Khushmeet Kumar. «Finite Element Method: An Overview». In: *Walailak Journal of Science Technology* 10 (Jan. 2013), pp. 1–8. DOI: 10.2004/wjst.v10i1.499 (cit. on p. 61).
- [54] Ki-Chan Kim, Ju Lee, Hee Jun Kim, and Dae-Hyun Koo. «Multiobjective Optimal Design for Interior Permanent Magnet Synchronous Motor». In: *IEEE Transactions on Magnetics* 45.3 (2009), pp. 1780–1783. DOI: 10.1109/TMAG.2009.2012820 (cit. on p. 64).
- [55] A. Soualmi, F. Zidat, Gh. Bara, and P. Lombard. «Estimation of losses in the stator and rotor of interior permanent magnets synchronous (IPMs) machines using reluctance network Reluctance». In: *2016 XXII International Conference on Electrical Machines (ICEM)*. 2016, pp. 1673–1679. DOI: 10.1109/ICELMACH.2016.7732749 (cit. on pp. 64, 65).

- [56] Fabio Tinazzi and Mauro Zigliotto. «Torque Estimation in High-Efficiency IPM Synchronous Motor Drives». In: *IEEE Transactions on Energy Conversion* 30 (Sept. 2015), pp. 1–8. DOI: 10.1109/TEC.2015.2408214 (cit. on p. 66).
- [57] A. Di Gerlando, G. M. Foglia, and R. Perini. «Procedure to Define an Accurate Model for Saturation and Cross-Coupling in Interior Permanent Magnet Machines». In: *2020 International Conference on Electrical Machines (ICEM)*. Vol. 1. 2020, pp. 291–297. DOI: 10.1109/ICEM49940.2020.9270752 (cit. on p. 67).
- [58] Ox Science. *Magnetic hysteresis loop for ferromagnetic materials*. 2020. URL: <https://oxscience.com/hysteresis-loop/> (cit. on p. 67).
- [59] Floran Martin, Anouar Belahcen, and Mohammed El Hadi Zaïm. «Effect of magnet materials on optimal design of a high speed PMSM». In: *2015 18th International Conference on Electrical Machines and Systems (ICEMS)*. 2015, pp. 661–667. DOI: 10.1109/ICEMS.2015.7385117 (cit. on pp. 69, 82).
- [60] A. E. Fitzgerald and Charles. Kingsley. *Electric machinery /*. 6th ed. Includes index. New Delhi : McGraw-Hill, c2014. (Cit. on p. 70).
- [61] Mitch Olszewski Oak Ridge National Laboratory. «Evaluation of the 2007 Toyota Camry hybrid synergy drive system». In: (2007) (cit. on p. 80).
- [62] ISOVAC. *isovac high-perm 330-50 A*. [Online]. 2018. URL: <https://www.voestalpine.com> (cit. on p. 83).
- [63] Adrian Tam. *A Gentle Introduction to Particle Swarm Optimization*. [Online]. 2021. URL: <https://machinelearningmastery.com/a-gentle-introduction-to-particle-swarm-optimization/> (cit. on p. 99).
- [64] Jerome E. Onwunalu. *Optimization of field development using particle swarm optimization and new well pattern descriptions*. 2010 (cit. on p. 100).